3-23-2018

Design and Testing of an Additively Manufactured CubeSat Structural Bus

Karson A. Roberts

DESIGN AND TESTING OF AN ADDITIVELY MANUFACTURED CUBESAT STRUCTURAL BUS

THESIS

Karson A. Roberts, Second Lieutenant, USAF

AFIT-ENY-MS-18-M-289

DEPARTMENT OF THE AIR FORCE
AIR UNIVERSITY

AIR FORCE INSTITUTE OF TECHNOLOGY

Wright-Patterson Air Force Base, Ohio

AFIT-ENY-MS-18-M-289

DESIGN AND TESTING OF AN ADDITIVELY MANUFACTURED CUBESAT STRUCTURAL BUS

THESIS

Presented to the Faculty

Department of Astronautical Engineering

Graduate School of Engineering and Management

Air Force Institute of Technology

Air University

Air Education and Training Command

in Partial Fulfillment of the Requirements for the

Degree of Master of Science in Astronautical Engineering

Karson A. Roberts, BSME

Second Lieutenant, USAF

March 22, 2018

AFIT-ENY-MS-18-M-289

DESIGN AND TESTING OF AN ADDITIVELY MANUFACTURED CUBESAT STRUCTURAL BUS

Karson A. Roberts, BSME
Second Lieutenant, USAF

Committee Membership:

Major Ryan O'Hara, PhD
Chair

Dr. Richard Cobb
Member

Dr. Carl Hartsfield
Member

Dr. Anthony Palazotto
Member

Abstract

Recent innovations in additive manufacturing and design capabilities have opened the door for more opportunities to integrate multiple functions into a structural design. Specifically, 3D printing through advanced laser powder bed fusion of metal powder allows for the development and integration of advanced structures that were previously unachievable. The demonstration of these techniques on a small satellite results in a structural bus consisting of various external and internal features, increasing its functionality and capabilities beyond simply providing structural support. 3D printing a multi-functional CubeSat bus with these integrated features such as internal lattices and wiring tabs demonstrates a new way of thinking going forward: modularizing the structural design and incorporating various capabilities that can meet a unique or generic satellite mission. This research addresses the design and testing of an additively manufactured CubeSat structural bus. 3D printing capabilities were harnessed to incorporate lattices into the walls of the structure, increasing its natural frequency and decreasing mass. The 3D printed unloaded CubeSat structure was vibration tested to NASA GEVS qualification levels, and showed no damage and proved survivability under these loading conditions.

Acknowledgments

There are many people I would like to thank who have been instrumental in this research. To my family and friends for being encouraging and supportive through the hard work that was required for this research. My research advisor Major Ryan O'Hara, who pushed me to think outside the box and come up with unique design ideas. Dr. Hartsfield, who took time to provide guidance and ideas throughout this research even though he wasn't my advisor. Phillip Smith, who encouraged and guided me through the intricacies of CAD software while teaching me many life lessons along the way. Randall Sharp, for sharing some of his expertise with fastener types and functions. The in-house technical experts with hands on satellite experience, Chris Sheffield, Sean Miller, Chris Lommano, and Jorge Urena, who provided insight into the practicality of various designs and aided with testing. Travis Shelton and Ben Doane, who provided additional insight into design ideas and provided guidance on the slicing programs and lattice generation software. Josh DeWitt, who aided with print parameters to use and ensuring the proof of concept designs printed smoothly. Brian Crabtree and Chris Harkless, who worked extremely hard in the post-processing of the final design and turned it around extremely quickly. Last but not least, Greg Cobb, who helped with the laser vibrometer testing and setup.

Karson A. Roberts

Table of Contents

Page

List of Figures

List of Tables

List of Acronyms

1U 10 cm x 10 cm x 10 cm CubeSat unit volume size

ABS Acrylonitrile Butadiene Sytrene

ADCS Attitude Determination and Control System

AFIT Air Force Institute of Technology

AM Additive Manufacturing

ASD Acceleration Spectral Density

BCC Body-Centered Cubic

CAD Computer Aided Design

CDH Command and Data Handling

COTS Commercial Off-The-Shelf

CSD Canistered Satellite Dispenser

EMC Electromagnetic Compatibility

EMI Electromagnetic Interference

GEVS Generic Environmental Verification Specification

NASA National Aeronautics and Space Administration

NRCSD NanoRacks CubeSat Deployer

PLA Polylactic Acid

PPOD Poly Picosatellite Orbital Deployer

TVAC Thermal Vacuum

DESIGN AND TESTING OF AN ADDITIVELY MANUFACTURED CUBESAT STRUCTURAL BUS

I. Introduction

1.1 Background

In a environment that strives for new cutting edge technologies and innovations, satellite programs around the world are faced with great expectations. These programs experience a constant pressure to produce high performing satellites with maximum capabilities, all while attempting to meet a budget. Additive Manufacturing (AM) is a growing technology with aerospace applications that can help achieve this objective. Also known as 3D printing, this production method builds parts by adding successive layers of materials, as opposed to the traditional subtractive manufacturing method that removes material. This layer-wise fabrication approach allows for the creation of complex geometries while reducing material, cutting cost, and reducing weight [9]. AM allows for digital modularity and parametric designs that conventional machining methods can't accomplish. It can print plastics, metals, composites, and a variety of other materials that are commonly used in the aerospace industry.

3D printing has applications in a variety of fields, including a growing interest from satellite programs. Many space programs are looking towards CubeSats to carry out their mission. CubeSats are cheap small satellites originally intended for educational use that have shown expanding capabilities since their inception. The original design was developed by California Polytechnic State University (Cal Poly) at San Luis Obispo and Stanford University in 1999 [14]. It is intended to fit into a

CubeSat dispenser, with the 10 cm x 10 cm x 10 cm CubeSat unit volume size (1U) configuration not exceeding 1.33 kg in mass [2]. A 2U configuration is the joining of two 1U CubeSats, and so on. Developers have also created larger sizes such as the 3U, 6U, 12U, and 27U to increase overall CubeSat capabilities and performance. Figure 1.1 shows several different sizes of CubeSats that are commonly used.

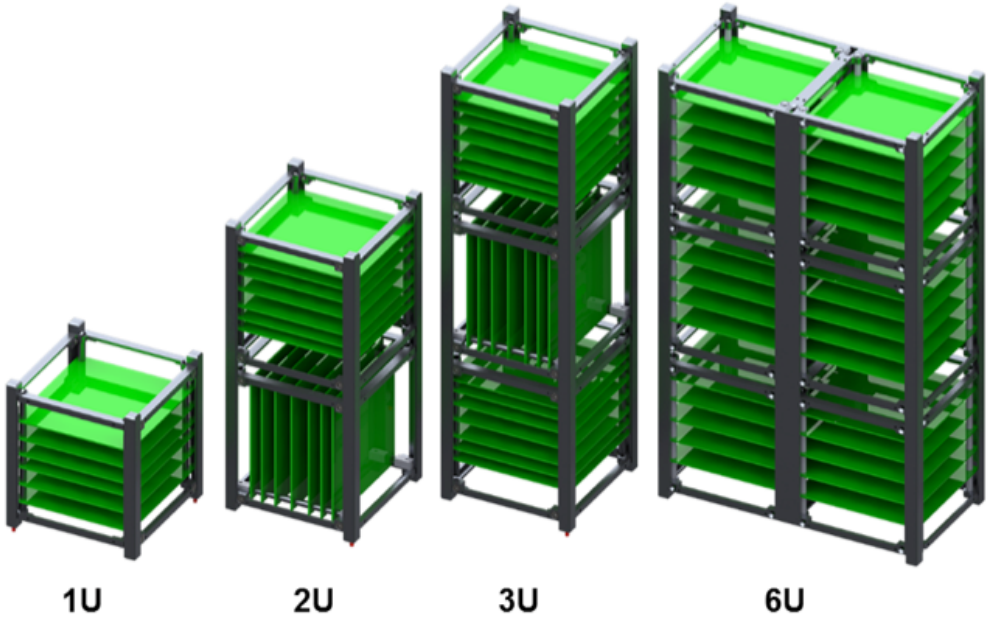

Figure 1.1: Typical CubeSat Form Factors [1]

The CubeSat structural bus hosts and supports the payload, electronics, batteries, and other essential components required for a successful mission. The CubeSat bus can be purchased as a Commercial Off-The-Shelf (COTS) component, making it readily available and applicable to a variety of missions. COTS equipment is cost effective and has become widely used in aerospace applications. The standard layout allocates a particular space inside the bus structure to a specific satellite component. The CubeSat structure must undergo and pass a variety of tests in order to be qualified for flight. One of these is vibration testing, which certifies the bus meets the structural

and loading requirements necessary to survive the launch environment. The advent of AM allows for research into an innovative design that better utilizes the structural bus. The performance of the bus structure is enhanced through lowering mass, reducing cost, and reducing part and fastener count.

1.2 Motivation

The CubeSat structural bus is often an overlooked area of research; it is the infrastructure of the satellite that supports the equipment necessary for an operational mission. Applying AM techniques to CubeSat bus designs and production promise to lower costs and increased functionality of future space systems. It is a Department of Defense initiative since it enhances the capabilities of the warfighter and drives new technological advancement in design methods [15]. Additionally, 3D printing of the bus will reduce the number of screws and fasteners in the structure, which is a common component that fails during structural testing [16]. In addition, integrating complex structures such as lattices into the CubeSat bus can reduce mass, making more mass available for other components such as electronics or the payload.

1.3 Problem Statement

As satellites become smaller and their functional requirements continue to increase, a need exists to improve the structural bus of a CubeSat to allow for more flexibility and enhanced payload capabilities to meet mission requirements.

1.4 Research Objectives

The problem statement results in three main objectives for this research:

1. Design a 3D printed 3U CubeSat structural bus.

2. Incorporate unique features in the bus structure that take advantage of 3D printing capabilities.

3. Test and verify that this bus meets the structural and loading requirements for launch applications.

1.5 Assumptions and Limitations

The scope of this research is limited to designing a structural bus of a 3U form factor. The bus designs are intended to print on Air Force Institute of Technology (AFIT) 3D printers, so designs are constrained to these printer capabilities. Initial designs are printed in plastic to demonstrate proof of concept and feasibility, while the final design is printed in metal.

This research is not limited to a specific experiment, satellite mission, or launch vehicle. The focus during this research is on the structural performance of the bus designs, and is validated through vibration testing. The CubeSat bus mass and physical size is designed to be compatible with the Poly Picosatellite Orbital Deployer (PPOD), a Cal Poly created common interface between the launch vehicle and the CubeSat. The specifics on the PPOD and other deployers will be discussed in more detail in Chapter II.

1.6 Methodology

Three main tasks are conducted throughout this thesis:

1. Identify unique 3D printed features that can be implemented into a 3U CubeSat bus that improve its performance.

2. Design a structural bus that incorporates these unique 3D printed features.

3. Demonstrate overall structural performance of the 3D printed 3U CubeSat. Experimentally test and evaluate these performance criteria in a relevant laboratory environment, through a combination of static and dynamic testing in AFITs experimental test facilities.

The first task of this research is accomplished through a review of the literature to identify the requirements of bus structures, and identifying areas of improvement. After this is completed, knowledge from the literature is applied to multiple iterations of bus designs using Computer Aided Design (CAD) software, keeping in mind AM requirements. A design is then selected from a combination of various performance criteria. The design will incorporate unique 3D printed features, which have been selected through both the literature review and experimental testing. Once these components are integrated, the third task of the research is accomplished through validating that the structure meets the necessary loading and functional requirements. CubeSat design specification documents are used to verify the structure meets all functional requirements. An industry standard that is used to ensure the CubeSat will survive the structural loads imparted during launch is the National Aeronautics and Space Administration (NASA) Generic Environmental Verification Specification (GEVS) loading profile [17]. Since a launch provider was not defined in this research, this profile will be the basis for evaluating structural integrity, with analysis conducted on the experimental data that is gathered. The vibration table at AFIT is used to carry out this testing.

1.7 Expected Contributions

This research presents an AM CubeSat bus design, and analyzes its practicality. This structure will display the benefits of reduction in cost, mass, and complexity for future satellites and pave the way forward on a different way to approach struc-

tural bus designs. It will demonstrate a bus that exhibits capabilities beyond merely providing support for the satellite components. This proof of concept and design methodology could be applied to future designs on real satellite missions.

1.8 Overview

The literature review in Chapter II presents an overview on CubeSats, AM, and 3D printing design considerations. Chapter III explains the methodology for the design and testing carried out in this thesis. The analysis and results of the designs and tests are discussed in Chapter IV. Chapter V summarizes the results, draws conclusions, and discusses recommendations for future work.

II. Literature Review

2.1 Chapter Overview

The intention of this chapter is to provide the reader with the background information required to understand the investigation of an additively manufactured CubeSat structural bus. To first understand the problem, one must know the purpose of the CubeSat bus, as well as its design requirements. Next, required space-qualifying tests as well as common failure mechanisms in CubeSats are covered. Lastly, the basics of Additive Manufacturing (AM) such as the different categories, design considerations and requirements, advantages/disadvantages, and aerospace applications are discussed.

2.2 CubeSat Overview

This section provides an overview of CubeSats and its relevance to the aerospace community. A brief history of CubeSat missions is discussed, as well as design requirements, common bus components, and different launch vehicle interfaces. The understanding of how CubeSats operate and function, their technological progression since inception, and the current state of the art is important to understand in order to develop new and innovative designs.

2.2.1 CubeSat History/Functionality

The CubeSat program started as a collaborative effort between departments at Cal Poly and Stanford, with an objective to cut satellite development costs, assure access to space for small payloads, and create frequent launch opportunities for picosatellites [2]. Table 2.1 outlines the satellite classification system used in this research, where CubeSats typically range from picosatellites to microsatellites.

Table 2.1: Satellite Classifications [7]

Satellite Name	**Mass (kg)**
Large	> 1000
Medium	500 to 1000
Mini	100 to 500
Micro	10 to 100
Nano	1 to 10
Pico	0.1 to 1
Fenito	< 0.1

The small 1U CubeSat has a maximum mass of 1.33 kg, and falls in the nanosatellite category [2]. The 3U CubeSat is essentially three 1U CubeSats put together, and is considered a nanosatellite due to its mass of 4 kg. 6U up to 27U CubeSat form factors are microsatellites (masses range from 12.0 kg to 54.0 kg) [18]. The CubeSat program developed standard sizes and requirements for CubeSats beyond just picosatellites, which was its original objective. As a result of this standardization, a baseline was created for industry leaders, government entities, and universities across the world to follow in their CubeSat designs. The dimensional requirements and engineering drawings of a 3U CubeSat as established by Cal Poly can be seen in Figure 2.1. Cal Poly has similar specification documents for the other CubeSat form factors. The drawings shows specific requirements for outer dimensions of the CubeSat, as well as railing requirements, access port locations once integrated into the dispenser, and locations of the deployment switches and separation springs. The purpose of the railings, separation springs, and deployment switches are discussed further in Section 2.2.2.

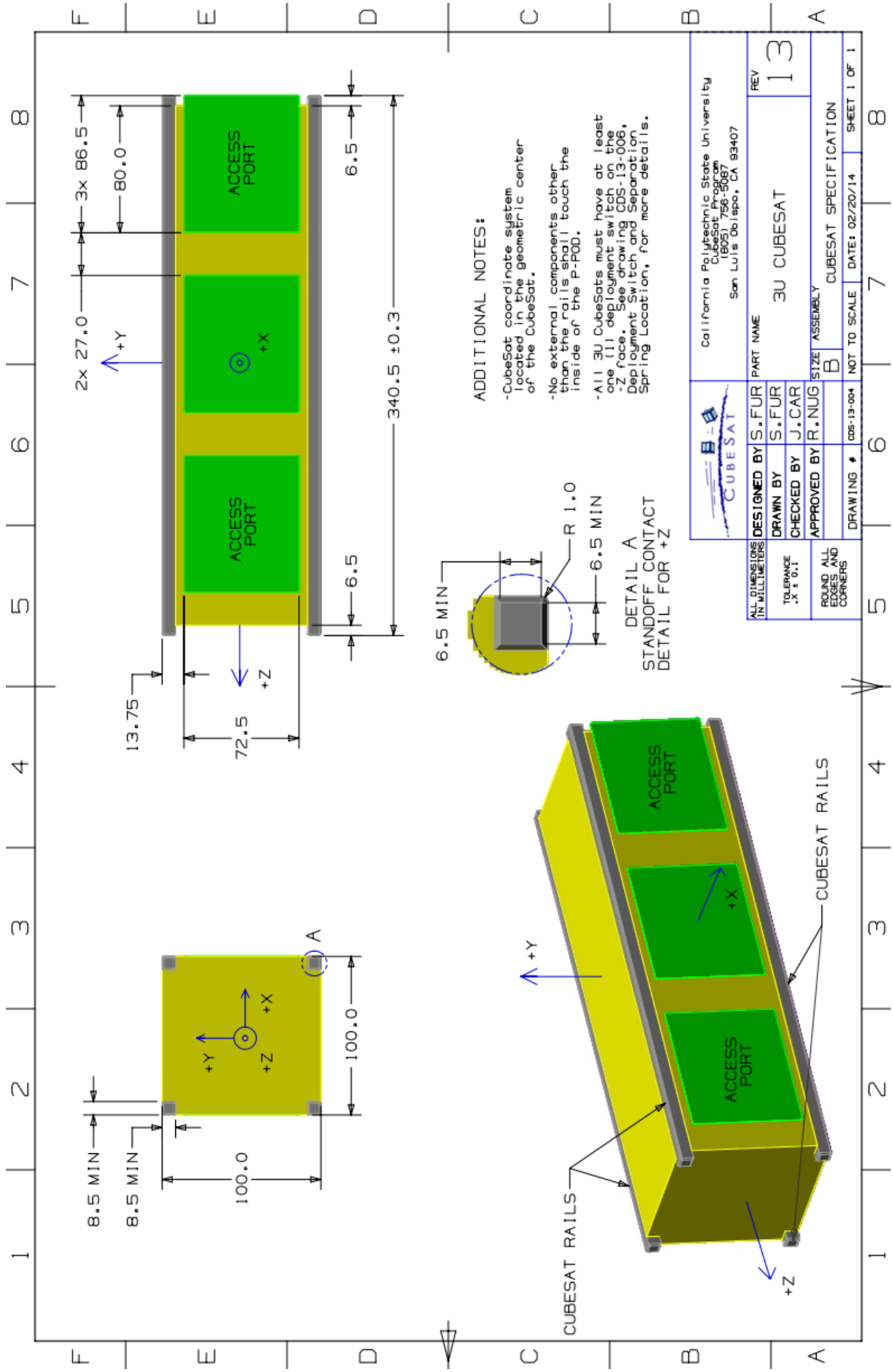

Figure 2.1: 3U CubeSat Specification [2]

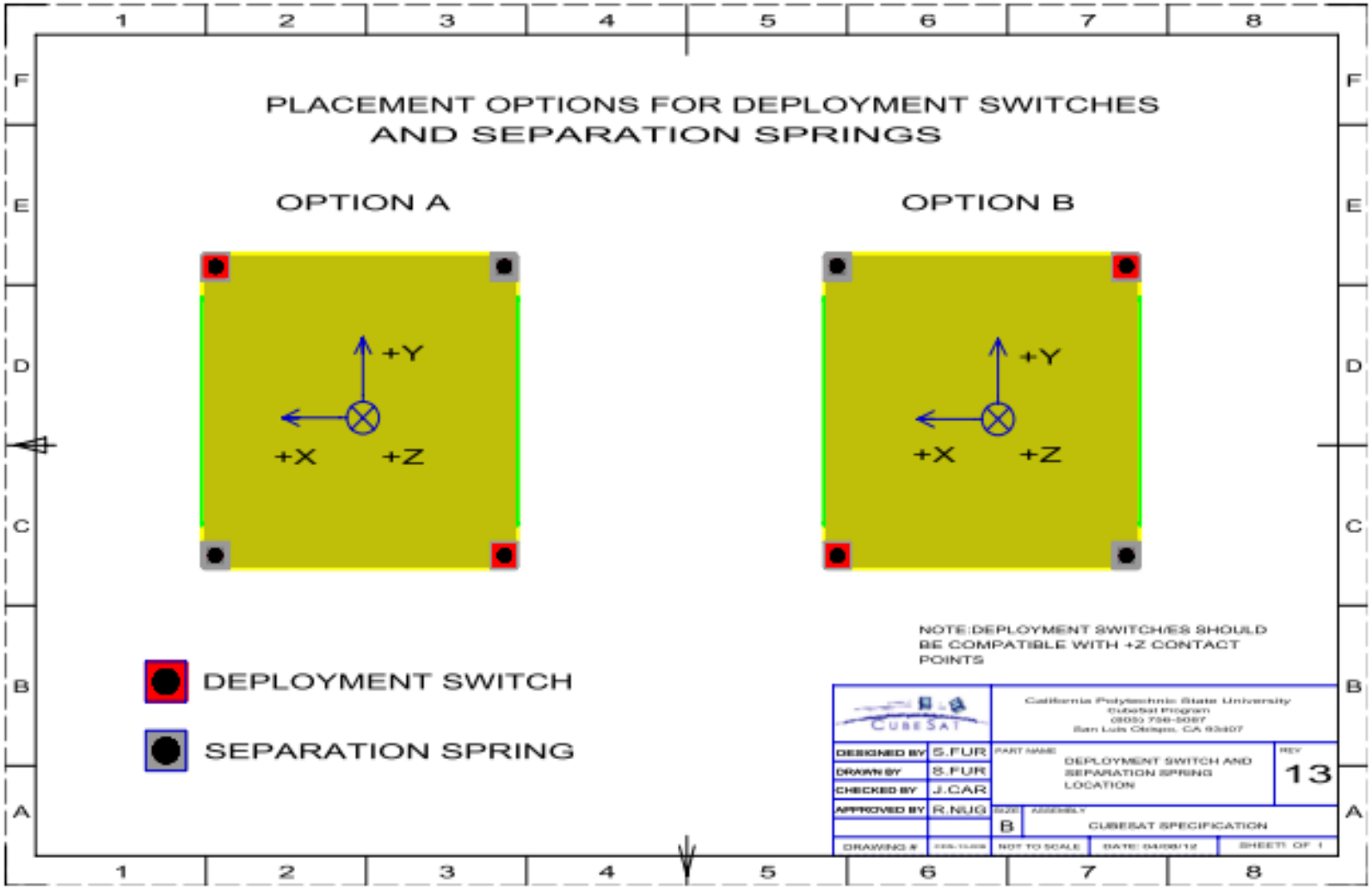

Figure 2.2: CubeSat Deployment Switch and Separation Spring Locations [2]

The space domain is continuing to become more and more hostile, making it imperative for the U.S. to keep its technological and innovative edge globally. Although the U.S. is currently the front runner in CubeSat programs, other nations are becoming more involved. 46% of the CubeSats launched from 2000-2012 are from the U.S., while Russia and India account for 27% and 11%, respectively [19].

CubeSats were originally intended for educational purposes, in order to get students familiar with satellite programs and program management techniques [20]. They are relatively low cost, for universities can design, build, and test CubeSats for around $200,000 [20]. CubeSats can be broken up into 4 classes: E-class, C-class, S-class, and T-class [21]. E-class satellites are educational satellites to train students, C-class satellites provide communication services, S-class satellites are science satellites that collect data, and T-class satellites test new industry technologies [19]. Since the early 2000s, there has been a clear shift in CubeSat applications from educational uses to technology demonstrations [19]. Some previous CubeSat missions of relevance include: QuakeSat-1, the first Earth observation CubeSat launched in 2003 that provided earthquake detection data[20], MEPSI, a military 2U experimental CubeSat launched in 2002 [19], among many others. Scientists are discovering that while relevant data can be acquired from CubeSats, launching a constellation of more than one CubeSat has the potential for enhanced mission capabilities. For example, Planet Lab Inc.'s Dove constellation consists of over 100 Earth-imaging CubeSats that allows for a wider scope of coverage that a single satellite couldn't achieve on its own [22]. Also, the QB50 Project uses a network of CubeSats to collect in-situ data of the thermosphere, and this data arguably couldn't be collected without the use of CubeSats [23].

All satellites, including CubeSats, consist of some basic subsystems that are essential to survivability and mission success. Some of these components are custom

designed and built, while others can be bought as COTS parts. These include the Attitude Determination and Control System (ADCS), propulsion, power, Command and Data Handling (CDH), communications, thermal control, structure, and payload [8]. ADCS determines the attitude and orientation of the satellite, and can also alter it if needed through active means [24]. Propulsion is used to launch the satellite into space, but can also be used on board the satellite for orbital maneuvers and attitude corrections [8]. Power is often acquired from solar panels or batteries while on orbit, and is necessary to turn on and run all of the satellite components. Solar panels can be body mounted or in a deployable configuration to achieve this objective. Body mounted solar panels are fixed to the bus structure itself, while deployable solar panels have hinges that can rotate the panels outward and orient them towards the sun. The command and data handling subsystem is the "brains" of the CubeSat, and consists of the electronics and codes necessary to run specific commands while on orbit. This subsystem is often integrated as a stack of electronics, and typically follows a PC/104 hole layout. An example stack of electronics at AFIT can be seen in Figure 2.3, following by specifications for the PC/104 layout in Figure 2.4.

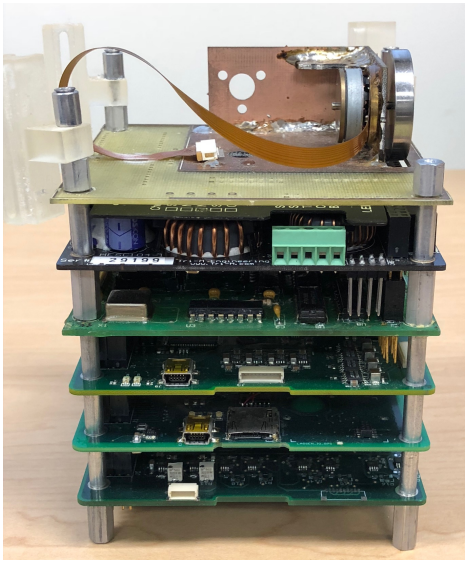

Figure 2.3: Sample Stack of Electronics

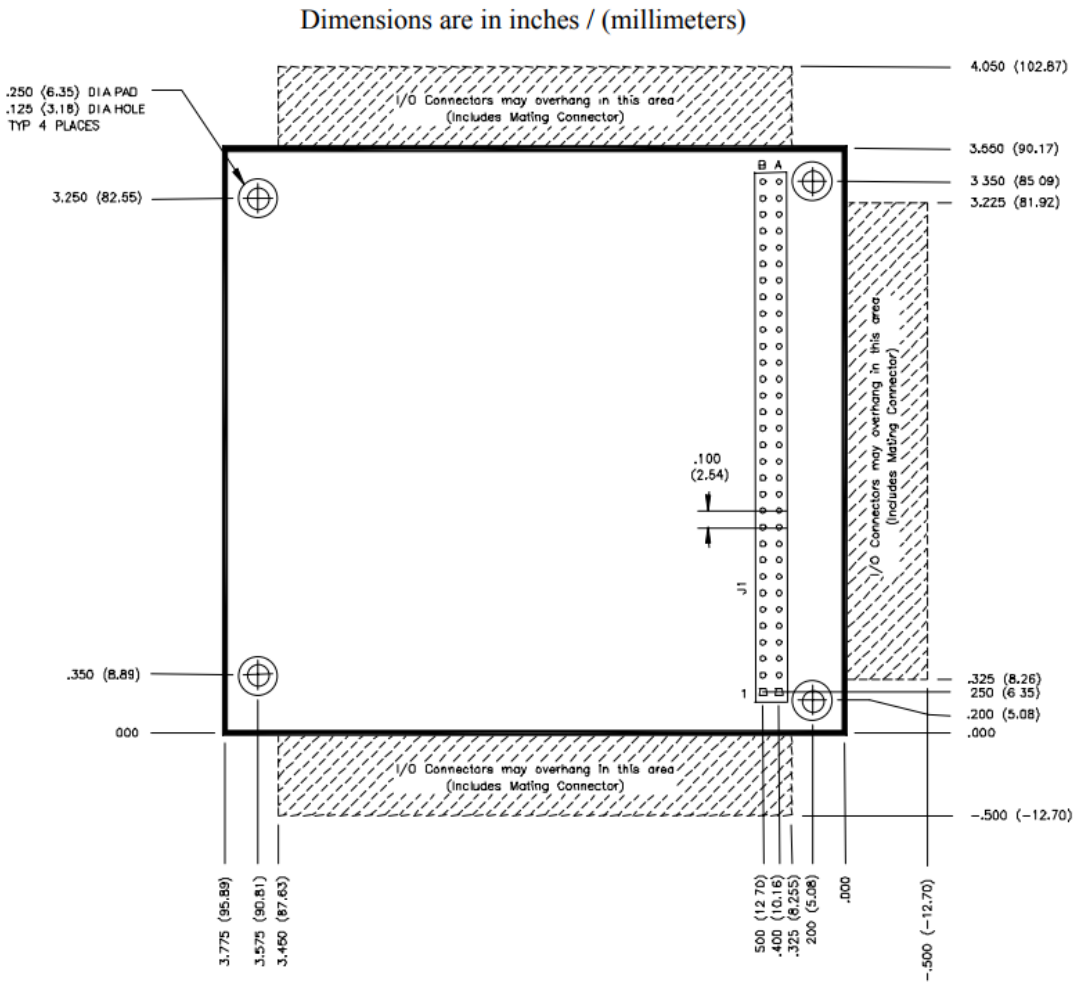

Figure 2.4: PC/104 Layout for 8 bit board [3]

The communications subsystem consists of the antennas and radios needed for the satellite to communicate with the ground station or other satellites. Thermal control is necessary to avoid overheating or freezing of components due to the extreme temperatures in space, ensuring proper functionality and mission success [8]. The payload is the component that carries out the overall mission objective, such as an optic for Earth imaging applications. Lastly, one of the most commonly overlooked subsystems is the bus structure. This is the mechanical subsystem that holds all of the components in place upon launch and provides structural support. It can be

custom designed or bought as a COTS product from companies such as Pumpkin or Clyde Space. The bus structure is commonly designed to be compatible with stacks of electronics that have a PC/104 hole layout. These stacks of electronics can be dropped down into the bus from the top or slid in from side, depending on the design of the bus structure. Sharp corners are avoided when possible, and fillets are implemented into the structural design to reduce stress concentrations [8]. It is important to note that all of these subsystems discussed need to be accounted for to in the AM bus design process to ensure the satellite functions properly.

2.2.2 CubeSat Launch Vehicle Interfaces

The purpose of the CubeSat launch vehicle interface is to protect and house the satellite during launch, as well as effectively deploy the satellite into its desired orbit once in space. It also acts as a safeguard to the rest of the launch vehicle, to protect other satellites or the rocket from getting damaged in the event of a satellite malfunction. CubeSats commonly get to space through a rideshare, where they are not the primary payload and are included on the launch as a "passenger", space permitting. A rideshare requires at least two spacecraft on the launch vehicle: the heaviest is called the prime, and the others are considered rideshares or tertiary payloads [25]. To be approved to launch, the CubeSat must be compatible with the interface/deployer it will use, meeting all of their specific requirements. A variety of CubeSat interfaces/deployers are commonly used, including the Poly Picosatellite Orbital Deployer (PPOD), Canistered Satellite Dispenser (CSD), NanoRacks CubeSat Deployer (NRCSD), among others. The CubeSat standard by Stanford and Cal Poly led to the development of the PPOD, designed to create a standard launch vehicle interface that safely groups multiple CubeSats for launch while not harming the primary payload or launch vehicle [26]. It is made of Al 7075 T-73 with Teflon-impregnated hard

anodized coating, and designed to hold up to 34 cm x 10 cm x 10 cm in hardware [5] [27]. CubeSats are required to be made from Aluminum 7075, 6061, 5005, and/or 5052 in order to be compatible with this deployer [2]. Typical PPOD configurations include three 1U CubeSats, one 3U CubeSat, or one 1U and one 2U CubeSat [5]. Figure 2.5 shows the PPOD in its stowed and deployed state.

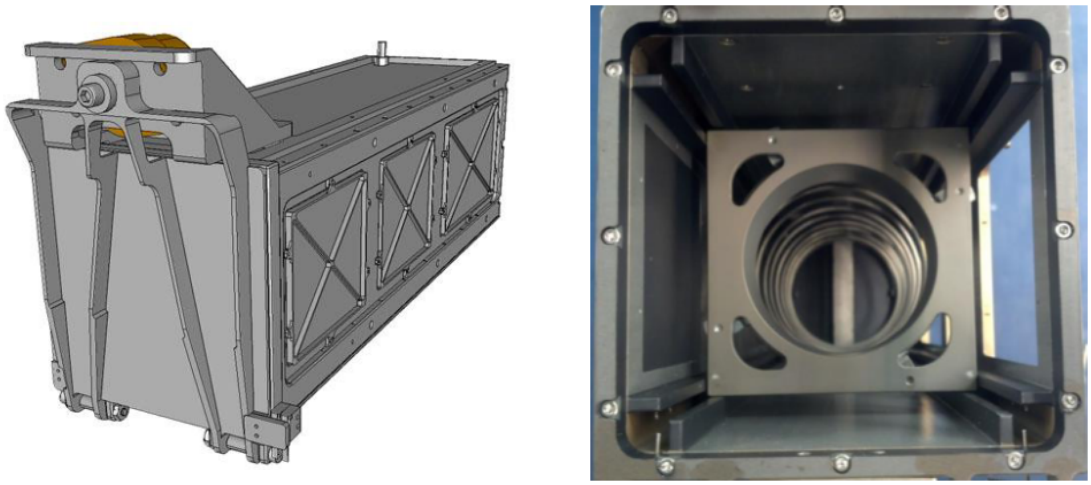

(a) Stowed State

(b) Deployed State

Figure 2.5: PPOD in Stowed and Deployed Configuration [2]

The railings described in Figure 2.1 provide the interface between the CubeSat and the PPOD, and are inserted into the deployer as shown in the cross section portion of Figure 2.5. At least 75% of the rails must contact the PPOD at all times, and they must have a surface roughness of less than 1.6 µm [2]. The CubeSats are deployed from the PPOD through a non-explosive spring release mechanism that minimizes shock to the other satellites and the launch vehicle [26]. The deployment switches and separation springs are important CubeSat components shown in Figure 2.2 that need to be accounted for in the structural design of the CubeSat. The deployment switches rest against the lid of the PPOD and keeps the satellite's electronics powered off during launch. Once the CubeSat is ejected from the PPOD, the switches are released and electronics powered on. The separation springs attached from the outside

of the PPOD and push against an interior plate. This plate, pushed by the springs, contacts the legs (bottom portion of the railings) of the CubeSat bus, ensuring a secure fit and successful deployment from the PPOD. For the purposes of this thesis, the bus is designed to be compatible with the PPOD. It has a robust design, significant flight heritage, and is the deployer of choice for several U.S. launch service providers for 1U-3U CubeSats [8]. The CSD and the NRCSD are covered briefly to provide background and context into a couple of the other common CubeSat dispensers available.

The CSD is also a proven dispenser with flight heritage that encompasses larger CubeSat sizes of 3U-27U. The CSD grips the bottom tabs running the length of both sides of the CubeSat, providing a preloaded junction that is secure during launch [18]. This plays a crucial role in being able to accurately model and predict loads that the critical components of the CubeSat will experience [18]. This tabbed integration design is the main difference from the PPOD, which uses a rail based system. Figure 2.6 shows a 6U CubeSat with tabs on the bottom, after ejection from the CSD.

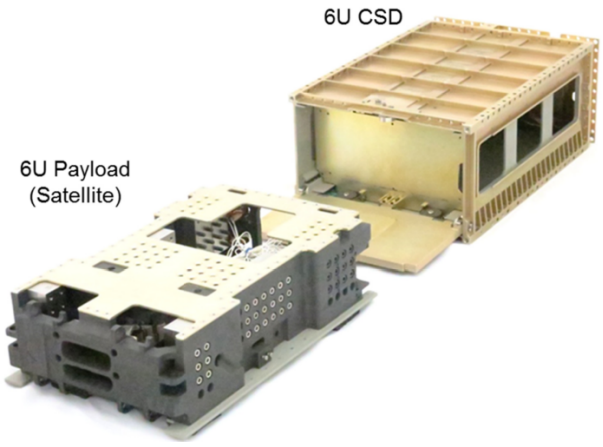

Figure 2.6: CSD for 6U CubeSat [4]

Finally, the NRCSD is the dispenser used to launch CubeSats into various orbits from the International Space Station. Once arriving at the space station, astronauts integrate the satellites into the dispenser for deployment into the desired orbit. The

dispenser has deployed over 170 CubeSats from all over the world, demonstrating the growing commercial value of the station and its platform for international collaboration [28]. The NRCSD uses a rail-based system similar to the PPOD, and can deploy 1U-6U sized CubeSats [29].

2.3 Spacecraft Testing and Failure Mechanisms

Testing a satellite is critical in demonstrating it will survive the launch environment and function properly in space. It is important to understand the types of tests and testing levels required and common problems that are faced so that they can be avoided. Studies show that reducing technical verification and requirements of space systems often results in problems such as high failure rates, schedule delays, and higher costs [30]. Therefore, testing is an effective method of reducing these failures and proving that the satellite is flight-ready. This section gives an overview on the required pre-flight tests and performance criteria of these tests.

2.3.1 Space-Qualifying Testing Methods

Mechanical, thermal, and various other tests are necessary to prove to the launch provider, the program, and the particular sponsor that the satellite is qualified for flight. The specific tests are outlined in NASA-STD-7002A, and include vibration testing, Thermal Vacuum (TVAC) testing, as well as Electromagnetic Compatibility (EMC) and radiation testing [8] [31]. This research is focused on the structural integrity of the CubeSat design, so will cover vibration testing in detail and give a brief overview of the other tests for context.

There are three types of testing levels for spaceflight parts and systems, including qualification, proto-flight, and acceptance testing [8]. Qualification tests the worst case conditions plus a margin, and is typically performed on a prototype model to

demonstrate a suitable design [30]. Qualification tested components or entire systems typically won't fly since they experience loads and environments greater than the worst case predictions, possibly causing damage that could affect future performance. Acceptance testing is much less severe than qualification testing, and certifies proper workmanship [30]. Proto-flight testing falls in-between acceptance and qualification in terms of severity, and is commonly implemented so the prototype model can be used for flight [30].

TVAC and EMC/EMI testing are other practices used to verify the satellite will meet the mission requirements and operate properly in orbit. EMC testing ensures that the satellite as a whole is electrically grounded properly, and that nothing will cause a short circuit during operation. Charge build up across the satellite can damage components, affecting the overall functionality of the satellite. Electromagnetic Interference (EMI) testing ensures that nothing emitted will cause damage or other issues for the mission [8]. The extent of testing and testing levels vary depending on the mission [8]. TVAC testing cycles the satellite through the extreme hot and cold temperatures it will experience upon launch and in the space environment, all while in a vacuum chamber. The range of temperatures that are tested vary depending on the temperature predictions of the mission and the testing level. This thermal environment is considered the most stressful on hardware in terms of fatigue [30]. These extreme temperatures can cause satellite hardware to malfunction or not work properly. Table 2.2 shows required temperature ranges of various bus components, which is important to know and document during the design phase of the mission.

Table 2.2: Typical Temperature Requirements of Various Satellite Components [8]

Equipment	**Operational Temperature (°C)**	**Survival Temperature (°C)**
Avionics Baseplate	−20 to 60	−40 to 75
Batteries	10 to 30	0 to 40
Hydrazine Fuel	15 to 40	5 to 50
Solar Arrays	−150 to 110	−200 to 130
Antennas	−100 to 100	−120 to 120
Reaction Wheels	−10 to 40	−20 to 50

TVAC testing measures the ability of the satellite to function during these extreme temperatures, and ensures the heating and cooling mechanisms are working properly. These mechanisms are installed to mitigate overheating and freezing of components by keeping them within their operational temperature ranges. This type of testing is also important in order to identify materials that may outgas or weaken while in a vacuum [32].

Vibration testing simulates the acoustics and loading that the satellite will experience during launch [8]. A vibration table imparts flight loads on the satellite in all three orthogonal axes, and verifies structural integrity through frequency response analysis [30]. Frequency response analysis generates a frequency response function that shows the structural response to forces as a function of frequency. The output is typically a measure of acceleration, often displayed as Acceleration Spectral Density (ASD) in units of g^2/Hz. The intensity of the tests and the particular testing levels are normally specified by the launch provider. If the launch provider doesn't indicate a loading profile to test to, then the NASA GEVS standard may be followed [17]. This standard encompasses worst-case vibration and shock loads expected during launch [17]. The NASA GEVS random vibration levels can be seen in Table 2.3, with the acceptance and qualification level profiles plotted in Figure 2.7. Note that a safety factor of 1.6 can be used for these dynamic loading levels if necessary for modeling and simulation purposes. [17].

Table 2.3: NASA Acceptance and Qualification Specifications for Random Vibration [5]

Frequency (Hz)	**Qualification (g^2/Hz)**	**Acceptance (g^2/Hz)**
20	0.026	0.013
50	0.16	0.08
800	0.16	0.08
2000	0.026	0.013
Overall	14.1 G_{rms}	10.0 G_{rms}

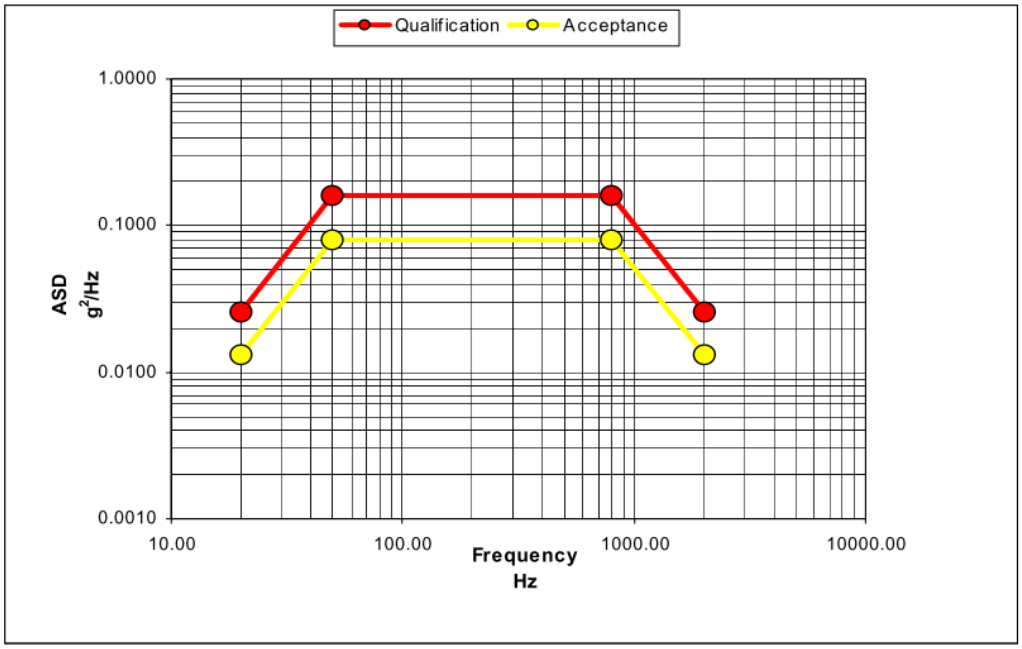

Figure 2.7: NASA Acceptance and Qualification Levels [5]

The vibration testing procedure follows three main steps: an initial sine sweep, random vibration, and post-sine sweep [30]. The satellite is inspected and tested for functionality after each test as seen fit [17]. The initial sine sweep simulates low frequency vibrations that are imparted by the launch vehicle, and is performed to obtain the baseline natural frequencies of the satellite at the low frequency transients [5] [17]. It is typically a 0.25g or 0.5g sweep from 20 to 2000 Hz at a rate of 2 or 4 octaves per minute [17]. A structure's natural frequency is the frequency at which maximum amplification oscillations occur with an applied force. Accelerometers are

attached to various points of interest on the satellite, and these accelerations captured throughout the course of the test are plotted against frequency. The natural frequencies can be identified by the peaks on this graph [5]. A structure's lowest, 1st mode natural frequency has to be higher than the natural frequency of the launch vehicle in order to be qualified for launch. A baseline minimum structural natural frequency that is used is 50 Hz, to ensure it will meet the requirements across all major launch vehicles [33]. Next, a random vibration is conducted, simulating the more intense loads experienced during launch by simultaneously exciting multiple frequencies [5]. For qualification levels, the satellite would experience loads up to 14.1 G_{rms}, according to Table 2.3. To error on the side of caution, most vibration tests start at less intense levels of -12 dB from the baseline and gradually increase to the 0 dB levels that are reflected in Table 2.3. This way, it is easy to identify if components shifted or broke before subjecting the structure to more intense loading. Finally, a post-sine sweep test is performed at the same levels as the pre sine sweep to determine if there were any changes that occured due to the random vibration loads [30]. Pre-random and post-random sine sweeps are compared using the following criteria [17]:

1. Not to exceed (NTE) +/-2 % change in natural frequency (and frequency of any other relatively high-mass modes of vibration)

2. NTE 10% reduction in peak response at the natural frequency

Satellite components normally were broken or shifted (moved) if there is a change in natural frequency between the pre and post sine sweeps that exceeds this criteria. The relationship between natural frequency, mass, and stiffness of a spring-mass structure or system is shown in Equation 2.1 [8].

$$f_n = \frac{1}{2\pi}\sqrt{\frac{k}{m}} \tag{2.1}$$

Where

f_n = frequency (Hz)

m = mass (kg)

k = stiffness (N/m)

Equation 2.1 shows that the frequency is dependent on the system mass and stiffness. A higher natural frequency means a structure responds linearly to loads at frequencies that would cause amplified responses in a lower natural frequency structure. The natural frequency can be experimentally determined with accelerometers through vibration testing or via non-contact methods with a laser vibrometer. A laser vibrometer is an optical transducer that directs a beam of light at an object, and can measure its vibration frequency and amplitude from the back scattered light [34].

One of the ongoing problems that occurs in a vibration loading environment is the loosening of bolted joints [35]. A bolt pre-load is applied to ensure that the parts to be joined remain in contact, and loss of this pre-load is a common failure mechanism that could cause damage to other satellite components [36]. A tool such as a digital torque wrench is used to apply a precise tightening torque to the fasteners of the satellite. The exact torque levels depend on the size, type, and application of the screw, and normally follow a published table of recommended values. In addition to preloading the fasteners, a minimum of one locking mechanism is required for all satellite hardware [16]. This can be accomplished through the use of a thread locking helicoil or staking material such as Loctite, which acts as a glue. These locking mechanisms are not designed to maintain the bolt preload, but rather acts as a safeguard to mitigate loss of fasteners and resist bolt loosening [16]. The type

of fasteners used depends on the mission and requirements, but Torx sockets have proved reliable under high loads and have the ability to transfer more torque on average [37]. In general, fasteners add complexity and potential failure points to a structure, problems that can be mitigated through AM.

2.4 Additive Manufacturing Overview

Additive manufacturing has the potential to reshape the way that engineers approach design problems. The concept of adding material to create a particular structure introduces a wide field of complex design possibilities that otherwise wouldn't be possible. It is starting to heavily influence the aerospace industry, where numerous programs have reduced part count, cut costs, and increased capabilities with the use of 3D printing. Section 2.4 gives a brief overview on the various 3D printing methods, aerospace applications, and design considerations.

2.4.1 Common AM Processes

AM currently consists of 7 main processes, including VAT photopolymerisation, material jetting, binder jetting, material extrusion, powder bed fusion, sheet lamination, and directed energy deposition [38]. Table 2.4 gives an overview of these processes, as well as some advantages and disadvantages of each.

Table 2.4: Classification of Additive Manufacturing Processes [9]

CATEGORIES	TECHNOLOGIES	PRINTED "INK"	POWER SOURCE	STRENGTHS / DOWNSIDES
Material Extrusion	Fused Deposition Modeling (FDM)	Thermoplastics, Ceramic slurries, Metal pastes	Thermal Energy	• Inexpensive extrusion machine • Multi-material printing • Limited part resolution • Poor surface finish
	Contour Crafting			
Powder Bed Fusion	Selective Laser Sintering (SLS)	Polyamides /Polymer	High-powered Laser Beam	• High Accuracy and Details • Fully dense parts • High specific strength & stiffness • Powder handling & recycling • Support and anchor structure
	Direct Metal Laser Sintering (DMLS)	Atomized metal powder (17-4 PH stainless steel, cobalt chromium, titanium Ti6Al-4V), ceramic powder		
	Selective Laser Melting (SLM)			
	Electron Beam Melting (EBM)		Electron Beam	• Fully dense parts • High specific strength and stiffness
Vat Photopolymerization	Stereolithography (SLA)	Photopolymer, Ceramics (alumina, zirconia, PZT)	Ultraviolet Laser	• High building speed • Good part resolution • Overcuring, scanned line shape • High cost for supplies and materials
Material Jetting	Polyjet / Inkjet Printing	Photopolymer, Wax	Thermal Energy / Photocuring	• Multi-material printing • High surface finish • Low-strength material
Binder Jetting	Indirect Inkjet Printing (Binder 3DP)	Polymer Powder (Plaster, Resin), Ceramic powder, Metal powder	Thermal Energy	• Full-color objects printing • Require infiltration during post-processing • Wide material selection • High porosites on finished parts
Sheet Lamination	Laminated Object Manufacturing (LOM)	Plastic Film, Metallic Sheet, Ceramic Tape	Laser Beam	• High surface finish • Low material, machine, process cost • Decubing issues
Directed Energy Deposition	Laser Engineered Net Shaping (LENS) Electronic Beam Welding (EBW)	Molten metal powder	Laser Beam	• Repair of damaged / worn parts • Functionally graded material printing • Require post-processing machine

All of these processes rely on adding layer by layer of material to create a component. The AFIT plastic and metal 3D printers utilize the material extrusion and powder bed fusion methods, respectively. Material extrusion is commonly used in cheaper, smaller 3D printers, where a user can easily design and create a part. This process lays down thin layers with a moving nozzle, and often uses plastics like Polylactic Acid (PLA) or Acrylonitrile Butadiene Sytrene (ABS). These plastics are good for proof of concept designs and practice, but don't translate well to applications where higher strengths are required.

Laser powder bed fusion is a subset of powder bed fusion, and is composed of powder and energy delivery systems that may be used to print metal components [39]. The powder delivery system has two pistons that supply the powder and hold

the part, and a coater that moves the powder from the supply piston to the part piston [39]. The energy delivery system has a laser and scanner, which allows any area of the base build plate to be accessed [39]. The initial layer of powder material is fused together by the laser, and subsequent layers are fused and joined together on top of each other to create the desired part [38]. It has the ability to produce finer features than the other AM processes with the precise focusing capabilities of the laser [9]. During the printing process, the environment over the powder bed is flooded with inert gas to protect it from oxygen exposure and to clear fumes created from the laser path [39]. These AM processes allow for innovative designs and printing of plastics, metals, among other materials.

2.4.2 Printer Compatibility

In order to be compatible with 3D printers, most designs have to be converted from a part file to a .STL file. STL stands for sterolithography triangle language, and simplifies the design into small triangular elements that the slicing software can read [40]. Once saved as a .STL file, a design can be imported into slicing software. Slicing software takes .STL files and orients them on the printer build plate to a desired configuration, sets print parameters such as layer height and print speed, and outputs .gcode or .magics files that the 3D printer can read in. Cura and Magics are commonly used slicing softwares for material extrusion and laser powder bed fusion printers, respectfully. This file saving and transfer process is important to understand and follow in order to successfully print particular designs.

2.4.3 Aerospace Applications and Design Considerations

The aerospace industry has greatly benefited from the application of AM practices, where reducing mass, increasing component capabilities, and cutting costs are

all possible. They have become prevalent in rocket designs, where a printed rocket thruster from Parabilis Space Technologies has shown 50% reduction in material usage and 70% reduction in weight [41]. Commercial company SpaceX has also printed and flown a main oxidizer valve on the Falcon 9 rocket, and demonstrated lower variability in material properties as well as increased ductility, fracture resistance, and strength [42]. Embedded electronics has been another area explored by AM, where system capabilities are increased with the ability to insert components such as sensors, batteries, and electronics into fabricated structures [43]. The insertion of materials isn't just limited to electronics, for AM can print hollow shapes and internal lattice structures that can maintain stiffness while reducing the mass of various components. Some common types of lattice structures include Body-Centered Cubic (BCC), face-centered cubic, octet, Schwarz, and hexagonal. A previous study compared various 3D printed lattice structures and demonstrated that BCC lattices have a high strength-to-weight ratio with the smallest mass on average [40]. All of this past work provides great promise ahead for the capabilities that 3D printed structures can have on CubeSat designs.

Designing a part for 3D printing requires a unique approach and a different way of thinking. Specifications and requirements are critical to consider throughout the design process, as well as trade-offs that will occur. One trade-off that occurs is between layer resolution and scale of the printed part [9]. Higher layer resolution results in a better surface finish, but increases the build time of the part [9]. Layer resolution is affected by layer height, print speed, and other parameters that can be specified prior to printing. The importance of print quality compared to print time would need to be assessed to determine the right balance of print parameters. Most AM processes can only produce a single material at a time, resulting in complications if a multi-material structure is desired [9]. The adoption of some of these multi-

material systems is limited due to uncertainty about the behavior at the material interfaces [9].

Printer capabilities and limitations are important to understand during the design process. For the laser powder bed fusion process on the AFIT 3D printer, certain guidelines and restrictions must be followed to ensure the design is printed successfully without surface flaws or structural issues. One big area of interest is to limit the amount of overhang material for a particular design. Since a particular design is printed from the bottom up (vertical print orientation), issues arise and the metal material starts to sag if there are overhang areas without supports. Support structures can be designed into the part and machined out afterwards, but that adds more time and effort for the machine shop and can make the post processing effort more complex or impossible in some cases. For printers that use a material extrusion process, some support material can be added and dissolved away in a bath after the print is complete. Nevertheless, designs that do not require support structures are desirable when possible. Figure 2.8 shows an example of a design that requires support structure due to some overhanging features.

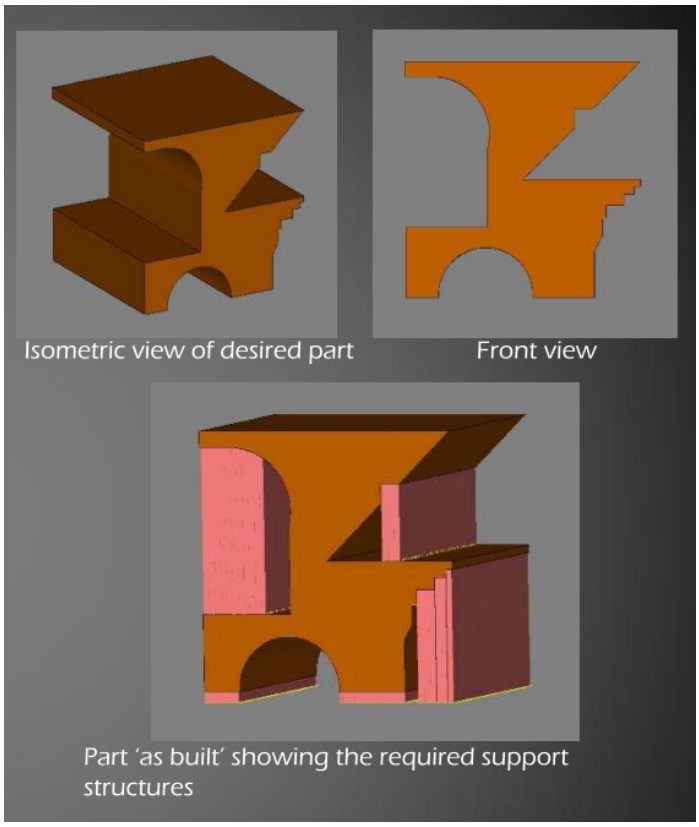

Figure 2.8: Isometric view (top left), front view (top right), and part "as built" showing the required support structures [6]

Other requirements on 3D printed parts include minimum wall thicknesses, minimum angled structures that can be printed without supports, minimum hole diameters, among others. It is generally good practice to not rely on the 3D printers to print holes, but to post process these afterwards at a machine shop. These requirements are particular to the AFIT 3D printer, and may vary depending on the printer and printing method. The following list outlines these design considerations for the AFIT 3D printers [6].

- Minimum wall thickness ≥ 0.1 mm
- Must support angles $< 45°$ off horizontal
- Orient parts to minimize vertical (z) height, 250 mm maximum

Not following these guidelines can result in weaker material properties and structural failures. As long as the design limitations of the printer are followed, 3D printing opens up countless possibilities for complex designs that otherwise couldn't be manufactured. This growing manufacturing technique can lead to reduction in component mass, cost, part count, as well as increasing its performance and capabilities.

2.5 Summary

This chapter supplied some background information to get familiar with the aspects of the problem, covering the basics of CubeSats, testing and failure mechanisms, and additive manufacturing. These are all critical areas to understand in order to design a CubeSat bus design to be 3D printed. The research methodology and way forward will lean heavily on the previous work and review of literature discussed in this chapter. The remainder of this thesis will discuss the methodology used to design the CubeSat structural bus, the results and analysis of these designs, and the conclusions drawn from the results.

III. Research Methodology

3.1 Chapter Overview

The purpose of this chapter is to describe the methodology taken to design a 3U CubeSat structural bus for 3D printing. As satellites become smaller and their functional requirements continue to increase, the need exists to improve the structural bus and utilize 3D printing capabilities to incorporate unique features. The software and equipment necessary to carry out the research will be discussed, followed by the procedures and processes used. The various studies that were carried out to reach the final design are discussed in this procedures section, as well as the vibration testing setup.

3.2 Materials and Equipment

A plastic 3D printer, metal 3D printer, and vibration table are all necessary to print and test the CubeSat structural bus. The CubeSat buses are designed around the capabilities of the AFIT 3D printers. Proof of concept and initial design iterations are printed on the Ultimaker 3 3D printer, which use PLA material. For the metal parts, the Concept Laser M2 Cusing printer at AFIT is used, and currently equipped to print in Inconel 718. In order to be compatible with the PPOD, the bus structure must be 7075, 5005, 5052 or 6061 Al. However, due to funding and safety concerns, the AFIT printer was limited to Inconel 718 during the timeline of this research. The material properties of PLA and Inconel 718 can be seen in the Table 3.1.

Table 3.1: Material Properties of Ultimaker PLA and Inconel 718 [10] [11]

Property	**PLA**	**Inconel 718**
Elastic Modulus (GPa)	2.85	208
Shear Modulus (GPa)	2.41	77.2
Poisson's ratio	0.36	0.29
Mass density (g/cm^3)	1.24	8.19
Yield Strength (MPa)	38.1	1100

Various software is required to design the bus, define the particular print parameters, and analyze the data acquired from vibration testing. SolidWorks is a CAD software that is utilized to create various iterations of CubeSat bus designs that are later printed. A lattice generation software called nTopology Element creates various lattice configurations and patterns that can be inserted inside a particular part. Slicing software Cura and Magics were used for the plastic and metal 3D prints, respectfully. For vibration testing, a MB Dynamics Electro-Dynamic Shaker System C40HP Vibration Table at AFIT is used to subject the bus to a particular set of loading conditions to test it structural integrity. Accelerometers are attached to the part in various locations of interest with bee's wax to measure accelerations throughout the duration of the vibration environment. The vibration table is hooked up to software that provides acceleration vs. frequency plots for the pre-sine sweep, random vibration, and post sine sweep that occurs in the axes of interest. Finally, a MATLAB graphical user interface is used to process and assess the data that occurs from the vibration tests. The extent and details of using these will be explained thoroughly throughout this chapter.

3.3 Procedures and Processes

The design and creation of an CubeSat bus structure that takes advantage of 3D printing capabilities is a broad research topic to tackle that requires a clear direction and scope. For the purposes of this research, one unique 3D printing capability was

focused on to apply on a bus structure. As a result of the literature review, this thesis will focus on the implementation of 3D printed lattices into the walls of the bus structure, with the objective of making a previously solid structure lighter and stiffer. A design of experiments was carried out that led to the generation of the final bus design that is validated through vibration testing. Since the results of these side studies had a direct impact on the final design, their results will be covered in this chapter. These tests included a wall thickness study, lattice selection study, and a structural design decision matrix. The procedures and results of these side studies will be discussed in detail, followed by the vibration testing methodology and experimental setup of the final design.

3.3.1 Wall Thickness Study

Before the lattices can be implemented into the walls of the bus structure, this study is carried out to determine the effects of lattice printability on varying wall thicknesses. A variety of small, 15mm x 15mm x 25mm L shaped test samples were designed in SolidWorks and printed on the Ultimaker 3 in PLA. The plastic 3D printer was used to determine proof of concept, feasibility, and demonstrate printability in order to later translate to AFIT's M2 Cusing metal 3D printer. The Ultimaker 3 has a nozzle size of 0.4mm, therefore wall thicknesses started at 0.4mm and increased up to 4mm. The upper limit of 4mm was a ballpark value chosen as a midpoint between the wall thicknesses of two in house bus structures. These structures varied in wall thickness from 1.5mm to 7mm. In addition to the changing wall thickness, t, the lattice to wall thickness, w_t, and lattice thickness, l_t, were changed. Figure 3.1 shows a top view of a latticed wall, where the crosshatched design represents the lattice structure.

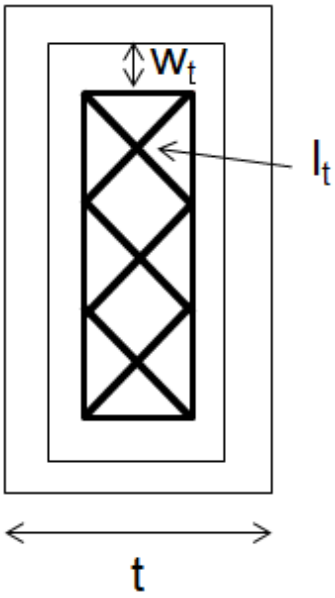

Figure 3.1: Latticed Wall Variable Descriptions

SolidWorks was used to create the lattices, which consisted of a repeating pattern that was cut through the part. In order to be compatible with the 3D printer, they were saved as fine resolution .STL files and imported into the Cura software. All designs were printed with the default setting of the fine print option. Preliminary test prints showed that lattices were unable to be generated within wall thicknesses of less than 2mm. Figure 3.2 shows the printed test samples, with Table 3.2 displaying the lattice parameters used on these articles.

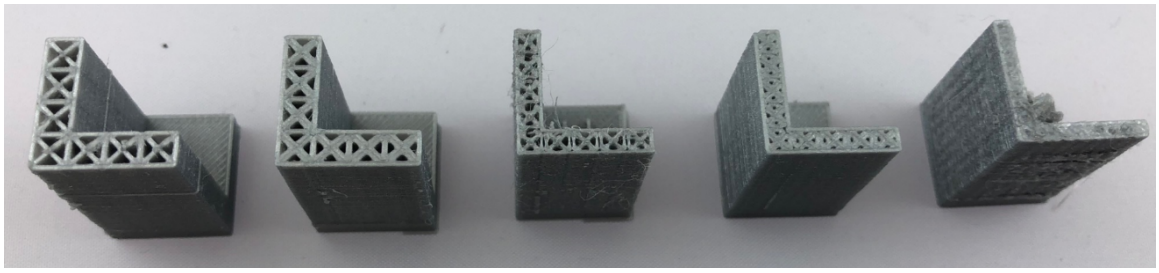

Figure 3.2: Wall Thickness Study Articles 1-5, from left to right

Table 3.2: Wall Thickness Test Article Properties

Article	**Wall thickness, t (mm)**	**Lattice-to-wall thickness, w_t (mm)**	**Lattice thickness, l_t (mm)**
1	4	0.4	0.4
2	4	0.4	0.8
3	3	0.4	0.4
4	3	0.4	0.8
5	2	0.4	0.4

Upon the completion of the test prints, the 4mm walls printed the most consistent, visible, sturdy internal lattice structures. This qualitative determination came from visual inspections of the components. This wall thickness was used for the lattice selection study and for the CubeSat designs.

3.3.2 Lattice Selection Study

The purpose of this study is to determine the best combination of parameters to use for the bus internal lattice structures. For CubeSat and vibration testing applications, a structure with a low mass and high natural frequency is desirable. Therefore, the metric used for the "best" lattice parameter combination is the lowest mass test article that still exhibits an increase in natural frequency. Due to the complexity of modeling lattice structures, these values are determined experimentally. The specifics of the test setup are explained in the following subsection.

Test samples are designed in SolidWorks with dimensions 175mm x 25.4mm x 4mm. The 4mm wall thickness comes from the results of the wall thickness study, and these samples will possess similar lattice parameters. One control test article is used that has no internal lattices, and the other articles contain both SolidWorks and nTopology Element lattice structures inside their 4mm walls. Table 3.3 shows the various lattice parameters for the test articles.

Table 3.3: Lattice Selection Study Test Articles

Test Article	**Lattice generation source**	**Lattice-to-wall thickness, w_t (mm)**	**Lattice thickness, l_t (mm)**
7	SolidWorks	0.5	0.25
7a	SolidWorks	0.5	0.375
7b	SolidWorks	0.5	0.5
7c	SolidWorks	0.25	0.25
8	nTopology Element	0.5	0.25
8a	nTopology Element	0.5	0.375
8b	nTopology Element	0.5	0.5
8c	nTopology Element	0.25	0.25
C4	*N/A*	*N/A*	*N/A*

Note that Article C4 corresponds to the control 4mm wall thickness component with no internal lattice structures. The test articles were designed to print on the M2 Cusing, which can produce more precise and higher fidelity models than the Ultimaker 3. Therefore, the w_t and l_t values varied slightly from the wall thickness study. The lattices in SolidWorks are designed in the same manner as the wall thickness study, as a repeating pattern that cuts through the part. Lattice determination for nTopology Element required some more fidelity, since this powerful software has the ability to generate dozens of different lattice types and parameters. BCC lattices are used, according to previous research that indicates these 3D printed lattice structure have the lowest mass on average [40].

In order to generate a latticed wall in nTopology Element, two separate .STL files have to be imported. An assembly of two separate parts is created in SolidWorks that includes a hollowed out outer shell, and the interior volume that will be replaced with lattice structures. Once this assembly is saved as a fine resolution .STL, the two .STL files are imported into nTopology Element. From there, the internal region is selected and the lattice generated, ensuring it is warped to fit the part. BCC lattices are indicated in the program as cubic vertex centroid, as indicated in Figure 3.3.

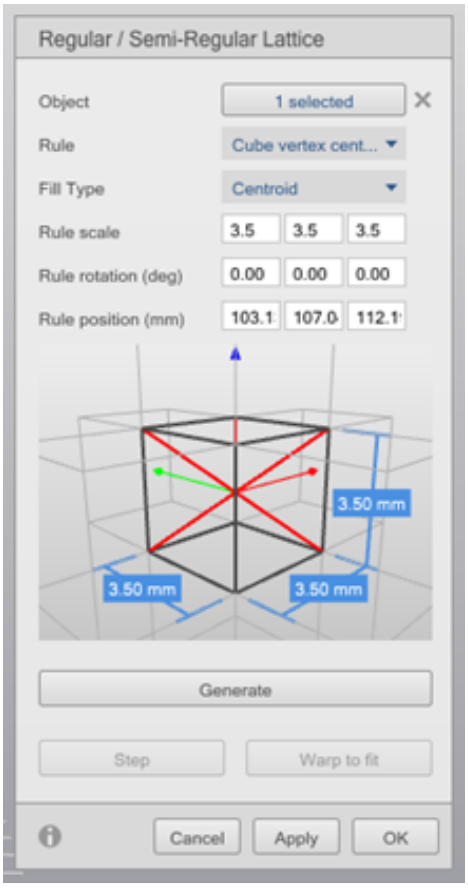

Figure 3.3: nTopology Element Lattice Generation Menu

All of the nTopology Element lattice structures followed a cube vertex centroid rule with centroid fill type. Note in Figure 3.3 that the rule scale corresponds to the dimensions of the cube that the lattice fills. To determine the rule scale used on each article, Equation 3.1 is used. Equation 3.1 allows for the implementation of consistent lattice dimensions relative to the varying lattice parameters for each test article.

$$\text{rule scale} = t - 2w_{\text{t}} \tag{3.1}$$

Where

rule scale= x, y, and z dimensions used for cube enclosing the lattice (mm)

t = total wall thickness (mm)

w_{t} = lattice to wall thickness (mm)

Once the lattice is generated, the lattice is thickened to the designated thickness. Lastly, the mesh of the lattice is generated using the default settings (mesh resolution and node smoothing set to 0) and reduced by 0.5. From there, the test article can be exported from nTopology Element as an .STL for printing. The test articles were sliced using the Magics software, and printed on the M2 Cusing using the print parameters defined in Table 3.4.

Table 3.4: Test Articles Print Parameters on M2 Cusing

Parameter Type	**Power (W)**	**Speed (mm/s)**	**Spot Size (μm)**	**Offset to Original Contour (mm)**	**Trace Spacing (mm)**	**Overlap of Surface Area (mm)**
Advanced Contour	120	280	50	0.09	N/A	N/A
Skin Surface Area	180	800	130	0.095	0.105	N/A
Inner Skin Surface Area	180	800	130	N/A	0.105	0.15
Core Surface Area	370	700	180	N/A	0.13	N/A
Lattice Support	160	1000	50	0	N/A	N/A

Once the parts were printed, the residual Inconel powder was cleaned off of the build plate and then the build plate was sent to the machine shop, where a wire EDM tool cut the articles off from the build plate. 3mm of extra material was added to the bottom of the test article as a tolerance to account for this process. The final test articles are shown in Figure 3.4.

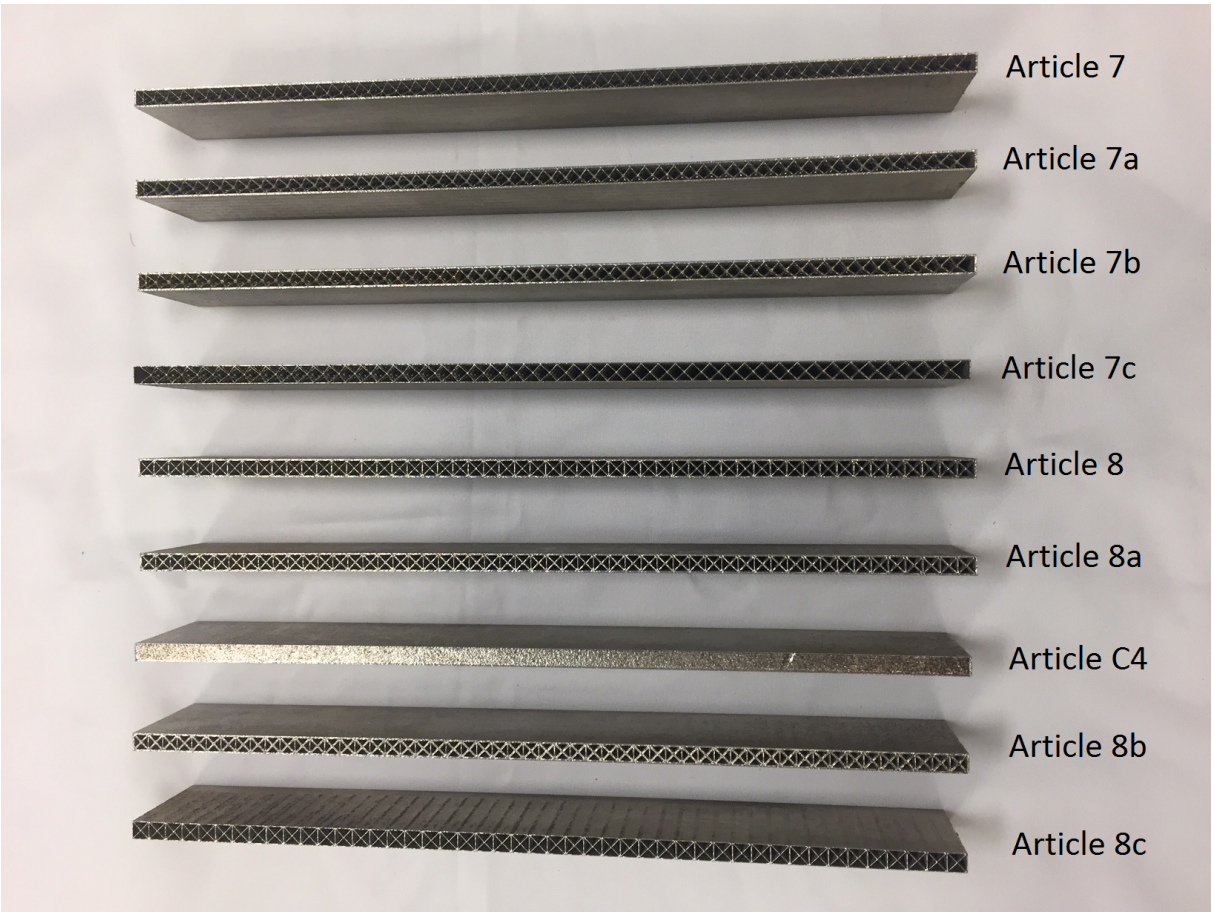

Figure 3.4: Final Test Articles

3.3.2.1 Lattice Selection Test Setup and Results

Experimental natural frequency values for all of the articles were acquired using a Polytec PSV-400 scanning head laser vibrometer. As briefly discussed in the literature review, this non-evasive method directs a beam of light at the sample and measures

its response due to the back-reflected light. Vibrations are inputted into this beam using an acoustic horn excited with a chirp signal. The software then created a grid consisting of small rectangles that encompassed the entirety of the test article. From there, the vibrometer measured the vibration response of each point on the grid, and averaged them to generate the frequency response of the test article. The natural frequencies for various modes of the test article can be determined by the peaks of the frequency response graph. The test articles are suspended by a lightweight wire and attached with clear tape to simulate free-free boundary conditions. This test setup is used to minimize test error and the effects of the boundary conditions on the results, and can be seen in Figure 3.5.

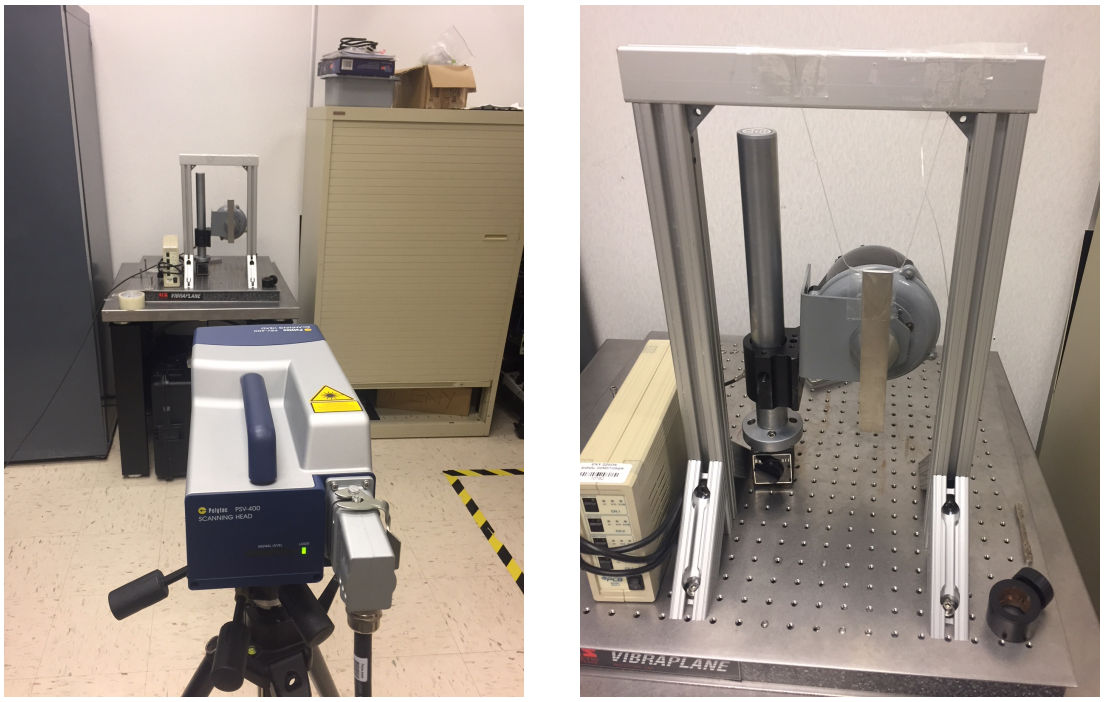

(a) Laser Vibrometer Test Setup (b) Test Article 7 in free-free configuration

Figure 3.5: Lattice Selection Test Setup

Figure 3.6 shows the frequency response graph for the 1st mode natural frequency of test Article C4, followed by Figure 3.7 that shows the 2nd and 3rd mode natural frequency shapes. Similar outputs occurred for the other test articles.

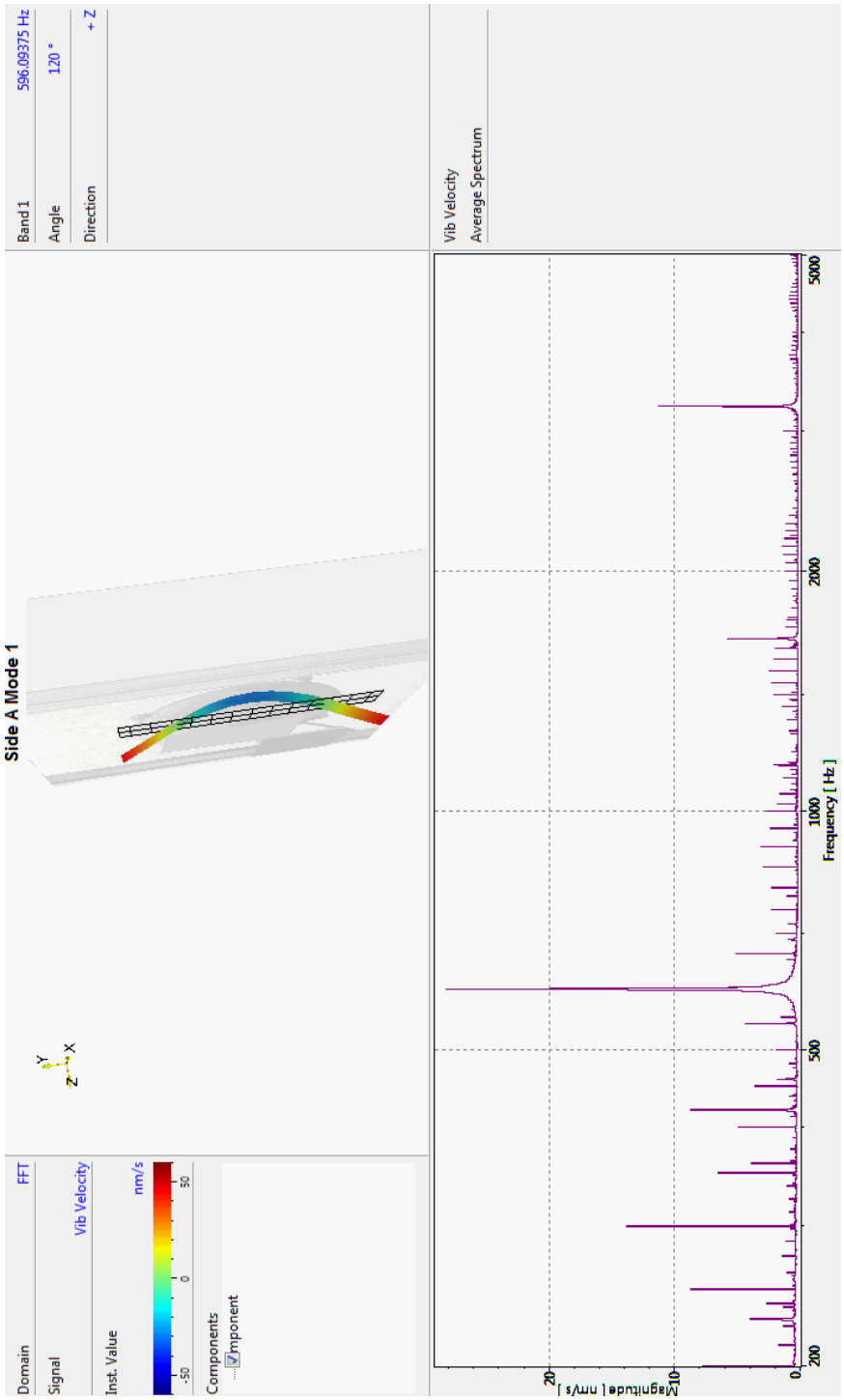

Figure 3.6: Article C4 Mode 1 Response

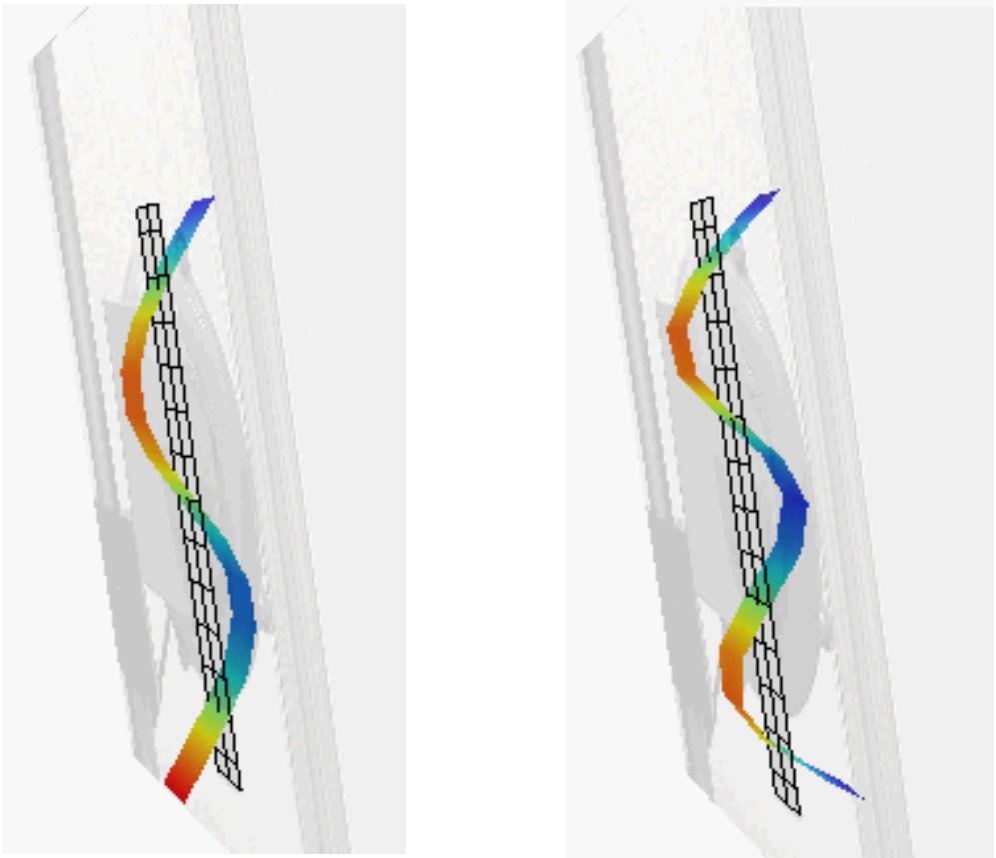

(a) Article C4 Mode 2 Shape

(b) Article C4 Mode 3 Shape

Figure 3.7: Article C4 Mode 2 and 3 Shapes

The large spike in Figure 3.6 corresponds to the first mode natural frequency, followed by the 2nd and 3rd modes with the other large spikes. The beginning of this plot shows some other spikes prior to the first mode natural frequency, which is most likely noise from the test setup. After all of the articles were tested, the optimal lattice parameter combination was selected based on the lowest mass test article that demonstrated an increase in natural frequency. Table 3.5 displaying the results of the vibrometer test.

Table 3.5: Vibrometer Test Results

Test Article	**Actual Mass (g)**	**Frequency (Hz)**	**Stiffness (N/m)**	**Mass Savings (%)**	**Frequency Increase (%)**
7	56.1	697.7	2145.0	60.6	17.0
7a	60.4	693.0	2283.8	57.5	16.3
7b	63.1	675.8	2268.7	55.6	13.4
7c	41.6	651.6	1389.9	70.8	9.3
8	77.6	614.8	2307.6	45.5	3.1
8a	85.6	607.0	2482.2	39.8	1.8
8b	93.9	577.3	2461.9	34.0	−3.2
8c	64.3	573.4	1664.4	54.8	−3.8
C4	142.2	596.1	3976.8	N/A	N/A

The frequencies that Table 3.5 is referring to is the first mode natural frequency. Because of this, a bending constant of 22.4 is applied to the experimental frequency values of each test article in order to back out the stiffness. The masses shown in Table 3.5 are within 5% of the predicted masses for each respective test article. One thing to note is that the mass savings and frequency increases were taken with respect to the control, solid walled Article C4. The results of the data showed that Article 7c had the biggest mass savings and still exhibited an increase in natural frequency. A closer view of this test article is seen in Figure 3.8.

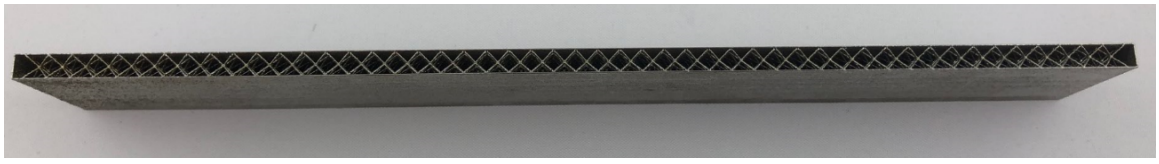

Figure 3.8: Test Article 7c

This component had a mass savings of over 70% and frequency increase of 9% compared to the solid-walled structure. In addition, the natural frequency value of 651.6 Hz for test Article 7c was only 6.6% smaller than the highest natural frequency value of 697.7 Hz in Article 7. The data shows that the nTopology Element generated lattices had higher natural frequencies compared to the SolidWorks articles. Articles

8b and 8c showed natural frequencies lower than the control test article. The data from this test proves the feasibility and advantages that internal lattice structures can have compared to a solid-walled structure. Going forward, the lattice parameters given by Article 7c will be followed for the internal lattice implementation on the final CubeSat bus design.

3.3.3 CubeSat Design Study

With the completion of the wall thickness and lattice selection studies, there is sufficient rationale to implement the Article 7c lattice parameters into the 4mm walls of the CubeSat. Now, the steps taken in the design of the structural bus will be addressed. As stated before, the CubeSat bus is designed with the AFIT 3D printer capabilities in mind. The structure also meets the requirements as specified in the CubeSat Specification Document by Cal Poly [2], including dimensional and material requirements. Three feasible designs were created, and a decision matrix was implemented to determine the optimal design to print. Each of the individual designs are discussed in detail, followed by a description the results of the decision matrix and explanation of the variables used.

When looking at designing a new CubeSat bus structure for 3D printing, it is important to understand the current trends of design and integration techniques for these structures. For the purposes of this research, a Pumpkin structural bus was used as a starting point. The cutouts of the exterior walls of this bus show severe overhang, something that wouldn't be able to 3D print without supports. Therefore, a new pattern was designed in a way to reduce the amount of overhang for 3D printing purposes, while incorporating openings to aid in bus access and component integration. This new cutout pattern is consistent across all design iterations, as well as the filleting of the interior edges of the structure to reduce stress build up. In addition,

all CubeSat designs incorporated a PC/104 hole pattern to allow for integration of electronic stacks.

3.3.3.1 Zipper Design

Due to size limitations of 250mm on AFIT 3D printers, this design involves two 1.5U sized prints that are secured through a zipper-like interface. Two lids are printed separately that attach to the top of the structure to complete integration of the bus. These lids account for the legs at the top of the CubeSat bus, but the bottom legs have to be attached externally. This attachment could come from welding or another creative method, but screwing them on from the inside of the bus isn't a feasible option due to the thickness of the walls and the location requirements for the legs. Hollowing out the bottom legs and screwing them on the bus from the outside presents issues with both the interface of the pusher plate in the PPOD and the attachment of deployment switches. Stacks of electronics can be integrated by dropping them down from the top of the structure, and hooks were added that act as tie down points for cable wires. These hooks are unique 3D printed features added to this design in addition to the internal lattices. The main components of this design are shown in Figure 3.9. The final integration of this design is shown in Figure 3.10, which displays an exploded view of the CAD model.

Figure 3.9: Zipper Design Main Components

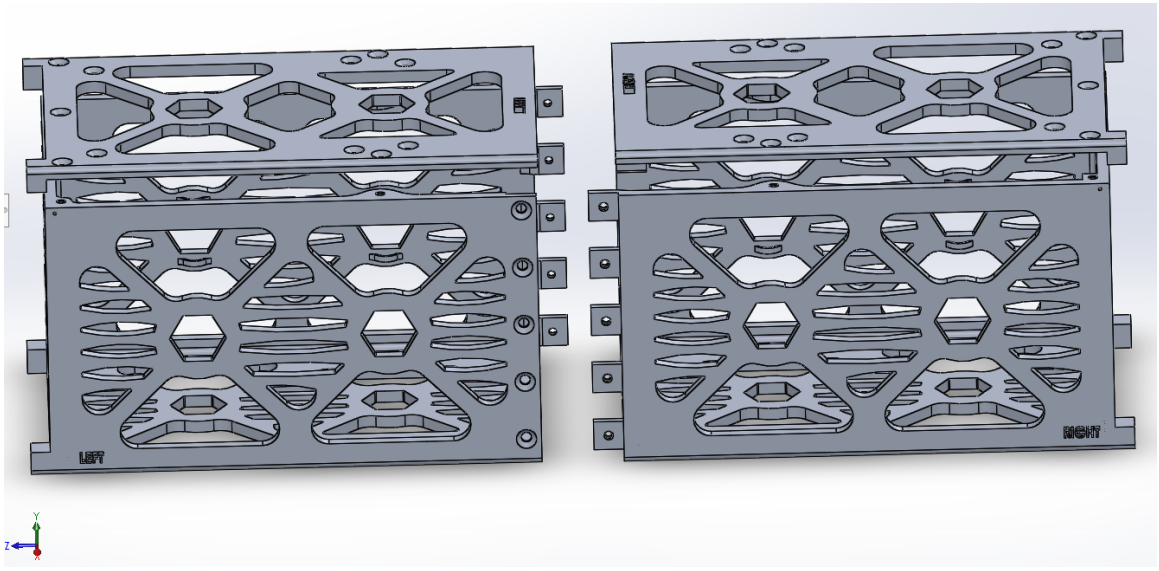

Figure 3.10: Zipper Design Exploded View

These two individual components are printed vertically in the orientation shown in Figure 3.9. This design is printed on the Ultimaker 3 in PLA using recommended settings and 20% grid infill density to demonstrate proof of concept. These proof of concept plastic prints have solid walls with no internal lattices for simplicity and to decrease print time. Table 3.6 outlines the print parameters used on this 28 hour print that deviate from the recommended settings.

Table 3.6: Zipper Design Print Parameters

Parameter	**Value**
Layer Height (mm)	0.2
Wall Thickness (mm)	1
Top/Botttom Thickness (mm)	1
Print Speed (mm/s)	40
Wall Speed (mm/s)	50
Top/Bottom Speed (mm/s)	330
Travel Speed (mm/s)	150

3.3.3.2 Top/Bottom Design

The second CubeSat interface created was a top/bottom design, and can be seen in Figure 3.11.

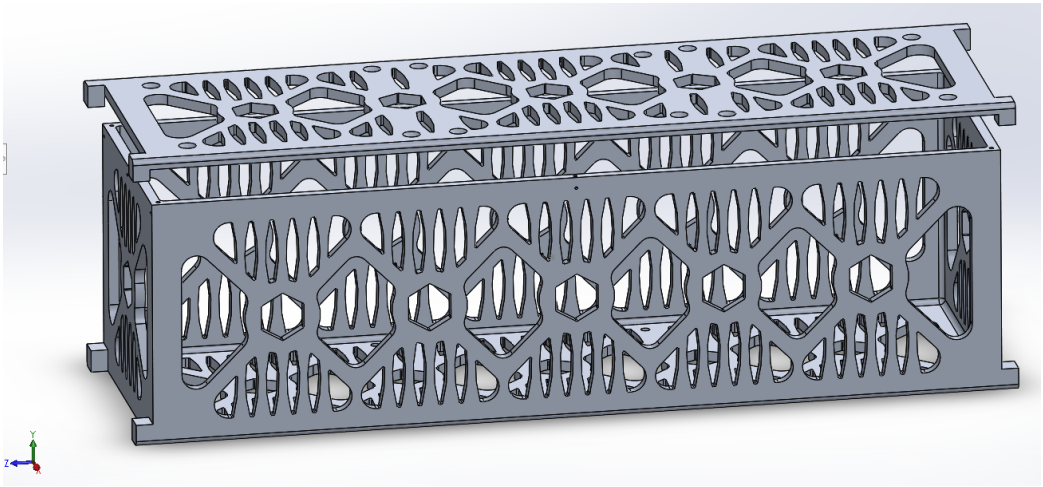

Figure 3.11: Top/bottom design

The bottom bus portion is meant to be printed vertically, with the 3U sized top lid printed as a separate component. The integration of this design involves screwing the top 3U sized lid onto the bottom bus portion. It incorporates a similar cutout design as the zipper interface, with vertical crossbars inserted that minimize the amount of overhang. This design also implements the hooks for cable tie down points. Stacks of electronics can be integrated by dropping them down vertically into the bottom bus, making it easy to access any one particular stack. Unfortunately, due to printer size limitations, a proof of concept print could not be completed.

3.3.3.3 Male/Female Design

The third viable design created can be seen in Figure 3.12.

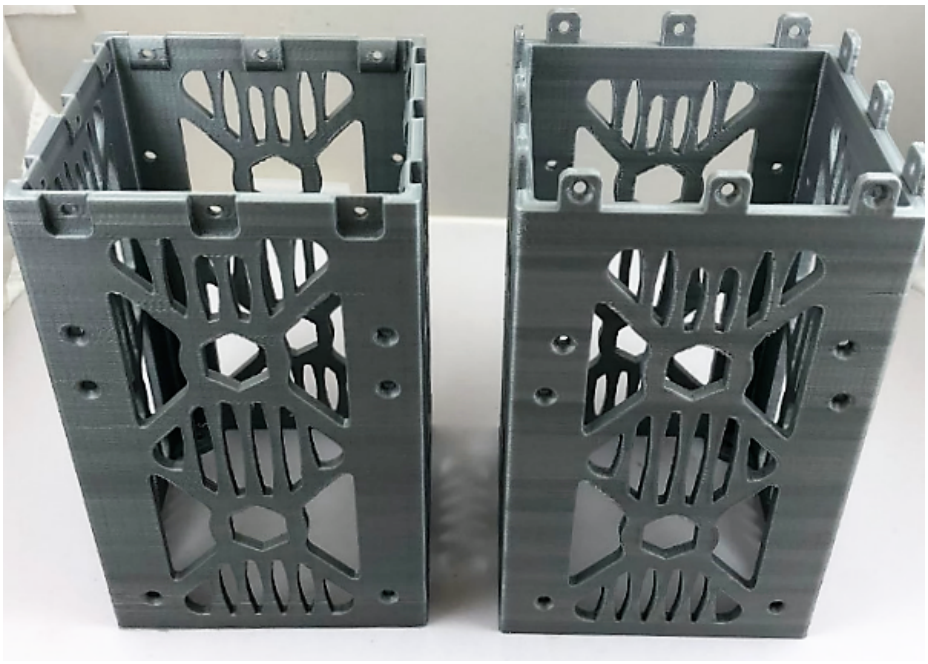

Figure 3.12: Male/Female Components

Note that these two components are printed vertically in the orientation shown in Figure 3.12. This bus structure consists of two 1.5U halves, similar to the zipper design. The male and female portions are screwed together, with lids printed sepa-

rately and attached to the ends of the structure. Because this is a 4-walled structure, the wire tie down straps were not practical to print. The stacks of electronics with this design would have to slide into the bus from the side instead of dropping in from the top, therefore requiring the stacks to be pre-wired prior to integration. For this reason, the wire tie down straps were not feasible to print since they would not be utilized. The print parameters used on this design are the same as those in Table 3.6. The final integration of this design can be seen in Figure 3.13, which shows an exploded view of the CAD model.

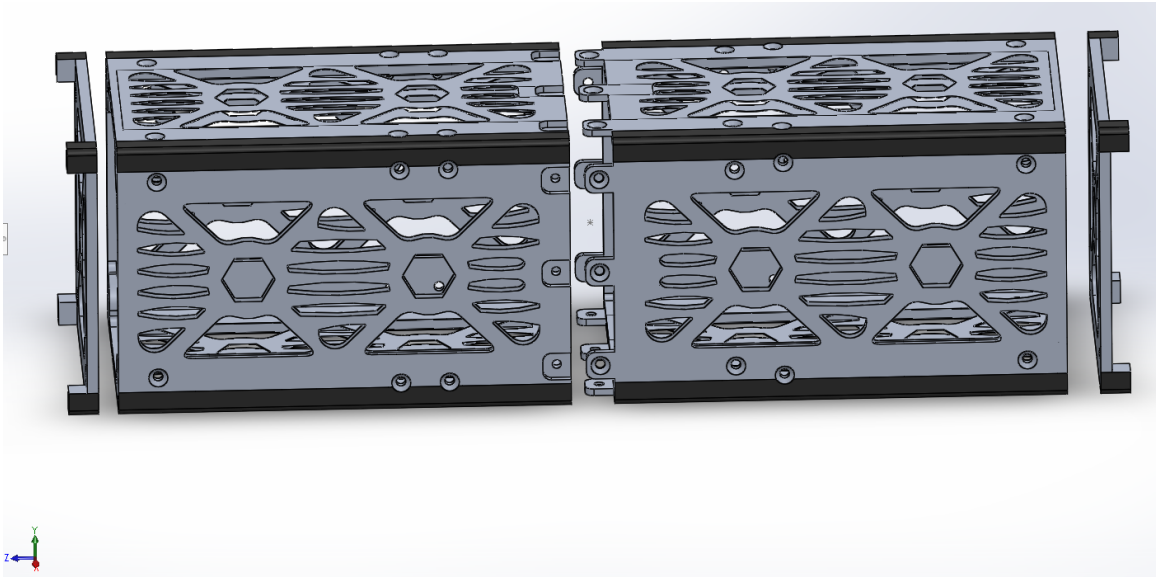

Figure 3.13: Male/Female Integration

All of these CubeSat designs and interfaces were viable options, and the one selected to print in metal comes from the results of the decision matrix, which is discussed in the following section.

3.3.3.4 Decision Matrix

The purpose of the decision matrix is to determine the structural bus to 3D print in metal out of the three design options discussed. Each design is ranked

based on specific qualitative and quantitative criteria, including mass, part count, system integration, cost, and post-processing/printability. Table 3.7 shows the design variables and the scoring ranges.

Table 3.7: Decision Matrix Variable Scoring Chart

Predicted Mass (g)	**Part Count**	**System Integration**	**Cost ($1k)**	**Post-processing/ Printability**	**Score**
≤ 320	≤ 10	10	≤ 1	10	100
$320 - 400$	$10 - 20$	9	$1 - 2$	9	90
$400 - 480$	$20 - 30$	8	$2 - 3$	8	80
$480 - 560$	$30 - 40$	7	$3 - 4$	7	70
$560 - 640$	$40 - 50$	6	$4 - 5$	6	60
$640 - 720$	$50 - 60$	5	$5 - 6$	5	50
$720 - 800$	$60 - 70$	4	$6 - 7$	4	40
$800 - 880$	$70 - 80$	3	$7 - 8$	3	30
$880 - 960$	$80 - 90$	2	$8 - 9$	2	20
$960 - 1040$	$90 - 100$	1	$9 - 10$	1	10
> 1040	> 100	0	> 10	0	0

The range of masses and their respective scores come from an approximation on structural mass efficiency. In general, an efficient structure is 8-12% of the total allowable mass, which is 4 kg in the case of a 3U CubeSat [8]. Therefore, bus structures with masses between 320g and 480g are deemed structurally mass efficient. The smaller the mass of the structure, the more mass available for other subsystems of the satellite. A score drops by 10 points as the mass increases to 2 % higher of the 4 kg maximum mass, i.e 10% of the mass at 400g, 12% of the mass at 480g, etc. The part count variable is a measure of the total number of components each design has. This includes both the components and fasteners necessary to put together the bus structure itself, ignoring fasteners that are external to the bus structure. These external fasteners include those that make up a stack of electronics, since these can vary depending on the mission and the amount of electronics required. The system integration category is a qualitative assessment that surveys 3 technical experts with

experience in CubeSat programs and component integration. The experts rank each design from 1-10 based on ease of access and ability to integrate components. The cost variable is an estimate of the total cost of 3D printing the structural bus. Finally, post-processing and printability is a combined qualitative variable that is similar to system integration. This variable accounts for the effort and manpower required to post machine the part and the compatibility of the design to print on the AFIT 3D printer. Table 3.8 shows the values of each variable across all designs, followed by the final scores in Table 3.9.

Table 3.8: CubeSat Designs Scoring

Design	**Predicted Mass (g)**	**Part Count**		**System Integration**	**Cost ($1k)**	**Post-processing/ Printability**
		Components	*Fasteners*			
Zipper	666.87	8	48	6	3.5	3
Top/bottom	642.35	2	20	8	7	3
Male/female	661.57	4	40	3	3.5	8

Table 3.9: Final Decision Matrix

Design	**Predicted Mass (10%)**	**Part Count (20%)**	**System Integration (20%)**	**Cost (25%)**	**Post-processing/ Printability (25%)**	**Score**
Zipper	50	50	60	70	30	52
Top/bottom	50	80	80	40	30	55
Male/Female	50	60	30	70	80	61

The results of the decision matrix show the male/female design has the highest overall score. The predicted masses of the designs ended up being around the same value, in the 600g range. The masses of each bus design are found from nTopology Element. Once the Article 7c lattice parameters are generated in the walls of the hollowed out structure (using a similar process as the lattice selection test), the final component is exported and saved as a .STL file. The software calculates the total

volume of this .STL file, which is multiplied by the mass density of 6061-T6 Al ($2.7g/cm^3$) to obtain the mass of the structure. With a predicted mass of 661.57g for the male/female design, this makes it about 16% mass efficient. This value isn't too far off from the rule of thumb mass efficiency of 8-12% [8]. Since it is unusual for a satellite to use up the entirety of its allowable mass, this variable is weighted at 10%.

The number of components for each design can easily be seen from the exploded CAD models, with the exception of the zipper design. This exploded CAD model shown in Figure 3.10 appears to only have 4 components, but really has 8 pieces for integration. The 4 bottom legs of the -Y face of the CubeSat bus are unable to print, and need to be externally attached as described in the zipper design section. As for number of fasteners, each CubeSat interface is designed for M3 flat head screws with helicoil inserts. Helicoil inserts are used to satisfy the additional locking mechanism requirement for satellites [16]. The helicoil inserts inside the holes of the male/female part can be see in Figure 3.14.

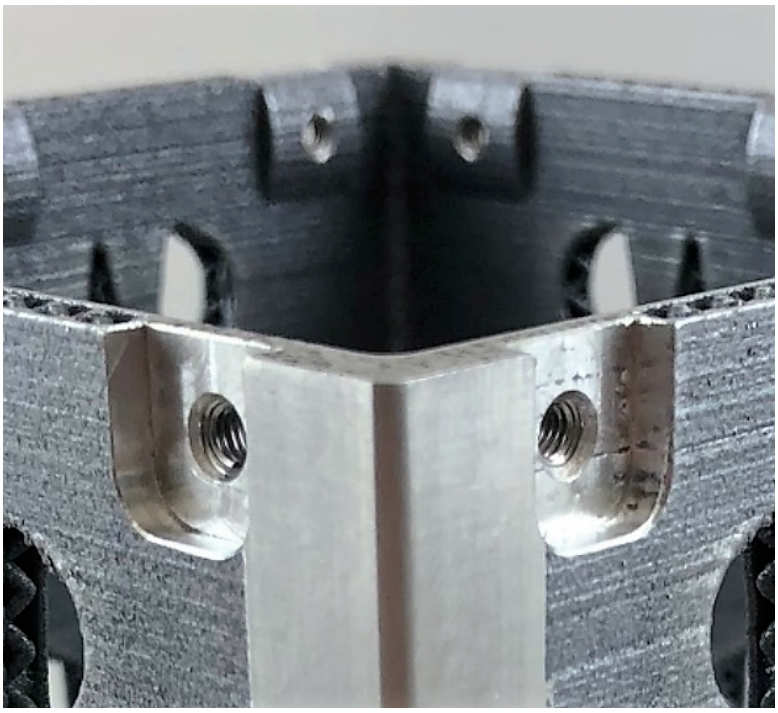

Figure 3.14: Helicoil Inserts on Male/Female Design

While there are only 20 total screws for the male/female design, the total number of fasteners increases to 40 due to the helicoils at each location. The same phenomenon is seen in the other design options. Reduction in part count is an important advantage of 3D printing, which drives the 20% weighting. In addition, fewer components leads to fewer points of failure.

In the systems integration category, the rankings given by the 3 technical experts were unanimous. More open spaces and access points are desirable when integrating components into the bus, something that the zipper and top/bottom design had. Also, it makes it simpler to make repairs to components with an open top design. On the other hand, the male/female design required stacks of electronics to be slid in from the side for integration. With this method, more of the structure must be disassembled to repair internal components. Although it is manageable to pre-wire and integrate stacks in this manner, the repair process can be challenging. A satellite that is easier to assemble requires less manpower, therefore is given a weighting of 20%, the same as part count.

Cost of the zipper and male/female designs was quoted at $3500 by external company Volunteer Aerospace. With larger printers that can build multiple designs at a time, the ability to print within a smaller space results in less material and less cost. For this reason, the vertical print orientation of the zipper and male/female designs is favorable. The top/bottom design takes up more space on the build plate, therefore was estimated at twice the cost. Cost savings is a big advantage in any satellite program, so is given a weighting factor of 25%.

The post-processing/printability category is qualitative, yet has a big impact on schedule and cost. If a particular 3D printed design requires intricate and complex post machining practices, it can delay the part completion date. The printability portion has the same implications as post-processing, where the ability or inability

to print the design on the AFIT printers impacts the delivery of the final product. For these reasons, this variable received a 25% weighting. Hole patterns on 3D printed parts are typically post-processed at a machine shop to ensure precision and to eliminate the chances of anomalies occurring from 3D printing the holes. For the male/female and zipper designs, these interfaces would be machined down to ensure a secure fit. The zipper design presented complications due to the inability to 3D print the bottom 4 legs of the bus. This presented a unique design challenge, as explained in detail in the zipper design subsection. Therefore, this design scored poorly in this category with the inability to meet the dimensional and design requirements. The top/bottom design had a similar outcome, due to its inability to print on the AFIT 3D printers through exceeding the size constraints. On the other hand, the male/female lid requires reasonable machining practices and has the ability to print on AFIT 3D printers. The print parameters of this design and other details are thoroughly discussed in the following section.

3.3.3.5 Final Design and Additional Considerations

As discovered through the decision matrix, the male/female design had the highest overall score and therefore is selected for 3D printing in metal. Understanding that post processing in required after printing the design, extra material is added to various areas of the structure. The lids themselves are machined out of 6061-T6 Al and not printed, so this material addition only applies to the male/female interfaces. Since the male/female portions would get machined down to ensure a secure fit, an extra 1mm of material was added to all sides of this interface as a tolerance. In addition, an extra 2.5mm of material was added to the bottom and top portions of the bus that attach to the lid. This was done to ensure a clean mating surface and to provide a tolerance for cutting the part off of the build plate. Lastly, an extra 1mm was added

to the railings so the machine shop had extra material to meet the surface finish requirement outlined in the CubeSat Design Specification [2].

Now that the extra material is added, a new lattice was generated in the walls of the bus structure using the parameters for Article 7c as outlined in Table 3.3. Generating the lattice in nTopology Element required a similar approach to the lattice selection study, the main difference being the amount of internal structure to fill with lattices. While the lattice selection study filled the entire interior of the test articles with lattices, the male/female design only fills the areas that follow the cutout design with lattices. The openings that were designed into the bus cutout pattern have to stay open to aid in bus access and component integration. Also, safety concerns arise if sharp lattices protrude into the open spaces that hands and fingers may enter in order to access bus components inside the structure. Therefore, the .STL's imported into the software included one that followed the outline of the cutout pattern and the hollowed out exterior shell of the bus. The ligaments of the lattice structures that protruded into the open areas were manually deleted, with great care taken to ensure that lattice structures were still connecting and continuous throughout the design. Finally, the .STLs were sliced and saved as a .Magics file for printing.

Due to machine and material availability, the final design was printed on a Concept Laser X line 1000r metal 3D printer at Volunteer Aerospace as opposed to AFIT's M2 Cusing. Volunteer Aerospace used AlSi10Mg, which is a commonly used 3D printed Aluminum alloy that closely replicates 6061-T6 Al properties. The material properties of both 3D printed AlSi10Mg and machined 6061-T6 Al can be seen in Table 3.10.

Table 3.10: AlSi10Mg vs. 6061 Al Properties [12] [13]

Parameter	**AlSi10Mg**	**6061-T6 Al**
Smallest wall thickness (mm)	$0.4 - 0.5$	N/A
Elastic Modulus (GPa)	70	68.9
Tensile Strength (MPa)	460	310
Mass Density (g/cm^3)	2.67	2.7
Yield Strength (MPa)	270	276

This printed material is a closer match than Inconel 718 with respect to PPOD compatibility material requirements [2]. While some of the printer properties were proprietary to Volunteer Aerospace, the printer properties that were released can be seen in Table 3.11, followed by the printed design on the build plate in Figure 3.15.

Figure 3.15: Final Design on the Build Plate

Table 3.11: Final Design Print Parameters

Parameter	Value
Layer Height (μm)	50
Temperature (°C)	200
Print Time (hours)	35

Volunteer Aerospace was responsible for cleaning and cutting the structure off of the build plate. From there, the component was shipped to the AFIT machine shop for final post-processing. Drawings were created of the male/female interfaces and tops lids for the machine shop as a reference, and can be seen in Appendix A. The final mass of the design came to 900g, which is 36% more than the predicted value of 661.57g. This may be attributed to the minimum printable wall thickness of AlSi10Mg, as shown in Table 3.10. Since design and testing was done on the M2 Cusing, it's possible some of the fine features weren't printable to the same precision on the X Line 1000r, specifically, the 0.25mm w_t and l_t values used for lattice generation. This would result in a thicker pieces than anticipated. Nevertheless, the latticed design demonstrated mass savings compared to a solid-walled bus with the same dimensions and wall thickness, estimated at 1010.05g. This is a 35% reduction in mass compared to the total predicted mass of the male/female design. The actual mass of a solid-walled bus is unknown since it wasn't fabricated, but the latticed design still would show an 11% reduction in mass, assuming a machined solid-walled structure was exactly the same as the predicted mass. Overall, this male/female design proved to overcome the design challenges encountered with 3D printing lattice structures internal to the walls.

3.3.4 Vibration Testing

As stated in the literature review, the purpose of vibration testing is to ensure that the structure can survive the intense loads imparted during launch. Since there is no

designated launch provider in this research, the NASA GEVS profile is used, as seen in Table 2.3. The empty structure is tested inside the PPOD to qualification levels to subject it to worst case scenario loading conditions. First, a pre-random 0.5g 20-2000 Hz sine sweep is conducted for 1 minute at 4 octaves/min. Then, the structure undergoes random vibration for 1 minute, in accordance with the qualification profile in Table 2.3. Finally, a post-random 0.5g 20-2000 Hz sine sweep is conducted for 1 minute at 4 octaves/min. Plots of acceleration vs frequency are generated for the structure, and changes in natural frequencies of $\pm$ 2% or 10% reduction in peak response at the natural frequencies between the pre and post sine sweep are noted. The structure is expected to have a minimum first mode natural frequency of 50 Hz in order to be compatible with most launch interfaces [33]

3.3.4.1 Test Setup

Before testing can occur, the CubeSat is assembled using the male/female interface components, the two lids, a digital torque wrench, and the stainless steel fasteners outlined in Table 3.12.

Table 3.12: Final Design Fastener List

Fastener Description	**Quantity**	**Material**	**Vendor**	**Part Number**
M3 0.5mm x 5mm flat head screw	12	316 SS	Everbilt	900450
M3 0.5mm x 6mm Torx flat head screw	8	316 SS	McMaster-Carr	92703*A*148
M3 0.5 (1D) thread-locking helicoil	20	18-8 SS	McMaster-Carr	91732*A*645

The machine shop installed the helicoil inserts into all countersunk holes prior to delivery, and a 41 cN-m (3.5 in-lb) tightening torque was applied to all fasteners using the digital torque wrench. The torque values imparted on the screws were obtained from a requirements document by Utah State University [44]. The document specifies

different categories of joints, with the fasteners of interest for vibration testing falling under Category 3. Category 3 joints are those that undergo specific performance or functionality testing, and could be single points of failure [44]. The complete table of required torque values that was referenced is in Appendix B. The M3 0.5 x 0.5mm x 5mm were originally ordered as Torx flat heads screws like the 6mm ones, but a back order from McMaster-Carr required a switch to a different vendor. These screws were installed at the male/female interface, while the 6mm screws were inserted into the lid interface to the rest of the bus. The final post-processed, fully assembled structure is shown in Figure 3.16.

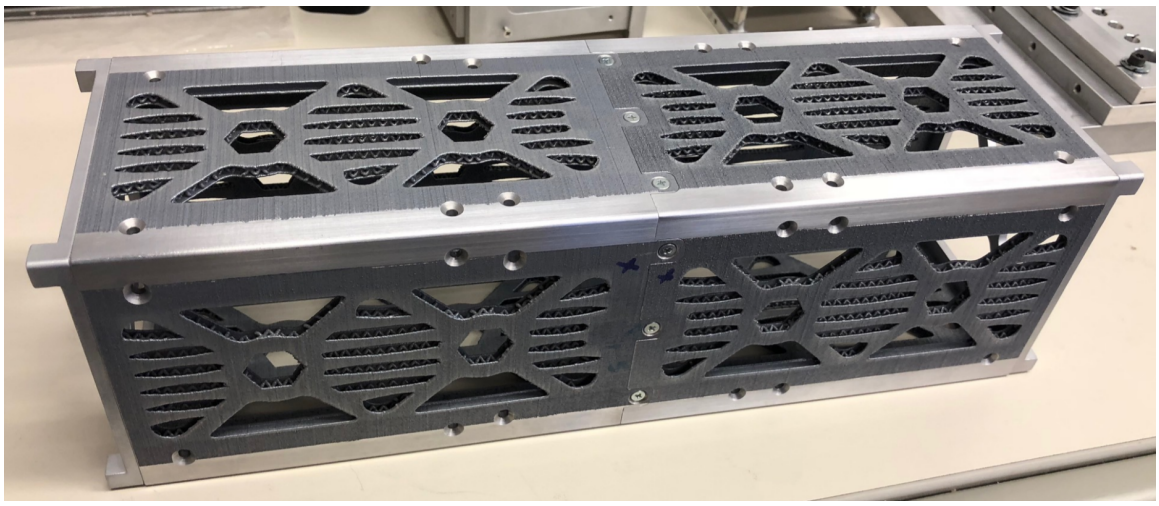

Figure 3.16: Assembled Final Bus Design

The railings have a smoother appearing finish in order to adhere to the surface roughness of CubeSat railings of less than 1.6 µm [2]. After the tightening torque was applied to the fasteners, torque stripes were drawn on the screws. These straight lines drawn on the screw/bus interface helps to identify where the screws were positioned prior to vibration testing. If the fasteners become loose and spin during vibration testing, the torque stripes will indicate a break in the line that wasn't present prior to testing. After the completion of assembly, the 3U CubeSat Acceptance Checklist was completed to ensure it met all the necessary requirements. The completed checklist

can be seen in Appendix C, and did not have any violations. One exception to this is that the railings were not anodized due to time constraints, but this did not affect the dimensions of the structure. Accelerometers are attached to the component using a bees wax, with their locations shown in Figure 3.17.

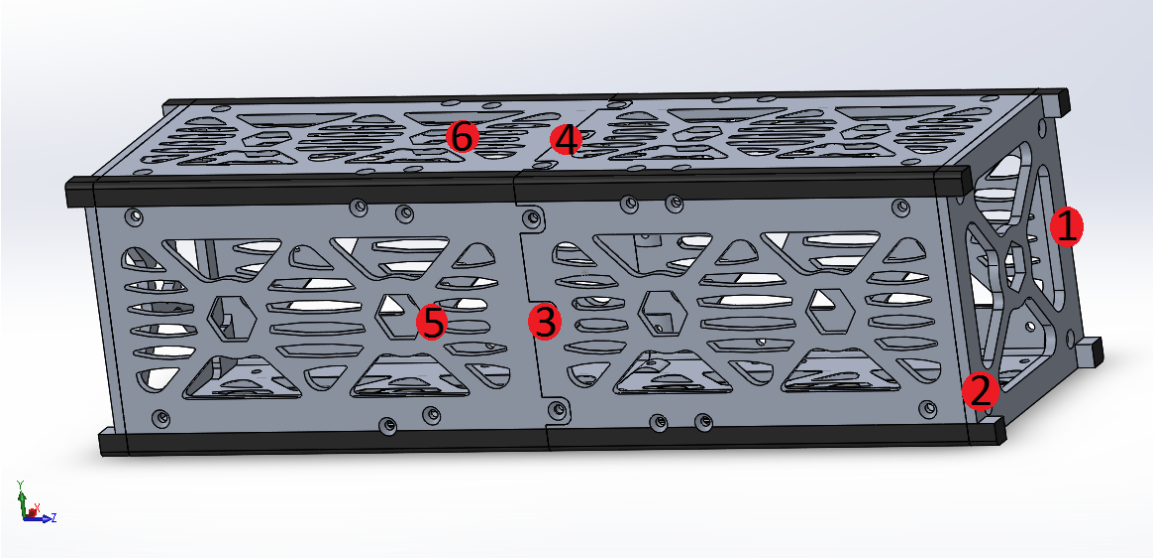

Figure 3.17: Accelerometer Locations

The accelerometers are attached in such a manner as to capture the acceleration in areas where high displacements are anticipated. The locations of the these sensors stayed constant throughout all axes of testing. All of the accelerometers shown in Figure 3.17 are located on the outside of the structure, and loose cables secured with Kapton tape. Axis labels are place on each face of the structure to aid in proper placement of the accelerometers and proper integration into the PPOD. Accelerometer 1 is on the bottom corner of the lid-to-bus interface, with number 2 acting as a control in the middle portion of the lid. Accelerometers 3 and 5 represent similar potential high stress areas, with 4 and 6 replicating the same locations on the + y face. A control accelerometer is placed on the vibration table to measure the response of the table itself. The bus structure is then integrated into the PPOD in accordance with its axis system. The PPOD is bolted to an adapter plate that is then attached

onto the vibration table. All setup procedures were in accordance with the 3U Test Pod User's Guide. Figures 3.18 and 3.19 show the test setup for the x and z axes, respectively.

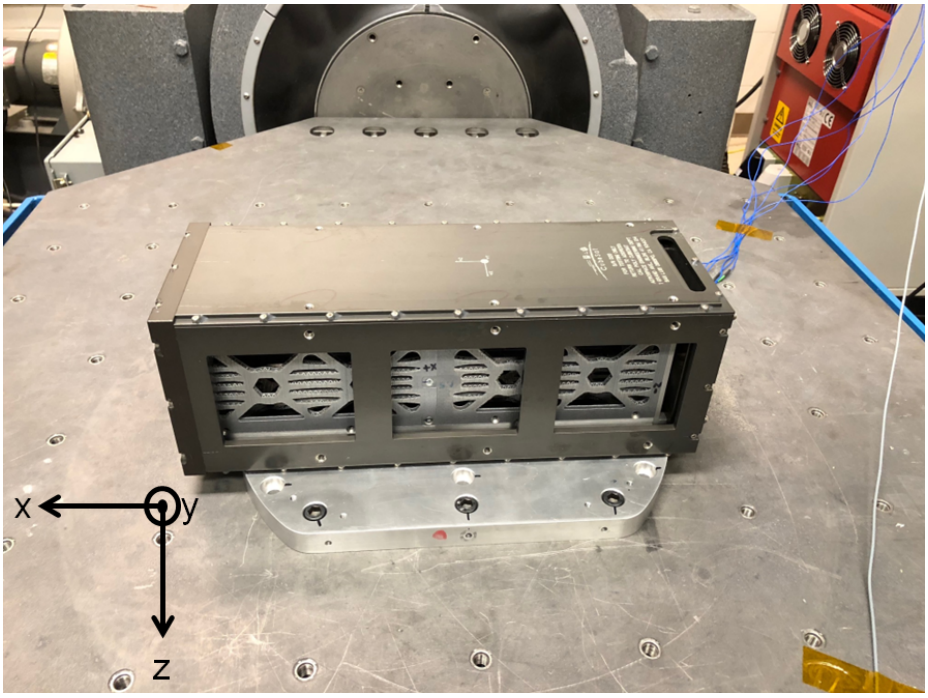

Figure 3.18: X Axis Test Setup

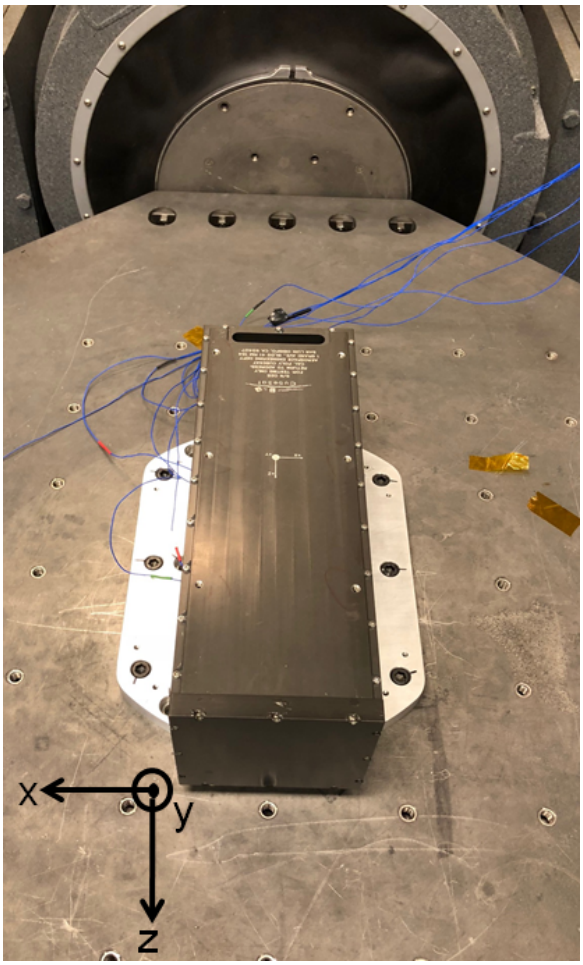

Figure 3.19: Z Axis Test Setup

While most vibration tests involve testing all three orthogonal axes, only the x and the z are necessary for this research. Since the structural design is symmetric about the central axis, the results of y axis testing should be equivalent to the results in the x axis. It is also important to note that the accelerometers of interest are those that are in line with the testing axis (i.e. 1 and 2 for z axis testing and 3 and 5 for x axis testing). The off axis accelerometers will be experiencing transverse loading, which isn't as intense as the axial levels experienced in line with the axis. The results from these vibration tests will be thoroughly explained in Chapter IV.

3.4 Summary

This chapter elaborated on the methodology necessary to successfully conduct the CubeSat structural bus design and test. A brief background of the problem was discussed, since this is imperative to understand thoroughly before coming up with a method to solve the problem. The various software used and required equipment was discussed, as well as their functions. The procedures and processes section discussed the variety of studies that were necessary to obtain the final design, including wall thickness, lattice selection, and the design decision matrix. This chapter also covered the vibration testing levels and experimental setup required to test the structural integrity of the CubeSat design. The remainder of this thesis will present the data obtained from the vibration testing, as well as conclusions and takeaways from this research.

IV. Results and Discussion

4.1 Chapter Overview

The purpose of this chapter is to elaborate on the results of the vibration testing of the 3D printed CubeSat structural bus. The details and observations of each run is thoroughly explained, followed by the results and implications of the data. The data is plotted and compiled using a MATLAB graphical user interface that shows the responses of the pre-random and post-random sine sweeps. The data is obtained from the control accelerometer and the accelerometers attached to the bus in accordance with Figure 3.17. All of the notes and time logs taken throughout the duration of the tests can be found in Appendix D. In addition, the data of the other accelerometers in the x and z axes tests that aren't discussed in this chapter can be seen in Appendix E.

4.2 Z Axis Vibration Testing Results and Observations

The structural bus first underwent vibration testing in the z axis, with the setup shown in Figure 3.19. As previously mentioned, the data of interest is that of the accelerometers aligned with the driven axis. In this case, accelerometers 1 and 2 are in line with the z axis during this test. The data obtained from the test in accelerometers 1 and 2 can be seen in Figures 4.1 and 4.2 respectively.

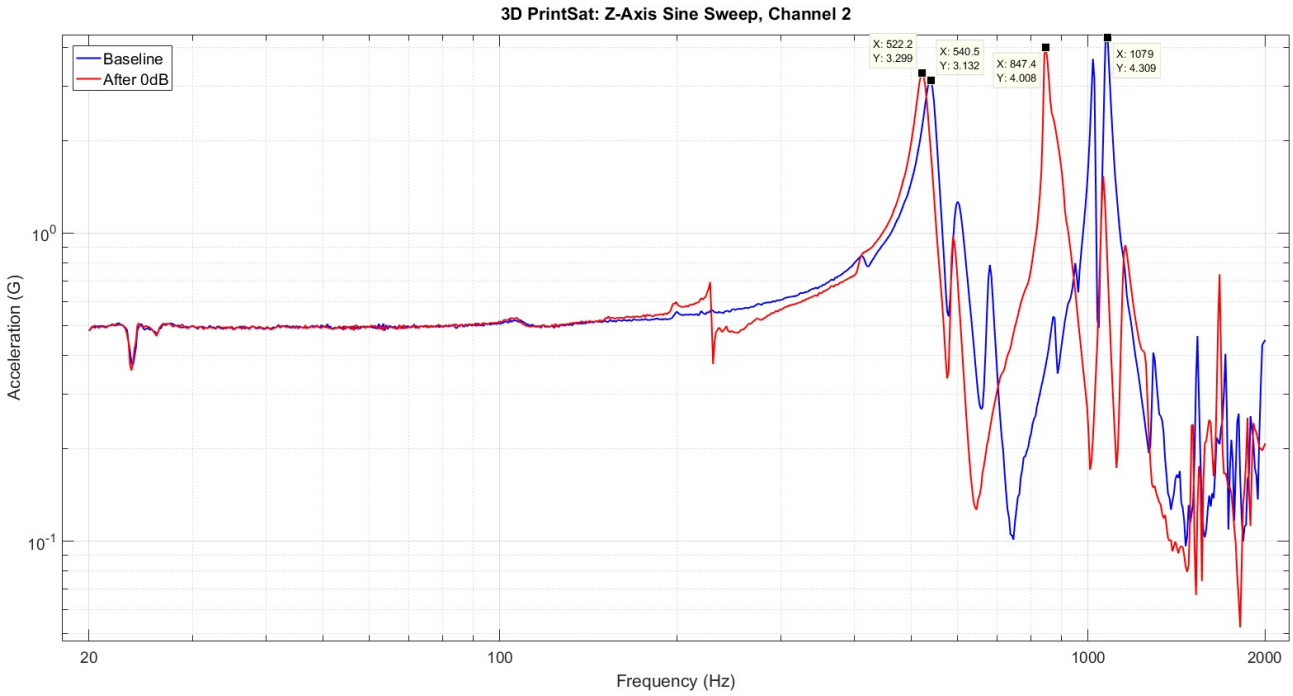

Figure 4.1: Z Axis Run 1 Accelerometer 1 Response

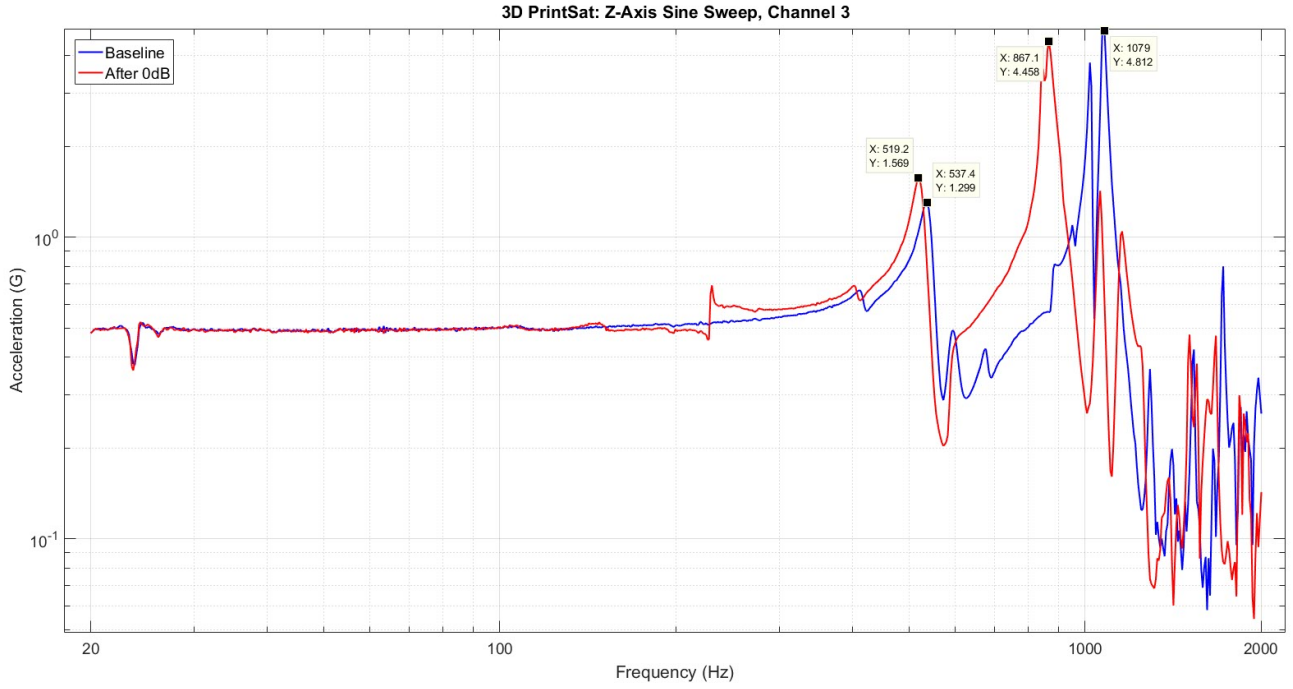

Figure 4.2: Z Axis Run 1 Accelerometer 2 Response

The control accelerometer attached to the vibration table is associated with Channel 1 for the testing data. Consequently, accelerometer 1 corresponds to channel 2, accelerometer 2 corresponds to channel 3, etc. Accelerometer 1 has a first mode natural frequency of 540.5 Hz before the random vibration and 522.2 Hz after the random vibration, as seen in Figure 4.1. These frequencies are much higher than the required 50 Hz minimum first mode natural frequency, demonstrating the structural integrity necessary to survive the launch environment. The accelerometer 2 has a similar response as seen in Figure 4.2, and a summary of the data of interest from this first run can be seen in Table 4.1.

Table 4.1: Z Axis Run 1 Data

Accelerometer		1	2
Mode 1 (Hz)	*pre-sine*	540.5	534.3
	post-sine	522.2	519.2
	% change	-3.4	-2.8
Mode 2 (Hz)	*pre-sine*	1079	1079
	post-sine	847.4	867.1
	% change	-21.5	-19.6
Mode 1 (G's)	*pre-sine*	3.1	1.3
	post-sine	3.3	1.6
	% change	6.5	23.1
Mode 2 (G's)	*pre-sine*	4.3	4.8
	post-sine	4	4.5
	% change	-7.0	-6.3

This test presented a concerning change in natural frequency in both the first and second modes for both accelerometers. Mode 1 showed changes in natural frequency of 3.4% and 2.8% in accelerometers 1 and 2, respectively. In mode 2, shifts of 21.5% and 19.6% occurred for accelerometers 1 and 2, respectively. All of these changes are greater than the 2% shift that's deemed acceptable according to the NASA GEVS standard. In addition, the peak response at the mode 2 natural frequency of accelerometer 2 dropped over 20 %, as shown in Figure 4.2. The structural bus was taken out of the PPOD and analyzed to attempt to determine the root cause for this

issue. A shift in frequency typically indicates that a part was broken or became loose, but further inspection of the structural bus found that this didn't apply. All of the torque stripes still lined up, indicating that the fasteners didn't come loose or need to be re-torqued. The accelerometers also didn't shift or come loose during the duration of the testing. However, upon inspecting the inside of the PPOD, metal shavings were discovered, shown in Figure 4.3. These components were collected in a bag for further evaluation.

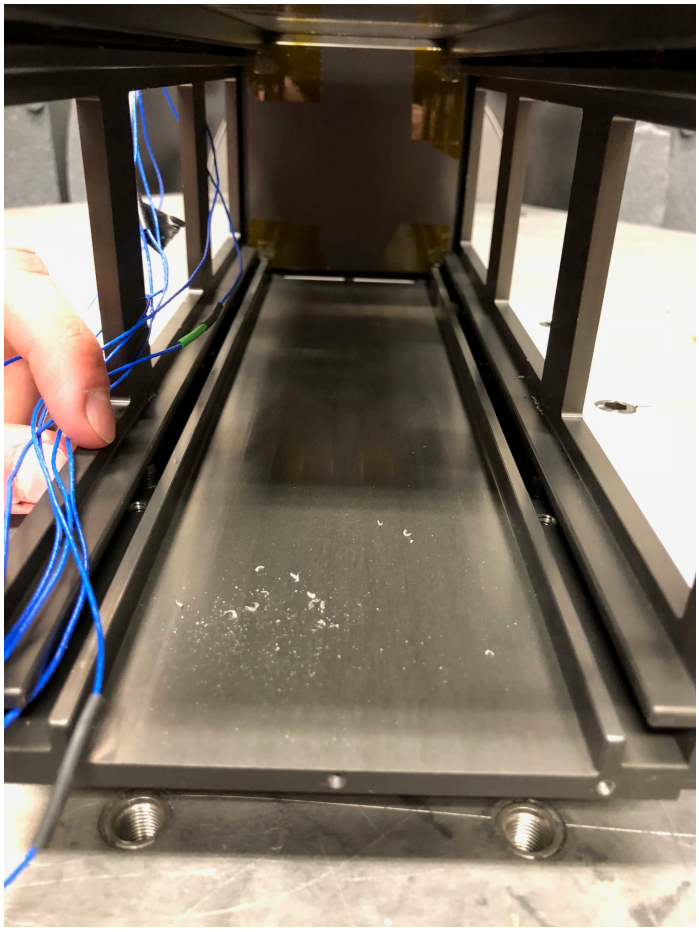

Figure 4.3: Metal Shaving in PPOD

The metal shavings are concentrated towards the front opening of the PPOD, which corresponds to the + Z face of the bus structure. These metal pieces were shiny, indicative of machined 6061-T6 Al rather than 3D printed AlSi10Mg, which

appears rough and gray. Without knowing for sure what these metal pieces were, they were inspected under a microscope at 12X magnification, as shown in Figure 4.4.

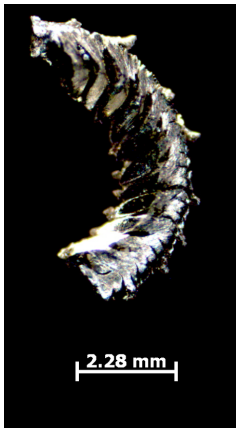

Figure 4.4: Metal Shaving from Vibe Testing

Upon collaboration with the machine shop and experts in the field who have machining experience, the metal shavings most likely came from the post-processed holes, which weren't thoroughly cleaned. The random vibration levels shook these metal leftover pieces loose, leaving them at the bottom of the PPOD after testing. Had there been electronics in the structure, these sharp metal pieces may have caused damage or short circuits.

Due to this unusual finding, a lower -6dB level second random vibration test was conducted followed by a post-sine sweep at 0.5g. The -6dB levels were used to not impart as intense of structural loads on the component, just in case there were broken internal components that couldn't be seen. The responses for accelerometers 1 and 2 for this second run can be seen in Figures 4.5 and 4.6 respectively, where post sine 1 corresponds to the sine sweep conducted after the 0dB random vibration test in run 1, and post sine 2 corresponds to the sine sweep conducted after the -6dB random vibration test.

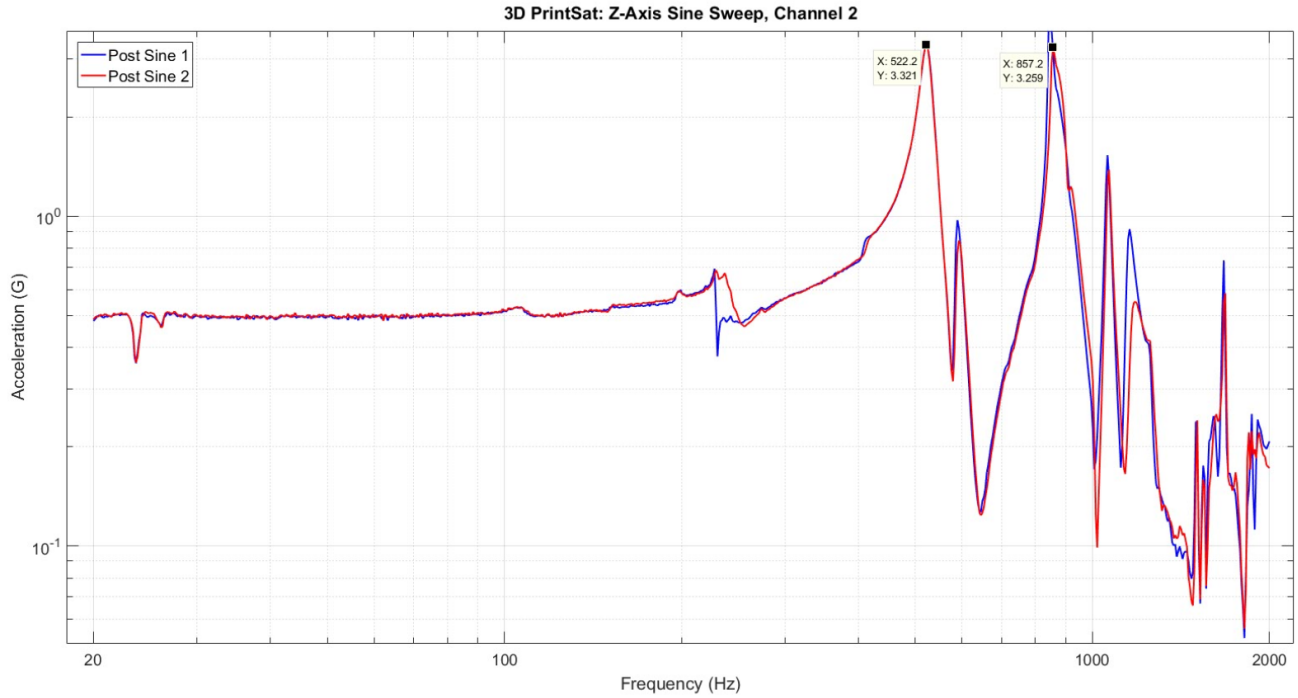

Figure 4.5: Z Axis Run 2 Accelerometer 1 Response

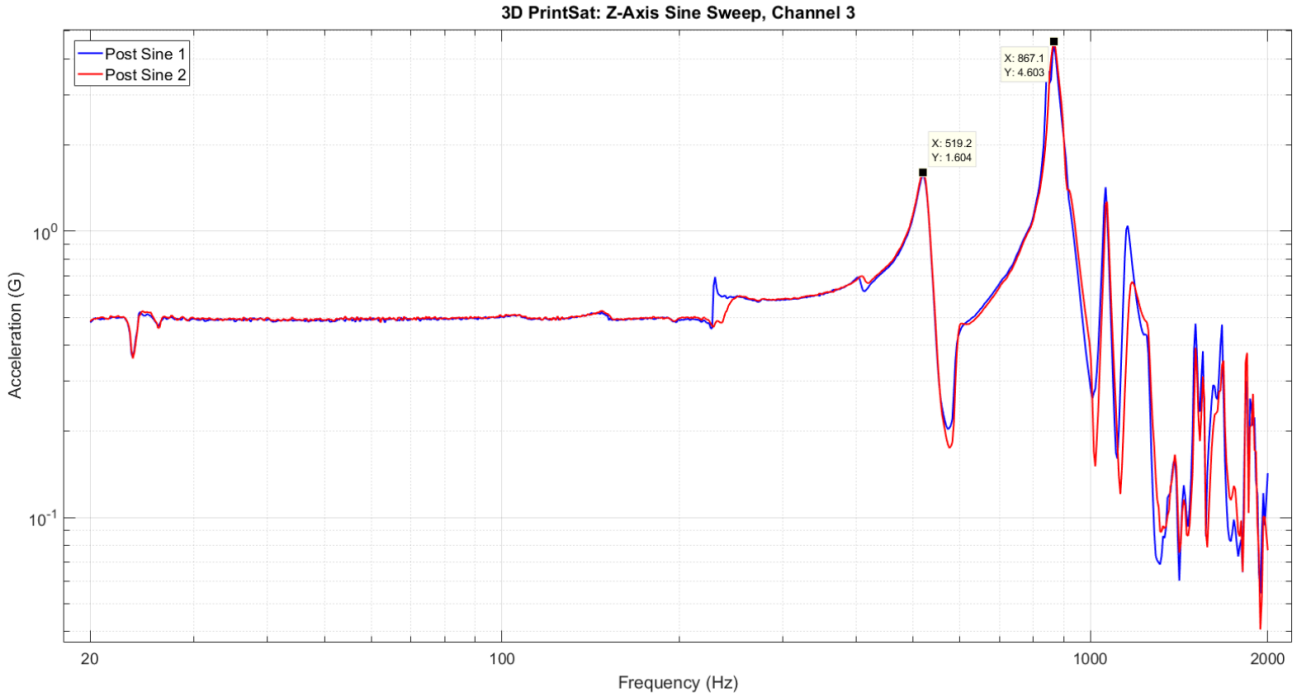

Figure 4.6: Z Axis Run 2 Accelerometer 2 Response

The post sine 1 mode 2 value isn't captured in Figure 4.5, but occurs at 847 Hz with a response of 4 G's. The natural frequencies of both accelerometers exceeded the 50 Hz minimum requirement. Overall, these tests show no major changes in natural frequency in either the 1st or 2nd modes of the structure, which is a positive sign. The one exception falls in the response of the 2nd mode in accelerometer 1, which drops 20% from 4 G's to 3.2 G's. The results of this second run suggested that the shift in natural frequency seen on the first test could've been an anomaly. After reassurance seeing no major shifts in natural frequency or peak response, the pre-sine, random, and post sine levels were repeated on the structure following the same levels as run 1. The responses of accelerometers 1 and 2 for this third run are shown in Figures 4.7 and 4.8 respectively.

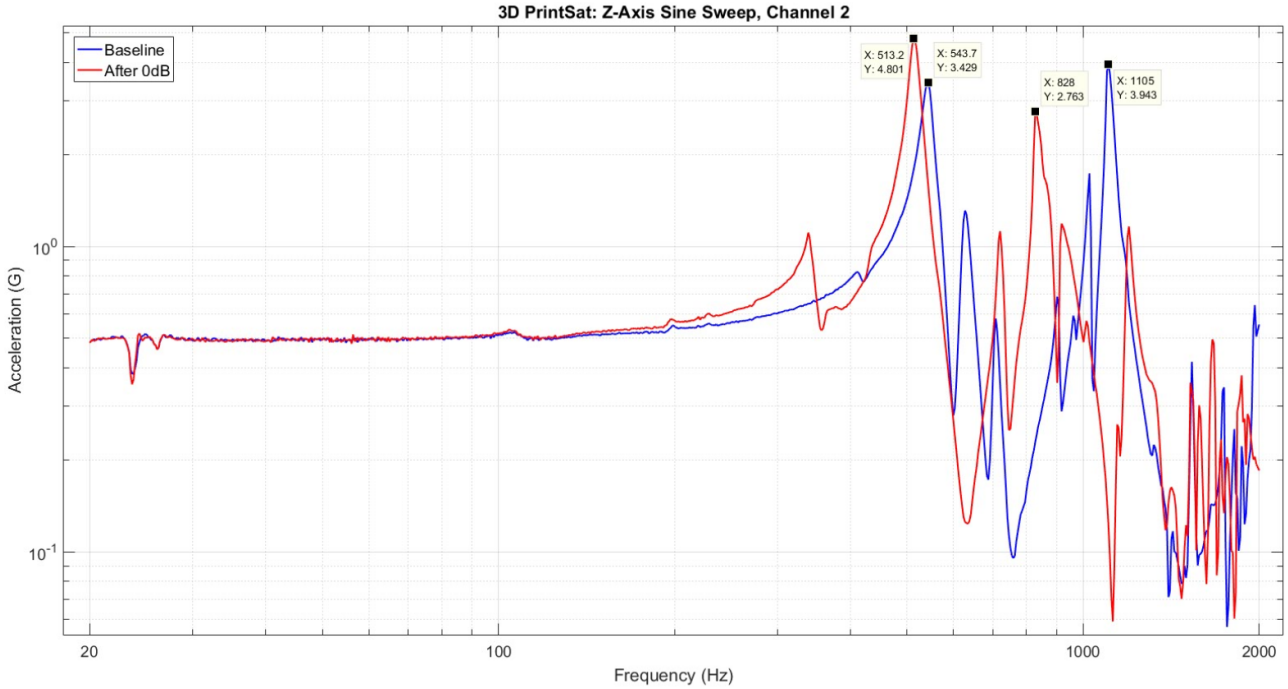

Figure 4.7: Z Axis Run 3 Accelerometer 1 Response

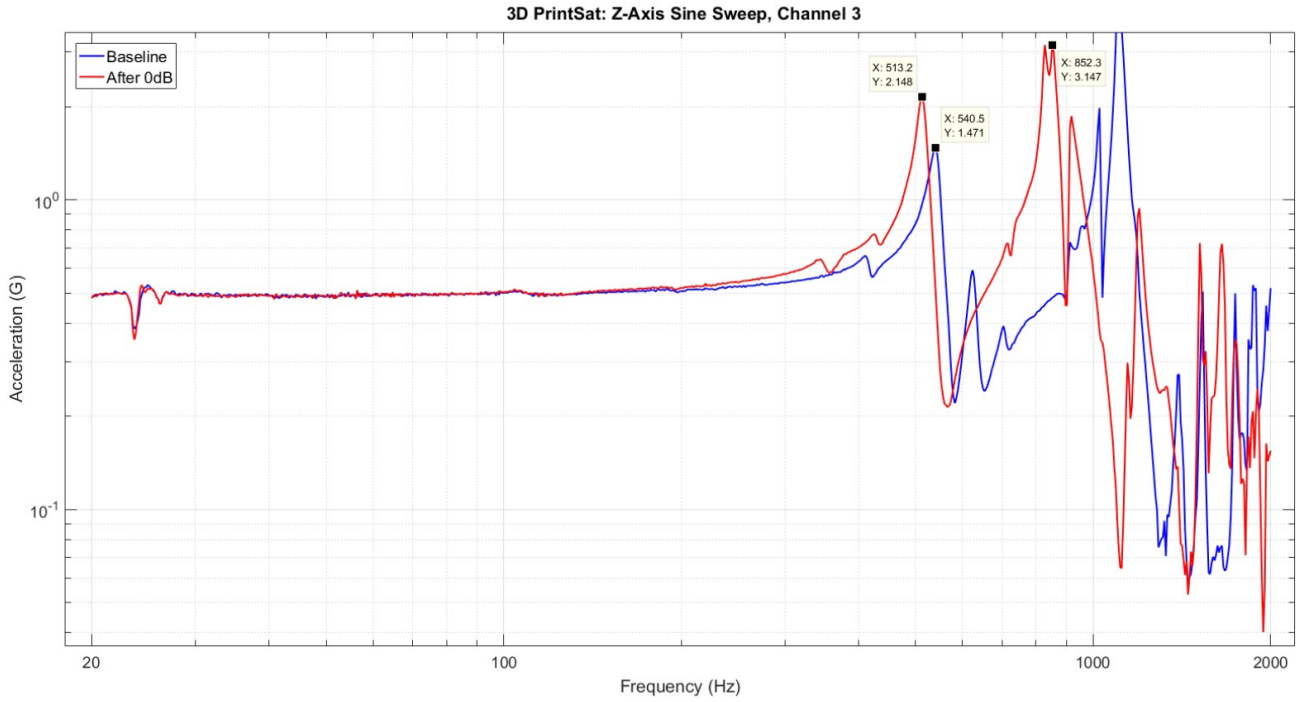

Figure 4.8: Z Axis Run 3 Accelerometer 2 Response

Figure 4.8 doesn't completely capture the pre-sine mode 2 of the structure, which occurs at a natural frequency of 1104 Hz and peak response of 4.6 G's. This third full test sequence showed similar results to the first run, with significant drops in natural frequencies still present in the second mode. Another inspection was conducted and found that the torque stripes were still in the same alignment as they were at the start of the test. The accelerometers were also in the same alignment as the beginning of the test, showing no movement during testing. In addition, more metal shavings were found at the bottom of the PPOD in a similar location. Table 4.2 shows the data obtained from run 3 of vibration testing.

The percent change in frequencies from the pre-sine and post-sine sweeps increased compared to the first run shown in Table 4.1. Also, both accelerometers in run 3 showed a decrease in peak response of over 20% in modes 1 and 2. The reason for the drops in natural frequency is unclear, since there are many factors that could have

Table 4.2: Z Axis Run 3 Data

Accelerometer		1	2
Mode 1 (Hz)	*pre-sine*	540.5	540.5
	post-sine	513.2	513.2
	% change	-5.1	-5.1
Mode 2 (Hz)	*pre-sine*	1105	1104
	post-sine	828	852.3
	% change	-25.1	-22.8
Mode 1 (G's)	*pre-sine*	3.4	1.5
	post-sine	4.8	2.1
	% change	41.2	40.0
Mode 2 (G's)	*pre-sine*	3.9	4.6
	post-sine	2.8	3.1
	% change	-28.2	-32.6

an impact on this phenomenon. A more detailed and thorough investigation would be required to identify the issue, but this fell outside the scope and time constraints of this research. Nevertheless, all three tests in the z axis demonstrated that the structure has a natural frequency higher than the 50 Hz minimum requirement. This also proved that the interface between the top lid and the rest of the 3D printed bus is secure. As stated in the overview of this chapter, the z axis responses of the other accelerometers not discussed in this section are found in Appendix E.

4.3 X Axis Vibration Testing Results and Observations

The x axis vibration test involved the same levels as the 1st z axis test, with the setup shown in Figure 3.18. The PPOD was inspected and cleaned prior to starting, ensuring there was no leftover metal shavings present. The x axis test is mainly concerned with accelerometers 3 and 5, since these are in the same orientation as the direction of the loads that the vibration table imparts on the structure. The responses from this first run on accelerometers 3 and 5 are shown in Figures 4.9 and 4.10, respectively.

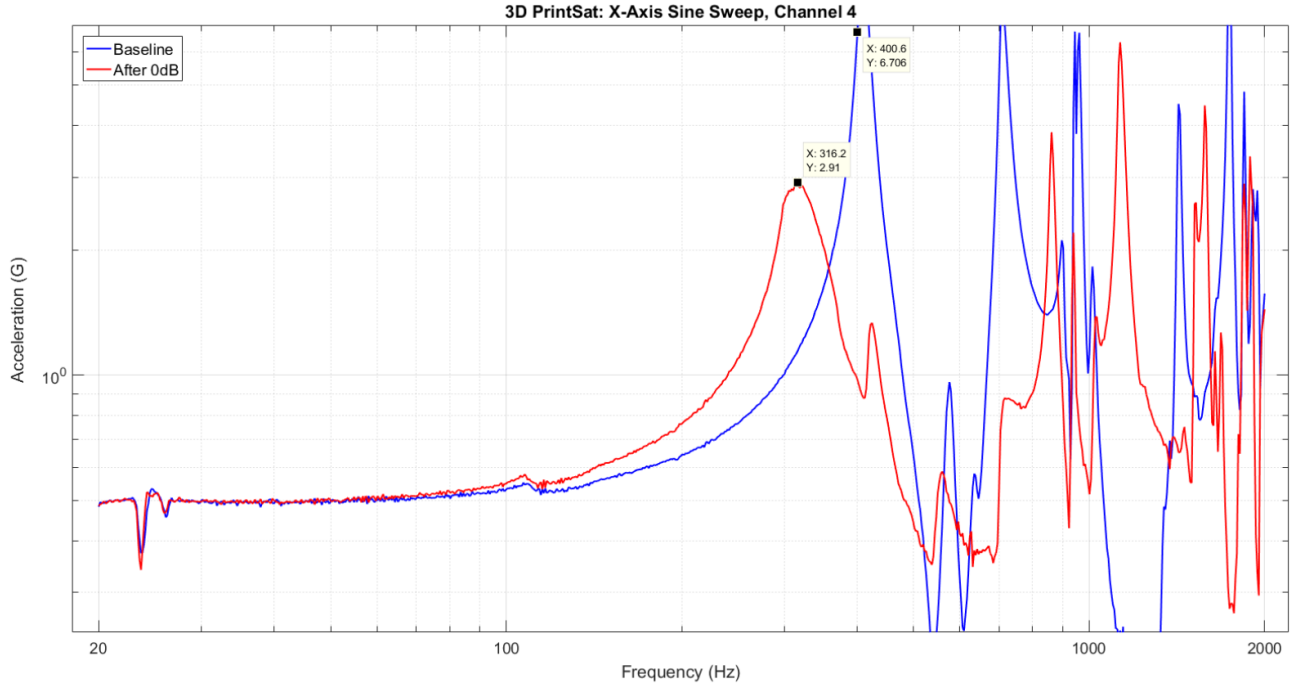

Figure 4.9: X Axis Run 1 Accelerometer 3 Response

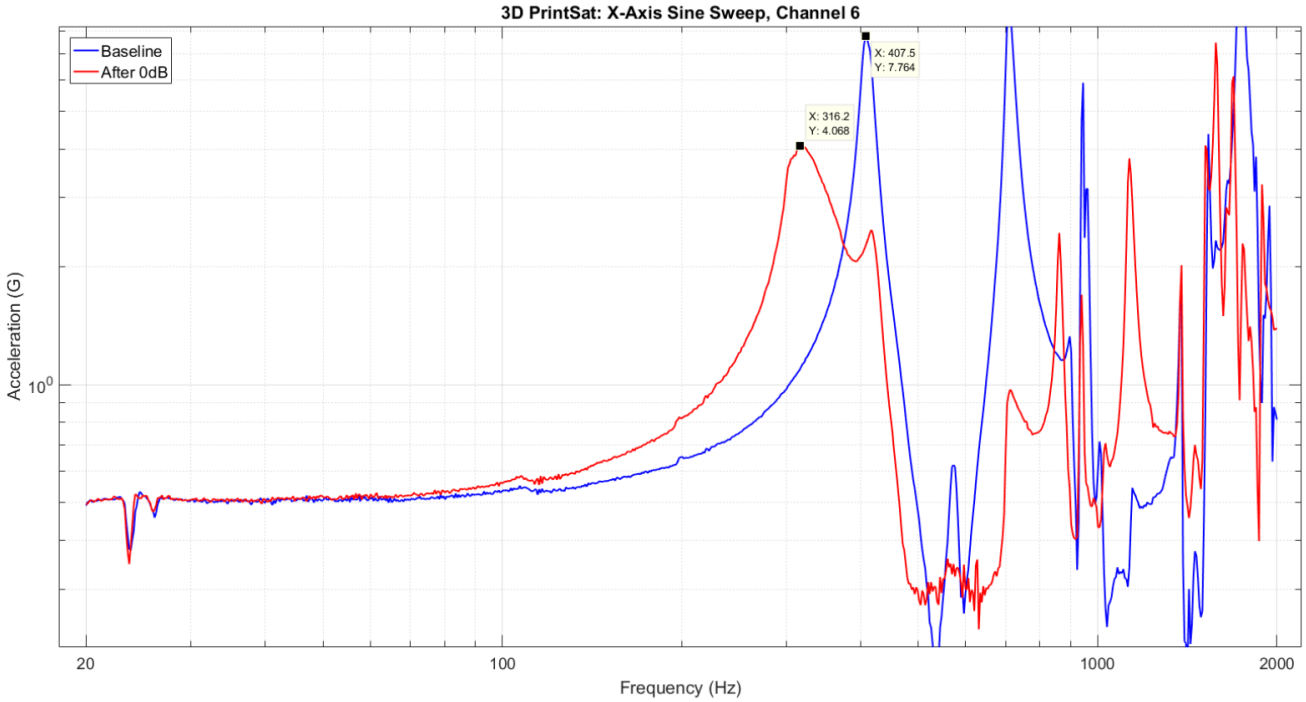

Figure 4.10: X Axis Run 1 Accelerometer 5 Response

The mode 1 natural frequencies for both accelerometers are above the 50 Hz requirement, demonstrating it will survive the launch environment. Figure 4.9 doesn't entirely capture the first mode baseline natural frequency, which occurs at 407.5 Hz with a peak response of 8.9 G's. It is unclear from the plots when the mode 2 natural frequency occurs in either accelerometer. But, compared to the z axis testing, these natural frequencies are much lower. The structural stress at the male/female interface is expected to be more than the structural stress at the lid/structure interface, so this result is somewhat expected. Table 4.3 shows the data resulting from this test.

Table 4.3: X Axis Run 1 Data

Accelerometer		3	5
Mode 1 (Hz)	*pre-sine*	407.5	407.5
	post-sine	316.2	316.2
	% change	-22.4	-22.4
Mode 1 (G's)	*pre-sine*	8.9	7.8
	post-sine	2.9	4.1
	% change	-67.4	-47.4

In addition to the lower natural frequencies compared to the z axis, there is a significant drop in natural frequencies in both accelerometers at over 22%. Also, the peak response at the mode 1 natural frequency decreases by over 67% and 47% for accelerometers 3 and 5, respectively. These are significant changes, and require further investigation in a future study. No additional runs were conducted in the x axis, since similar results are expected during repeated runs, much like what was demonstrated in z axis testing.

4.4 Summary

This chapter summarized the results from the NASA GEVS qualification levele vibration testing of the 3D printed CubeSat structural bus in both the x and z axes. The structure had a first mode natural frequency exceeding the 50 Hz minimum first

mode requirement. Unfortunately, drops in both natural frequency and peak response at the natural frequency values between the pre and post sine sweep was prevalent in this testing, and didn't meet the passing criteria as specified by NASA GEVS. The exact reason for this drop is unknown, and requires extensive future studies. The following chapter will discuss conclusions, recommendations for future work, and lessons learned throughout this research.

V. Conclusions and Recommendations

5.1 Analysis Summary

This thesis first covered the basis of CubeSat designs, requirements, and an overview on additive manufacturing capabilities through a literature review. Information acquired from this background study was leveraged to design and 3D print a CubeSat structural bus. From the background of various AM printed structures and capabilities, internal lattices were selected as a unique feature to 3D print into the bus. These internal lattice structures prove to lower mass and increase the stiffness of a part. The wall thickness used for these lattices was acquired from a study of smaller printed test samples, which resulted in 4mm walls.

From there, a lattice selection study using a laser vibrometer obtained the natural frequencies of various test samples that implemented different BCC lattice parameter combinations. For the application of satellite designs, high natural frequencies and low masses are desired, therefore a frequency to mass ratio was used as a metric for this study. Next, a decision matrix that weighted variables such as mass, part count, system integration, cost, and post-processing/printability was implemented on various CubeSat bus designs. A male/female interface had the highest combined score, which was then 3D printed in AlSi10Mg and vibration tested to NASA GEVS qualification levels. The results of the vibration testing showed that the 3D printed structure did not meet the structural and functional requirements for launch applications. These tests noted shifts in natural frequencies that occurred, but time constraints and the scope of this thesis prevented further analysis on the root cause of these changes.

5.2 Research Significance

This research is significant in paving the way forward for newer, innovative satellite designs. 3D printing makes complex, modular designs possible that couldn't be produced otherwise. The use of AM to print fewer components and unique internal features can reduce cost and turnaround time. The implementation of internal lattices into the walls of a CubeSat bus shown in this research is just one example of the enhanced benefits that 3D printing can provide for satellites. Also, this research demonstrates the first use of metal AM for a CubeSat structural bus. With the space domain continuing to become contested, it remains pertinent to keep the technological edge over our enemies through creative and more capable satellite designs.

5.3 Research Limitations

The biggest limitation of this research was printer size capabilities. Even though satellites are continuing to shift to become smaller and smaller, the more common and practical sizes of CubeSats are 3U and larger. The AFIT metal 3D printer can only print up to a 2U size CubeSat, requiring a unique design challenge for printing two halves to later be integrated together. While the printer used at Volunteer Aerospace is larger and capable of printing up to a 24U in size, the focus from the beginning of the research and throughout the design iteration was to print on the AFIT M2 Cusing. Designing to print on a larger printer from the beginning would eliminate these size constraints, where different interfaces and print orientations could be explored that increase functionality while still reducing mass, cost, and number of components.

5.4 Recommendations

Although it wasn't a requirement for this research, a good understanding and background of CAD fundamentals would have been helpful. Designing components, especially for 3D printing, required many iterations and an outside the box way of thinking. The SolidWorks CAD software is user friendly, but it is helpful to know some of the tricks and shortcuts available to make the designs more modular. This approach allows for small adjustments to be made that don't require a rework or redesign of the entire structure. Also, it would've been helpful to fully explore the intricacies of the nTopology Element software. Time constraints and limited experience with this software resulted in relatively basic uses, even though the software has extremely powerful lattice generation capabilities.

5.5 Future Work

There are many direction that this research can be continued as future work. The biggest problem area that arose in the results of the vibration testing was the drop in natural frequencies. The reason for the drops are unknown, and would be an interesting topic to tackle. CT scans of the structure could potentially identify damaged internal structures, if any, and the use of an electron microscope could identify further voids in the 3D printed structure itself. Along the same lines, material properties of the 3D printed, AlSi10Mg can be tested and compared to machined 6061-T6 Al, followed by an analysis of the effect that various printing parameters have on the final strength, size, and accuracy of a desired design. Lastly, the interface between the PPOD and CubeSat bus could've had an impact on the test results, and would be an interesting issue to investigate. All of these factors could have played a role in the drops in natural frequency, but time constraints and the scope of this research prevented further analysis.

Another topic that can be explored is the modeling of the structural bus. Modeling using finite element analysis methods was outside the scope of this thesis, for structural performance was tested experimentally. An in-depth understanding of finite element analysis would be required to model the complex lattice designs present throughout the walls of the structural bus. The ability to accurately model this structure would be a great benefit to the Air Force and satellite industry, for external loads, structural performance, and other characteristics of complex lattice structures could be modeled and predicted prior to experimental testing.

Using BCC lattices proved to reduce mass and increase stiffness of the bus structure, but it would be interesting to explore alternate lattice types to implement. While this research conducted a lattice selection study to identify the optimal combination of BCC parameters to implement, the use of other lattice structures such as octet, Schwarz, and hexagonal could have a different impact on performance. In addition, research into a multi-material structure could have an impact on structural performance.

Another area to explore is varying the wall thickness of the bus structure. 4mm walls were chosen for this research based on the ability to print internal lattice structures in plastic as a proof of concept. With more flexibility and freedom during the research process, the boundary could be tested on how thin of walls with internal lattices could be 3D printed, while maintaining appropriate strength and stiffness values. The thinner walls would allow for increased payload volume and a lighter structure, yet the proof of concept is difficult to test on plastic 3D printers ahead of time.

Testing of the bus structure with integrated satellite components in a flight ready configuration would be another useful study. This research focused exclusively on testing an empty structural bus, so loading it with stacks of electronics and a pay-

load would allow for a more representative testing environment of the CubeSat. In addition, conducting additional tests such as TVAC and EMC/EMI on the entire loaded structure would provide a better understanding on if the CubeSat can survive all aspects of the launch and space environments.

Lastly, utilizing the techniques from this research and applying it to an actual satellite program could be explored. Rather than relying on standard COTS parts that may be rigid and costly, printing these components could save time, cost, and money. The bus could also be designed for integration into other deployers such as the CSD, or NRCSD. In addition, future designs could focus on designing the bus around a particular payload or another subsystem of the satellite.

Appendix A. Final Design Drawings

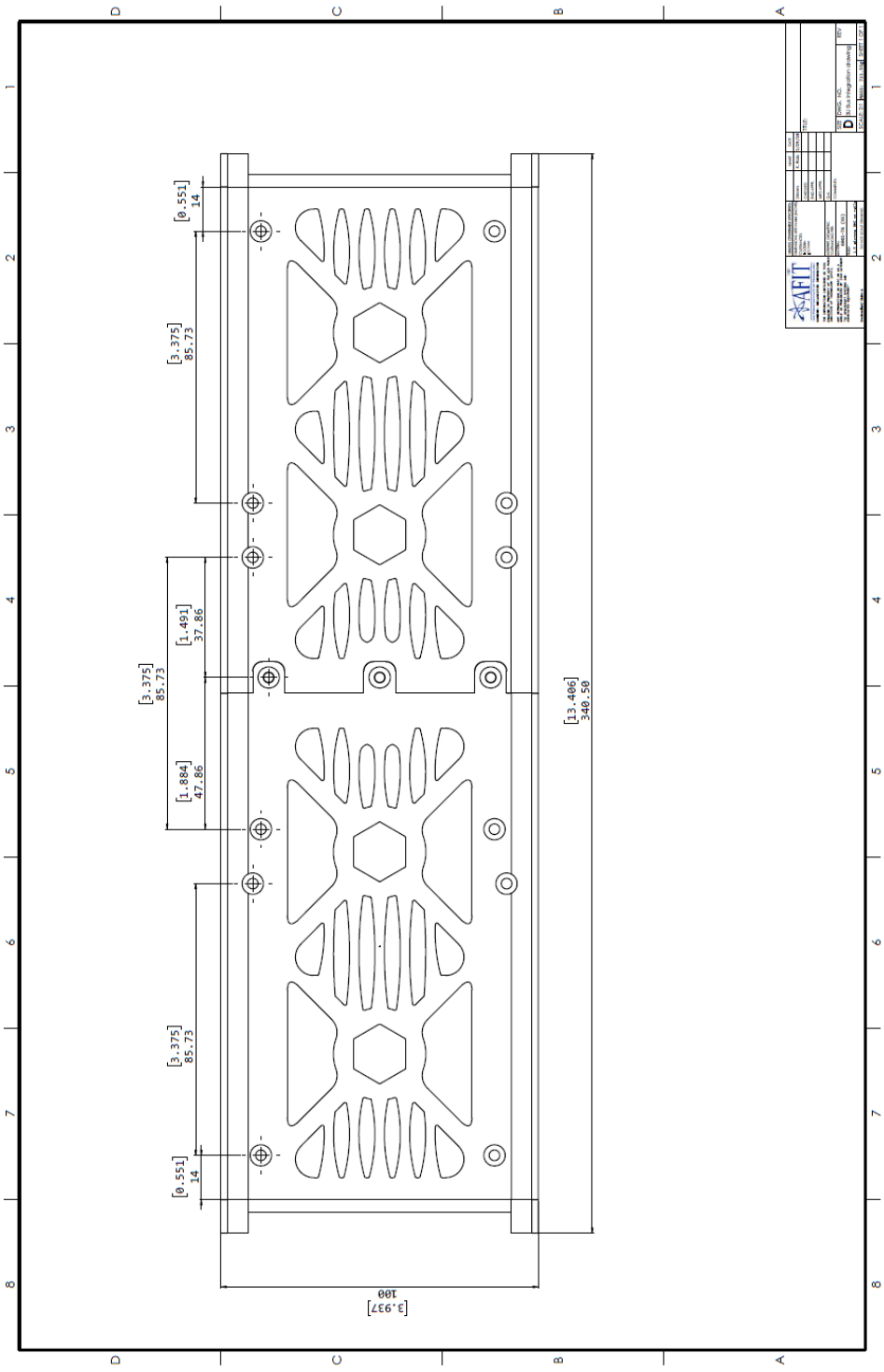

Figure A.1: Male/Female Component Integration

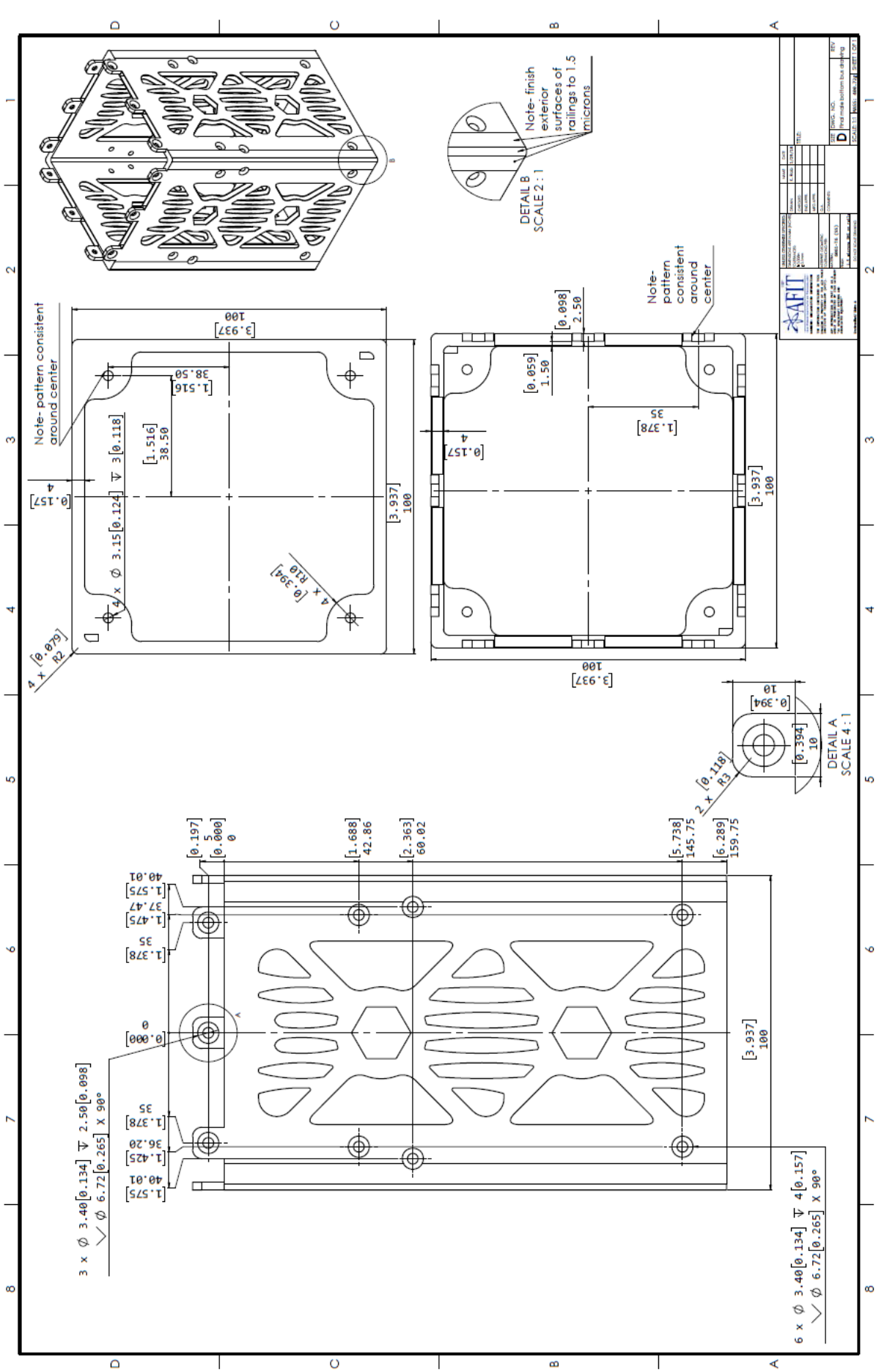

Figure A.2: Male Bus

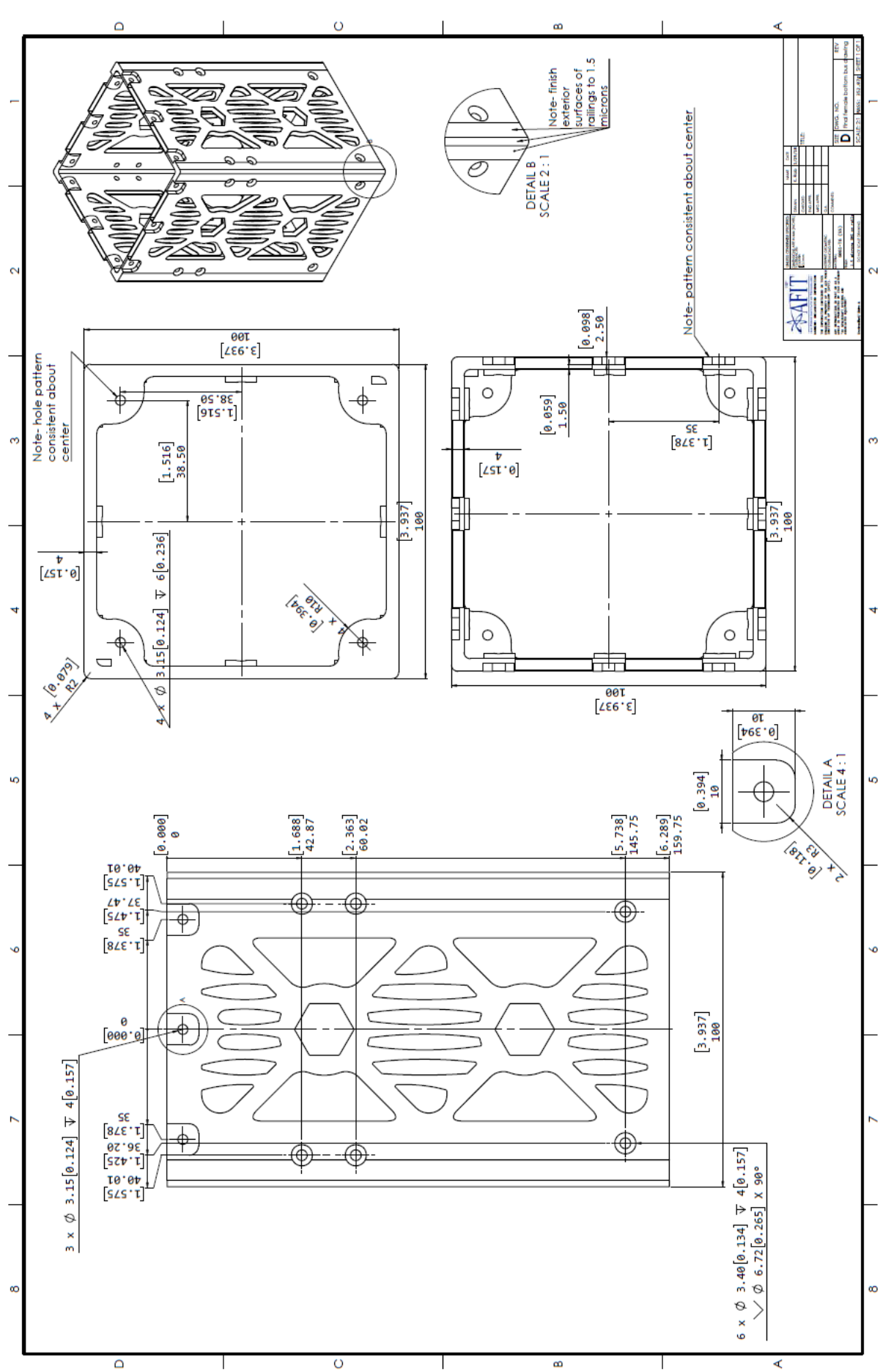

Figure A.3: Female Bus

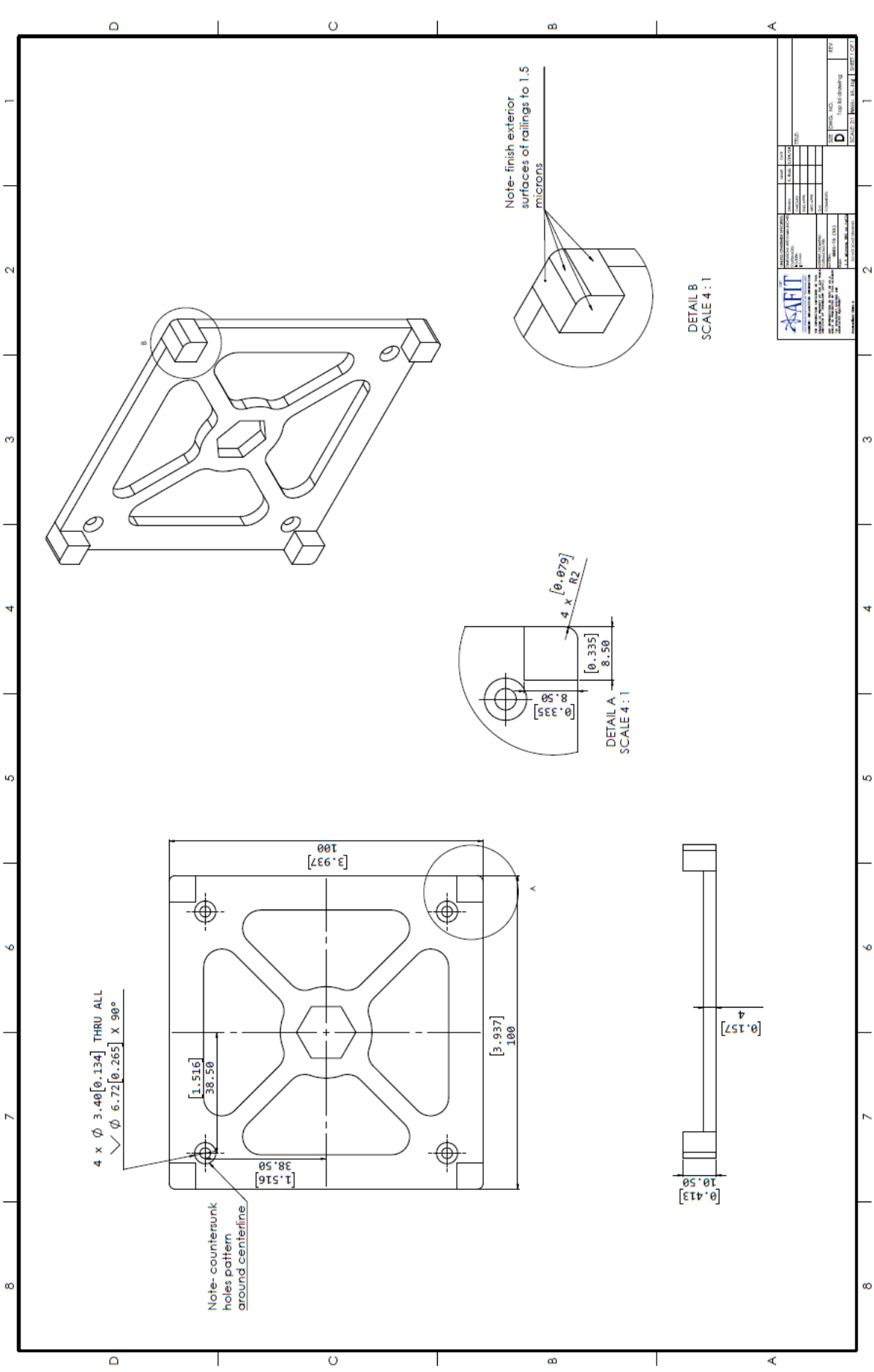

Figure A.4: Exterior Lid

Appendix B. Recommended Fastener Torques

Suggested Torque Values for Metric (300 SST) Heat Treated Screws

Dry Installation (K=0.20)

Syt: 2.07E+08 *(Yield Strength)*
Sps: 1.76E+08 *(Proof Strength)*

	Size	Pitch	Nominal Diameter *D (mm)*	Tensile Stress Area *At (sq mm)*	Category 1 (.78Sps)		Category 2 (.60Sps)		Category 3 (.75Sps)		Category 4 (.90Sps)		Category 5 (Sps)	
					Clamp Load *P (N)*	Torque Value *T*	Clamp Load *P (N)*	Torque Value *T*	Clamp Load *P (N)*	Torque Value *T*	Clamp Load *P (N)*	Torque Value *T*	Clamp Load *P (N)*	Torque Value *T*
cN-m	1.6	0.35	1.6000	1.27003	174	6	134	4	167	5	201	6	223	7
	2	0.40	2.0000	2.07323	284	11	219	9	273	11	328	13	365	15
	2.5	0.45	2.5000	3.39080	464	23	358	18	447	22	537	27	596	30
	3	0.50	3.0000	5.03084	689	41	531	32	663	40	796	48	885	53
	3.5	0.60	3.5000	6.77521	928	65	715	50	893	63	1072	75	1191	83
	4	0.70	4.0000	8.77872	1202	96	926	74	1158	93	1389	111	1543	1.2
N-m	5	0.80	5.0000	14.18255	1942	1.9	1496	1.5	1870	1.9	2244	2.2	2494	2.5
	6	1.00	6.0000	20.12338	2756	3.3	2123	2.5	2654	3.2	3184	3.8	3538	4.2
	8	1.25	8.0000	36.60855	5014	8.0	3862	6.2	4827	7.7	5793	9.3	6436	10.3
	8	1.00	8.0000	39.16711	5364	8.6	4132	6.6	5165	8.3	6198	9.9	6886	11.0
	10	1.5	10.0000	57.98960	7942	15.9	6117	12.2	7647	15.3	9176	18.4	10196	20.4
	10	1.25	10.0000	61.19860	8382	16.8	6456	12.9	8070	16.1	9684	19.4	10760	21.5
	12	1.75	12.0000	84.26655	11541	27.7	8889	21.3	11112	26.7	13334	32.0	14815	35.6
	12	1.25	12.0000	92.07185	12610	30.3	9713	23.3	12141	29.1	14569	35.0	16188	38.9
	14	2.00	14.0000	115.43938	15811	44.3	12178	34.1	15222	42.6	18267	51.1	20296	56.8
	14	1.50	14.0000	124.54556	17058	47.8	13138	36.8	16423	46.0	19707	55.2	21897	61.3
	16	2.00	16.0000	156.66843	21457	68.7	16527	52.9	20659	66.1	24790	79.3	27545	88.1
	16	1.50	16.0000	167.24832	22906	73.3	17643	56.5	22054	70.6	26464	84.7	29405	94.1
	20	2.50	20.0000	244.79442	33527	134.1	25823	103.3	32279	129.1	38735	154.9	43039	172.2
	20	1.50	20.0000	271.50340	37185	148.7	28641	114.6	35801	143.2	42961	171.8	47735	190.9

Figure B.1: Recommended Fastener Torques

Appendix C. 3U CubeSat Acceptance Checklist

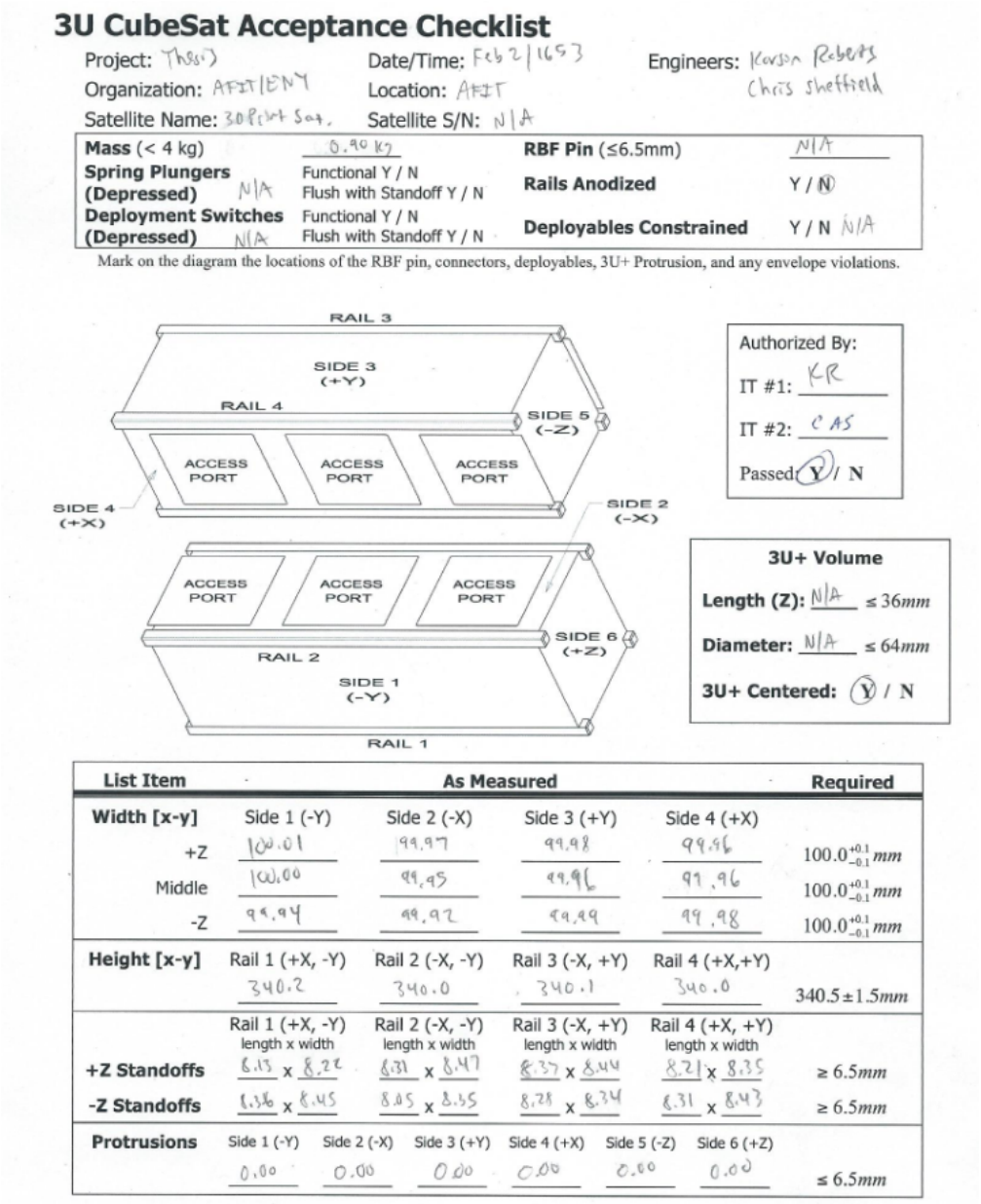

3U CubeSat Acceptance Checklist

Project: Thesis | Date/Time: Feb 2 1653 | Engineers: Kevin Roberts, Chris Sheffield
Organization: AFIT/ENY | Location: AFIT
Satellite Name: 3U Test Sat. | Satellite S/N: N/A

Mass (< 4 kg)	0.90 kg	**RBF Pin** (≤6.5mm)	N/A
Spring Plungers (Depressed) N/A	Functional Y / N Flush with Standoff Y / N	**Rails Anodized**	Y / (N)
Deployment Switches (Depressed) N/A	Functional Y / N Flush with Standoff Y / N	**Deployables Constrained**	Y / N N/A

Mark on the diagram the locations of the RBF pin, connectors, deployables, 3U+ Protrusion, and any envelope violations.

Authorized By:
IT #1: KR
IT #2: CAS
Passed (Y) / N

3U+ Volume
Length (Z): N/A ≤ 36mm
Diameter: N/A ≤ 64mm
3U+ Centered: (Y) / N

List Item	As Measured				Required
Width [x-y]	Side 1 (-Y)	Side 2 (-X)	Side 3 (+Y)	Side 4 (+X)	
+Z	100.01	99.97	99.98	99.96	$100.0^{+0.1}_{-0.1}$ mm
Middle	100.00	99.95	99.96	99.96	$100.0^{+0.1}_{-0.1}$ mm
-Z	99.94	99.92	99.99	99.98	$100.0^{+0.1}_{-0.1}$ mm
Height [x-y]	Rail 1 (+X, -Y)	Rail 2 (-X, -Y)	Rail 3 (-X, +Y)	Rail 4 (+X,+Y)	
	340.2	340.0	340.1	340.0	340.5±1.5mm
	Rail 1 (+X, -Y) length x width	Rail 2 (-X, -Y) length x width	Rail 3 (-X, +Y) length x width	Rail 4 (+X, +Y) length x width	
+Z Standoffs	8.13 x 8.22	8.31 x 8.47	8.37 x 8.44	8.21 x 8.35	≥ 6.5mm
-Z Standoffs	8.36 x 8.45	8.05 x 8.35	8.28 x 8.34	8.31 x 8.43	≥ 6.5mm
Protrusions	Side 1 (-Y)	Side 2 (-X)	Side 3 (+Y)	Side 4 (+X)	Side 5 (-Z)	Side 6 (+Z)	
	0.00	0.00	0.00	0.00	0.00	0.00	≤ 6.5mm

Figure C.1: Completed CubeSat Acceptance Checklist

Appendix D. Vibration Testing Results

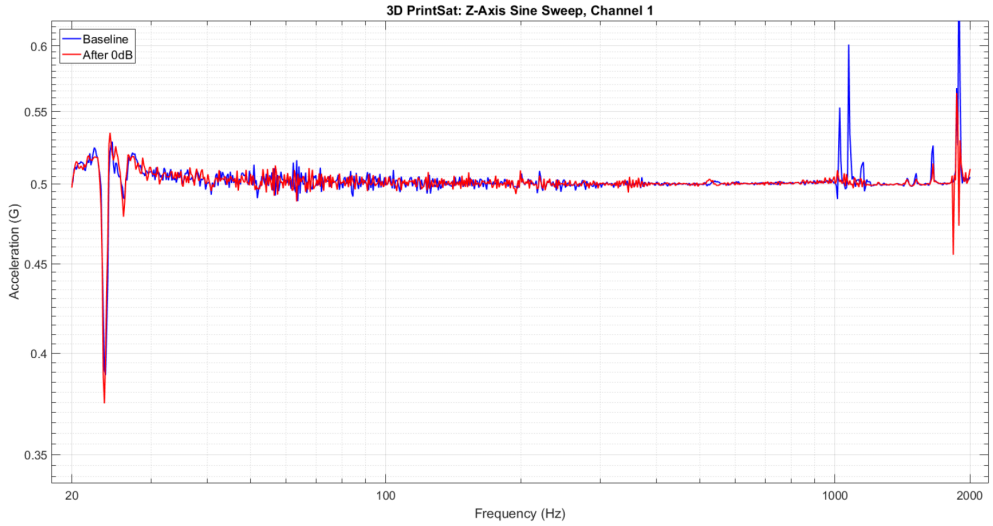

Figure D.1: Z Axis Run 1 Control Accelerometer Response

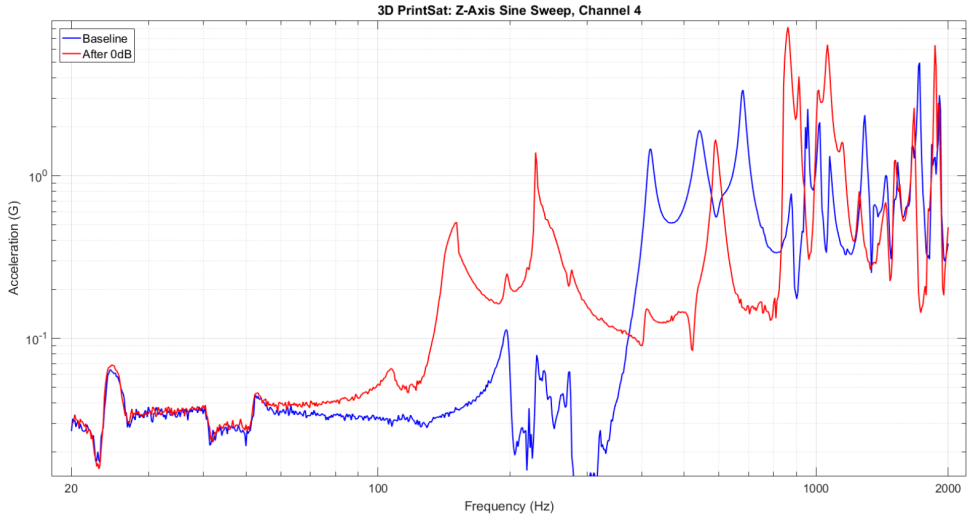

Figure D.2: Z Axis Run 1 Accelerometer 3 Response

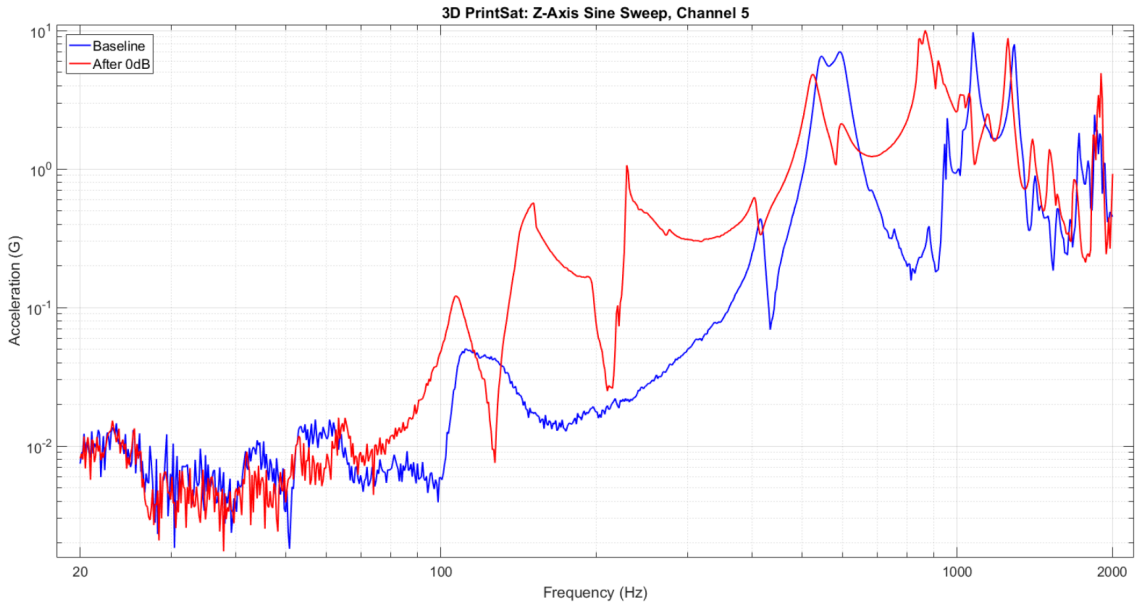

Figure D.3: Z Axis Run 1 Accelerometer 4 Response

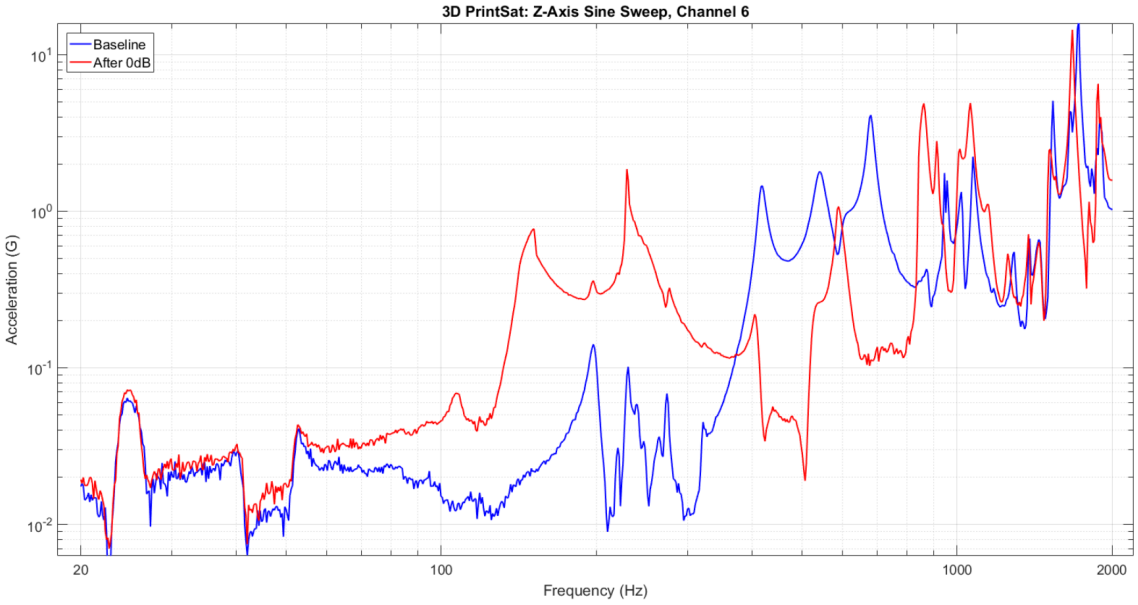

Figure D.4: Z Axis Run 1 Accelerometer 5 Response

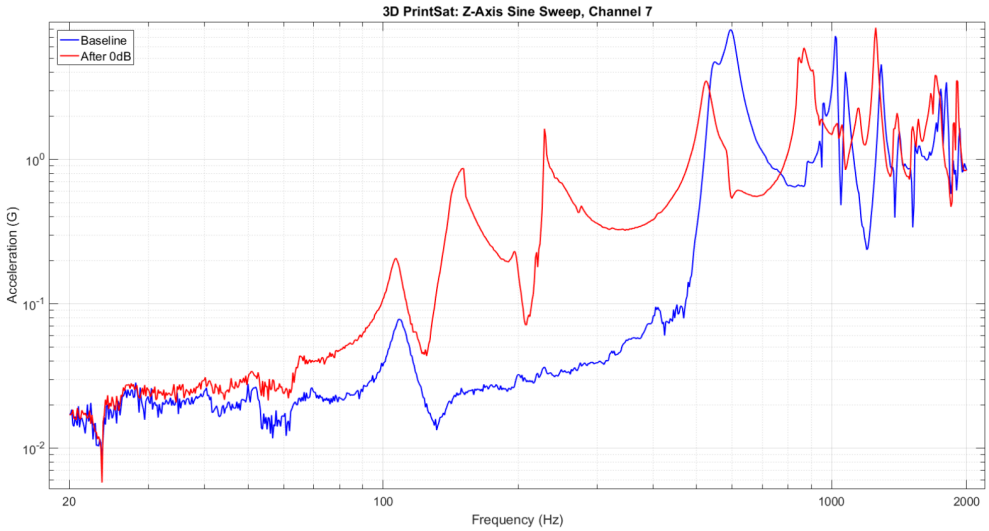

Figure D.5: Z Axis Run 1 Accelerometer 6 Response

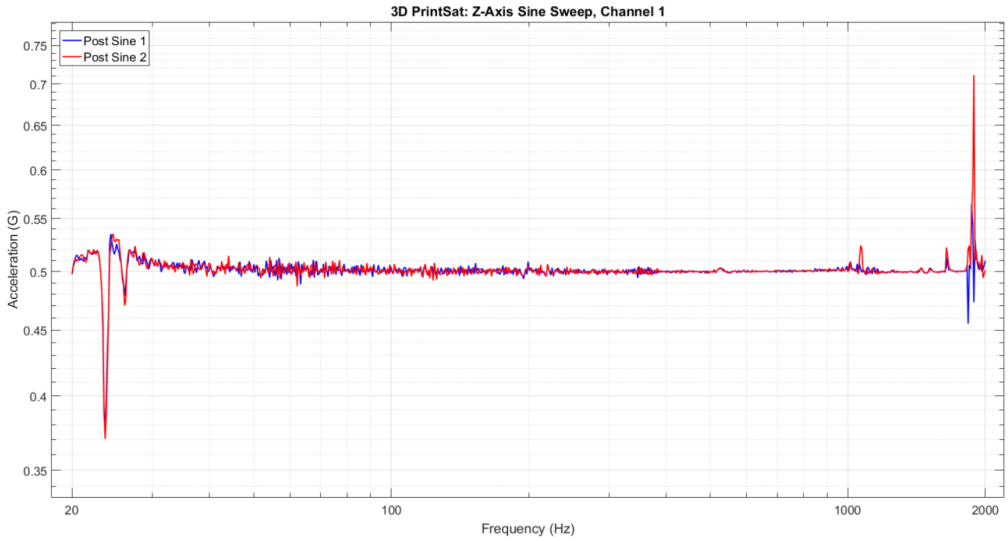

Figure D.6: Z Axis Run 2 Control Accelerometer Response

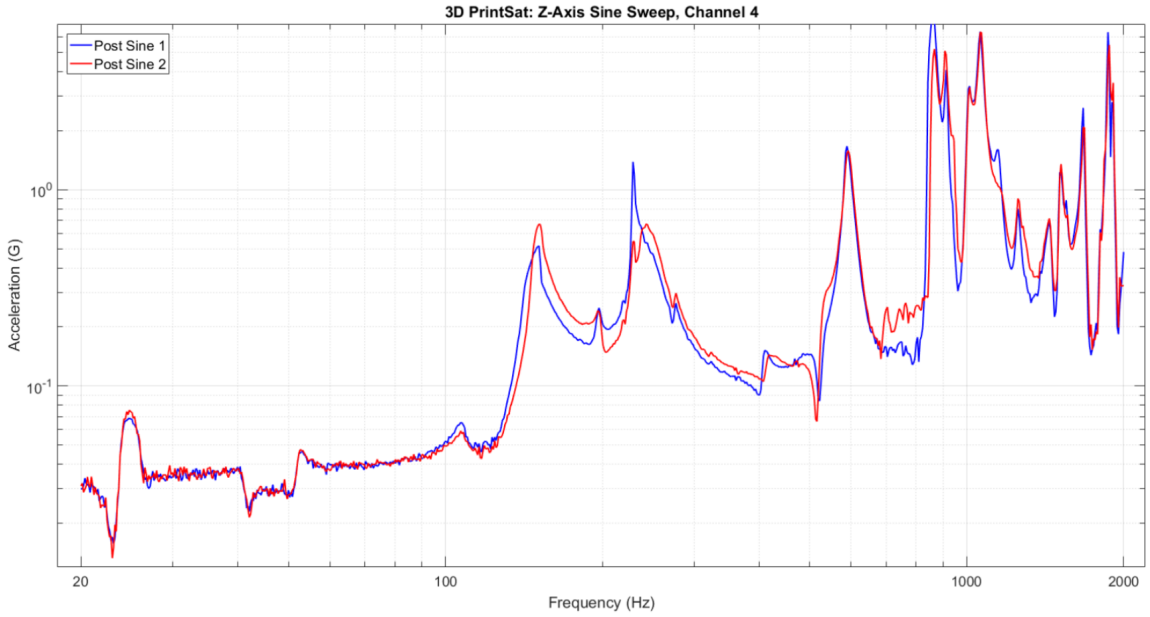

Figure D.7: Z Axis Run 2 Accelerometer 3 Response

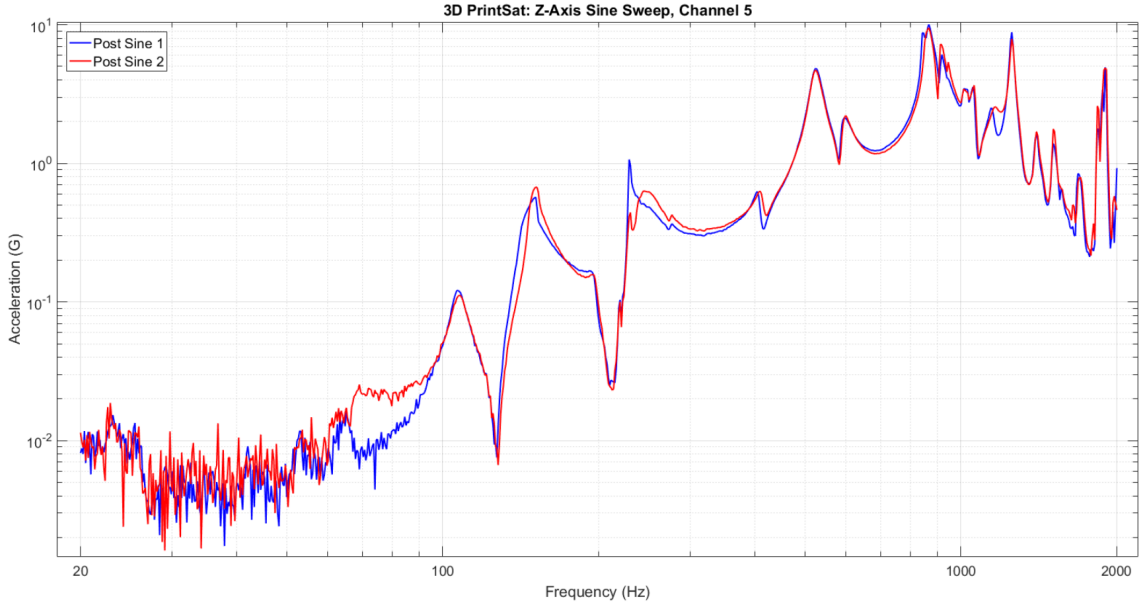

Figure D.8: Z Axis Run 2 Accelerometer 4 Response

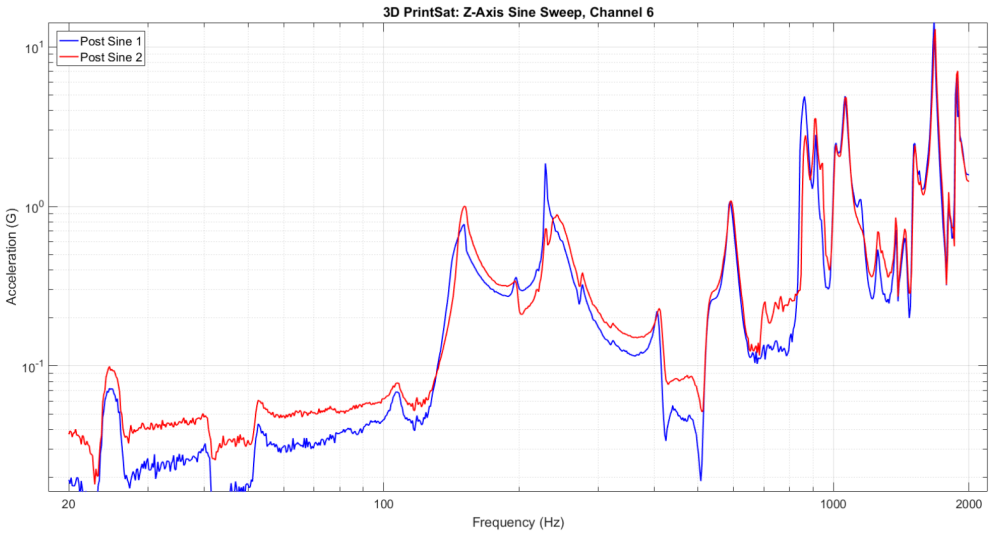

Figure D.9: Z Axis Run 2 Accelerometer 5 Response

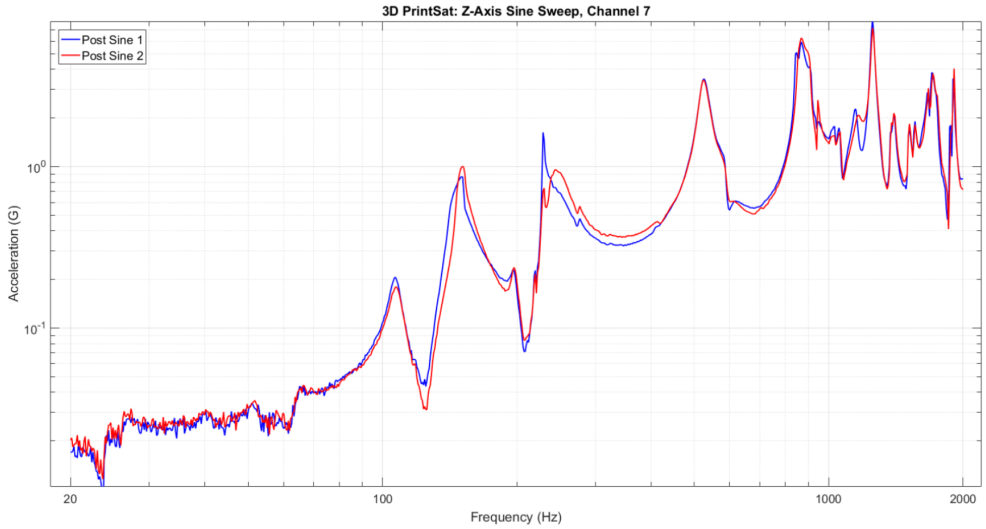

Figure D.10: Z Axis Run 2 Accelerometer 6 Response

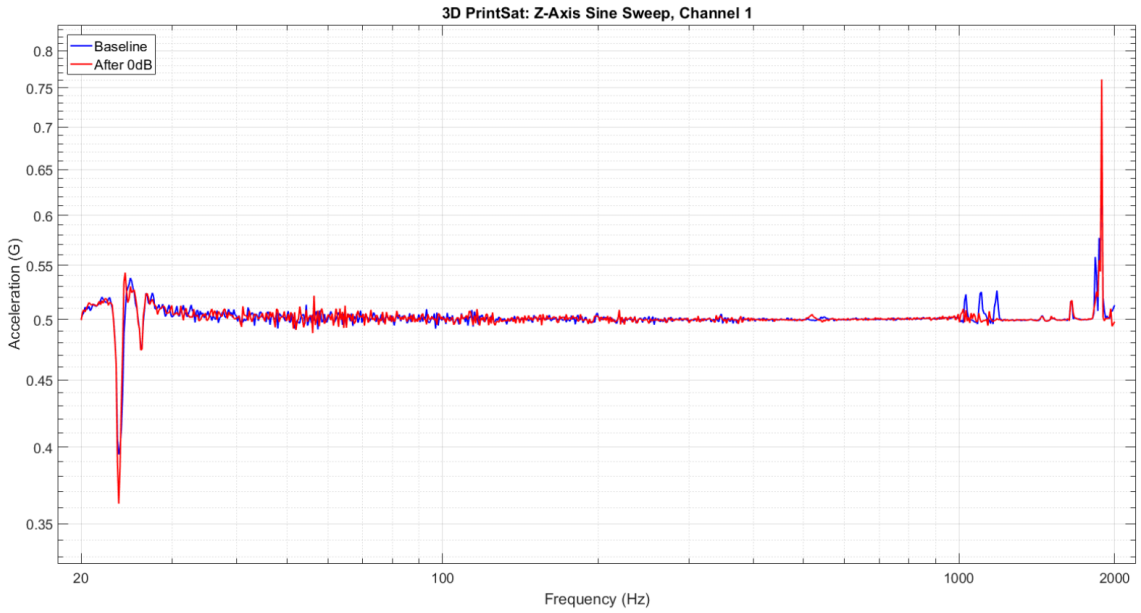

Figure D.11: Z Axis Run 3 Control Accelerometer Response

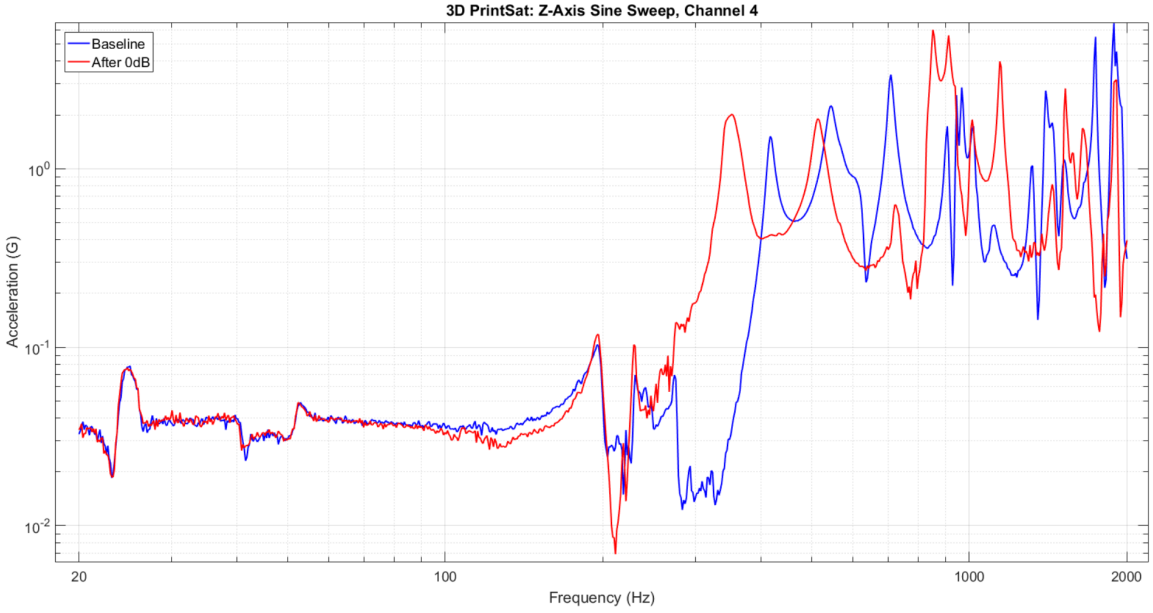

Figure D.12: Z Axis Run 3 Accelerometer 3 Response

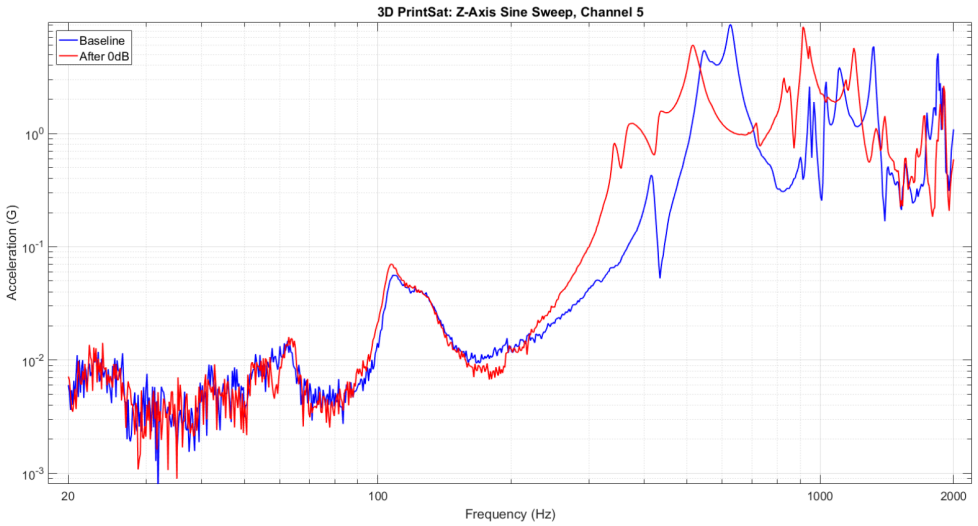

Figure D.13: Z Axis Run 3 Accelerometer 4 Response

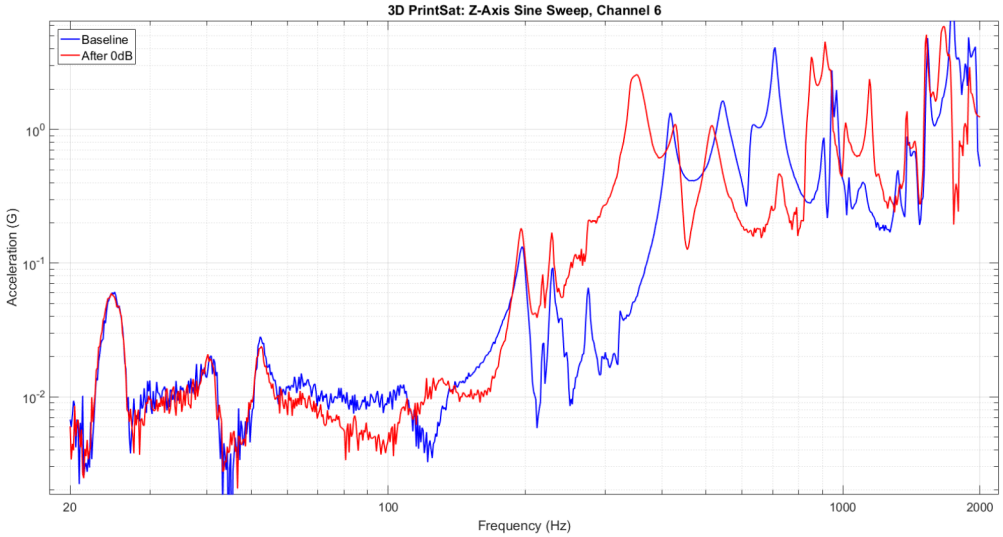

Figure D.14: Z Axis Run 3 Accelerometer 5 Response

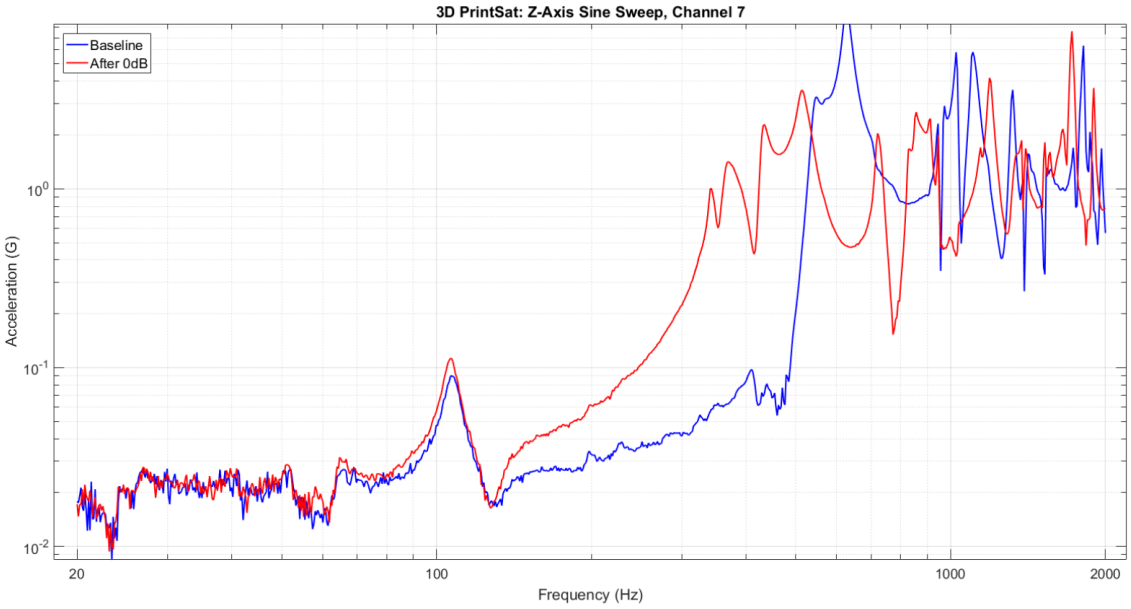

Figure D.15: Z Axis Run 3 Accelerometer 6 Response

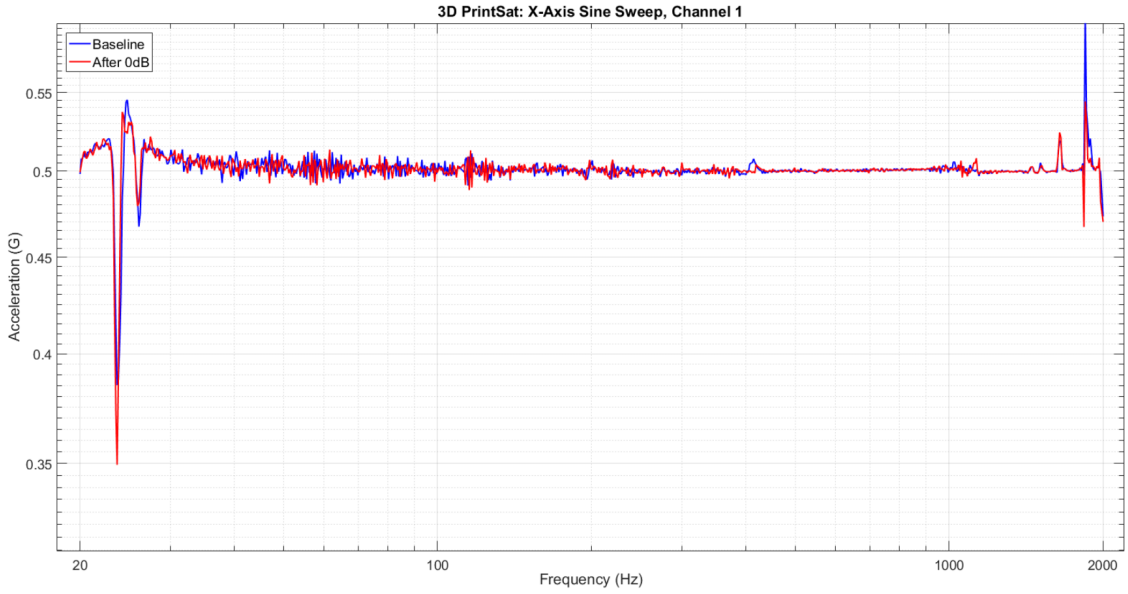

Figure D.16: X Axis Run 1 Control Accelerometer Response

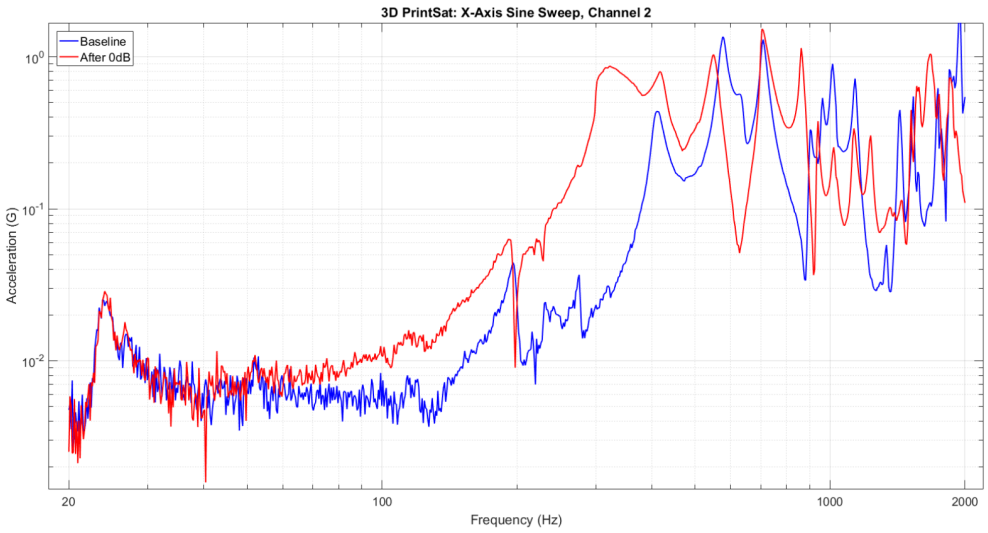

Figure D.17: X Axis Run 1 Accelerometer 1 Response

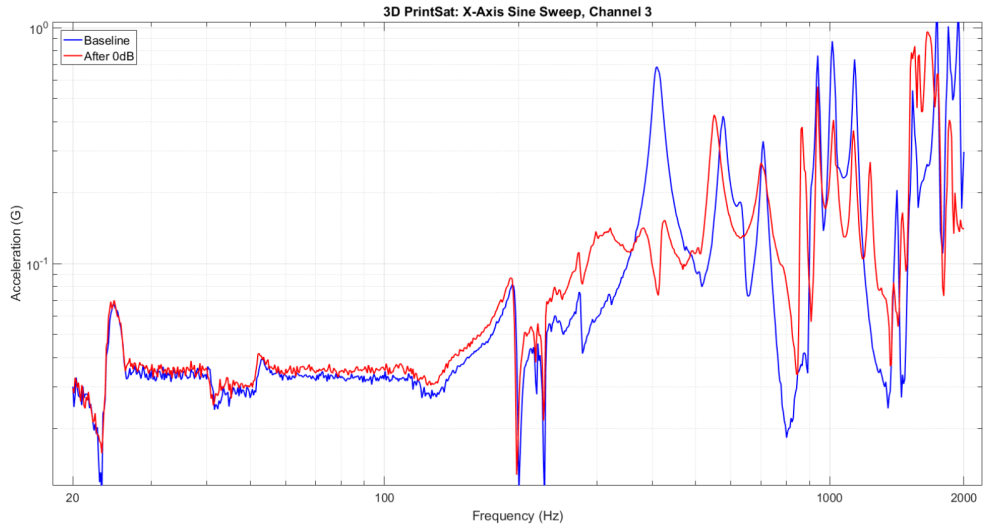

Figure D.18: X Axis Run 1 Accelerometer 2 Response

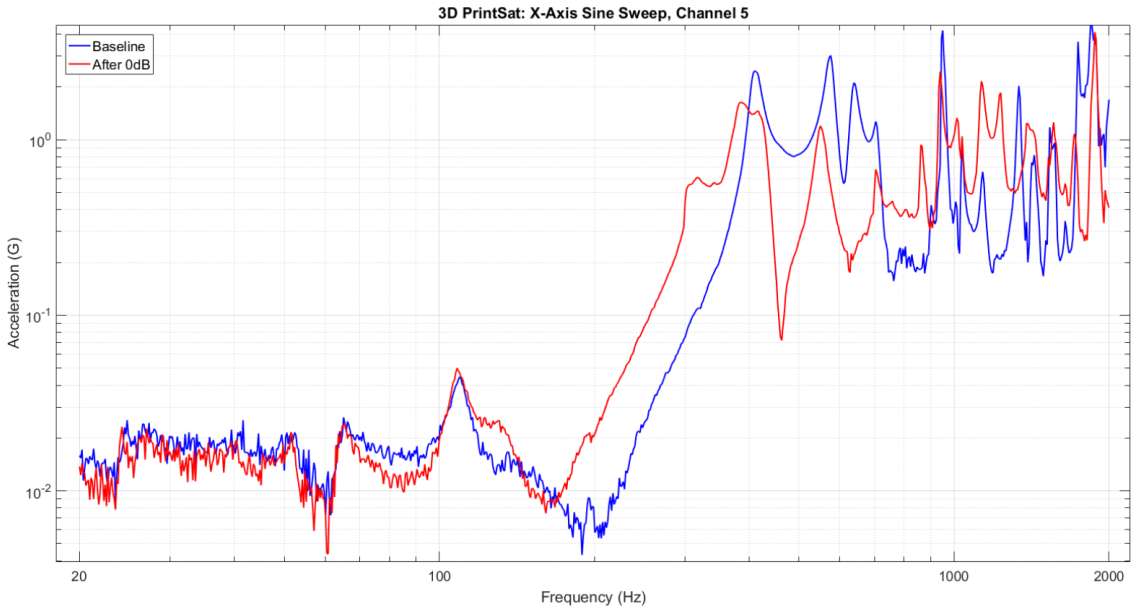

Figure D.19: X Axis Run 1 Accelerometer 4 Response

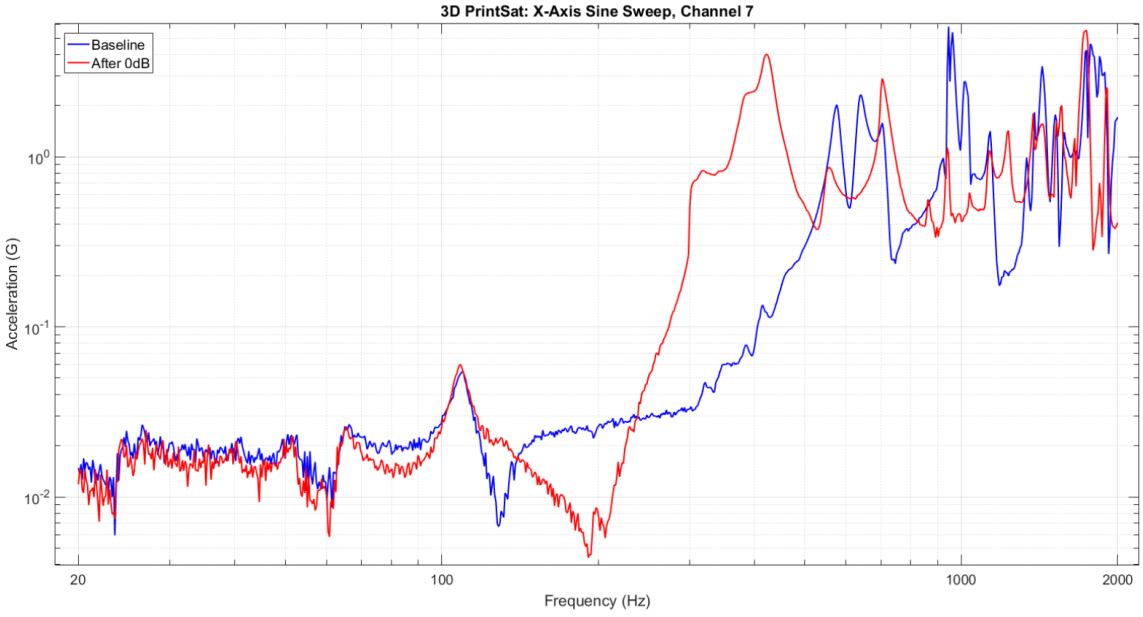

Figure D.20: X Axis Run 1 Accelerometer 6 Response

Bibliography

[1] C. Belle, "Mass Challenge for CubeSats," 2015.

[2] CalPoly, "Cubesat design specification (CDS)," Tech. Rep., 2014.

[3] PC/104 Embedded-PC Modules, *PC / 104 Specification*, 2008.

[4] Planetary Systems Corporation, "Canisterized Satellite Dispensor (CSD) Data Sheet," Planetary Systems Corporation, Tech. Rep., 2015.

[5] V. Bashbush, "Characterization of the Internal and External Requirements of the CubeSat P-POD and Test Pod," Ph.D. dissertation, California Polytechnic State University, 2004.

[6] I3DMFG, "Manufacturing Best Practices," p. 225, 2010.

[7] G. Konecny, "Small Satellites-A Tool For Earth Observation?" Institute of Photogrammetry and GeoInformation, University of Hannover, Tech. Rep.

[8] J. Wertz *et al.*, *Space Mission Engineering: The New SMAD*. Hawthorne, CA: Microcosm Press, 2015.

[9] W. Gao *et al.*, "The status, challenges, and future of additive manufacturing in engineering," *Computer-Aided Design*, vol. 69, pp. 65–89, 2015.

[10] Ultimaker, *Technical data sheet PLA*, 2016.

[11] MatWeb, *Special Metals INCONEL ® Alloy 718*, 2017.

[12] EOS GmbH - Electro Optical Systems, "Material Data Sheet: EOS Aluminium AlSi10Mg," Tech. Rep., 2014.

[13] ASM, "ASM Material Data Sheet Subcategory : 6000 Series Aluminum Alloy," Tech. Rep., 2012.

[14] NRO, "National Reconnaissance Office 2013 Innovation Campaign: The CubeSat Program," 2013.

[15] J. D. Fielding *et al.*, "Department of Defense Additive Manufacturing Roadmap," Tech. Rep. November, 2016.

[16] National Aeronautics and Space Administration, "REQUIREMENTS FOR THREADED FASTENING SYSTEMS IN SPACEFLIGHT HARDWARE," Washington, D.C., Tech. Rep. NASA-STD-5020, 2012.

[17] ——, "General Environmental Verification Standard (GEVS) For GSFC Flight Programs and Projects," NASA Goddard Space Flight Center, Greenbelt, Maryland, Tech. Rep. GSFC-STD-7000A, 2013.

[18] Planetary Systems Corporation, "Payload Specification for 3U, 6U, 12U, and 27U," Planetary Systems Corporation, Tech. Rep., 2016.

[19] M. Swartwout, "The first one hundred CubeSats : A statistical look," *Journal of Small Satellites*, vol. 2, no. 2, pp. 213–233, 2013.

[20] D. Selva and D. Krejci, "A survey and assessment of the capabilities of Cubesats for Earth observation," *Acta Astronautica*, vol. 74, pp. 50–68, 2012.

[21] R. E. Sharples, "Evaluation of the Impact of an Additive Manufacturing Enhanced CubeSat Architecture on the CubeSat Development Process," Master's thesis, Air Force Institute of Technology, 2016.

[22] I. Planet Labs, "Meet The Dove," 2017.

[23] C. O. Asma *et al.*, "Orbital Dynamics Characteristics of a QB50 CubeSat Performing Atmospheric Re-Entry," *AIAA Atmospheric Flight Mechanics Conference*, no. August, pp. AIAA2010–7812, 2010.

[24] F. L. Markley and J. L. Crassidis, *Fundamentals of Spacecraft Attitude Determination and Control*. New York: Springer Science & Business Media, 2014.

[25] M. Swartwout, "Cheaper by the dozen: The avalanche of rideshares in the 21st century," in *IEEE Aerospace Conference Proceedings*, 2013, pp. 1–12.

[26] A. Chin *et al.*, "CubeSat: The Pico-Satellite Standard for Research and Education," *AIAA SPACE 2008 Conference & Exposition*, no. September, pp. 1–11, 2008.

[27] W. Lan, "Poly Picosatellite Orbital Deployer Mk III ICD," Tech. Rep., 2007.

[28] NanoRacks LLC, "NanoRacks Completes Largest ISS CubeSat Deployment Cycle To Date," 2017.

[29] ——, "NV NanoRacks CubeSat Deployer (NRCSD) Interface Control Document," Tech. Rep. NR-SRD-029, 2013.

[30] C. Rich, "Spacecraft Systems Engineering: Manufacture and Test," 2017.

[31] National Aeronautics and Space Administration, "Payload Test Requirements," Tech. Rep., 2004.

[32] ——, "Standard Materials and Processes Requirements for Spacecraft," Tech. Rep. SP-645, 2016.

[33] A. Calvi, "Spacecraft Loads Analysis," ESA/ESTEC, Noordwijk, The Netherlands, Tech. Rep., 2011.

[34] Polytec, "PSV-400 Scanning Vibrometer."

[35] S. Fernando, "Mechanisms and Prevention of Vibration Loosening in Bolted Joints," Tech. Rep., 2005.

[36] R. C. Latta III, "Structural Analysis of a 6U CubeSat Chassis," Master's thesis, AFIT, 2014.

[37] C. Inventor, "All About Screws," 2008.

[38] Loughborough University, "The 7 Categories of Additive Manufacturing," 2017.

[39] W. E. King *et al.*, "Laser powder bed fusion additive manufacturing of metals; physics, computational, and materials challenges," *Applied Physics Reviews*, vol. 2, no. 4, p. 041304, 2015.

[40] Box, Christopher A., "Analysis of Additively Manufactured Lattice Structures by Finite Element Methods," Master's thesis, Air Force Institute of Technology, 2011.

[41] I3DMFG, "DMLS Thrusters."

[42] Space Exploration Technologies, Inc., "Space X Launches 3D-Printed Part to Space, Creates Printed Engine Chamber," 2014.

[43] D. Espalin *et al.*, "3D Printing multifunctionality: Structures with electronics," *International Journal of Advanced Manufacturing Technology*, vol. 72, no. 5-8, pp. 963–978, 2014.

[44] Utah State University, "Torque Limits for Threaded Fasteners," Utah State University Research Foundation, North Logan, Utah, Tech. Rep., 2010.

REPORT DOCUMENTATION PAGE

Form Approved
OMB No. 0704–0188

1. REPORT DATE *(DD–MM–YYYY)*	2. REPORT TYPE	3. DATES COVERED *(From — To)*
22 March 2018	Master's Thesis	October 2016 — 22 March 2018

4. TITLE AND SUBTITLE

DESIGN AND TESTING OF AN ADDITIVELY MANUFACTURED CUBESAT STRUCTURAL BUS

5a. CONTRACT NUMBER

5b. GRANT NUMBER

5c. PROGRAM ELEMENT NUMBER

6. AUTHOR(S)

Roberts, Karson, A. , 2nd Lieutenant

5d. PROJECT NUMBER

5e. TASK NUMBER

5f. WORK UNIT NUMBER

7. PERFORMING ORGANIZATION NAME(S) AND ADDRESS(ES)

Air Force Institute of Technology
Graduate School of Engineering and Management (AFIT/EN)
2950 Hobson Way
WPAFB OH 45433-7765

8. PERFORMING ORGANIZATION REPORT NUMBER

AFIT-ENY-MS-18-M-289

9. SPONSORING / MONITORING AGENCY NAME(S) AND ADDRESS(ES)

10. SPONSOR/MONITOR'S ACRONYM(S)

11. SPONSOR/MONITOR'S REPORT NUMBER(S)

12. DISTRIBUTION / AVAILABILITY STATEMENT

DISTRIBUTION STATEMENT A:
APPROVED FOR PUBLIC RELEASE; DISTRIBUTION UNLIMITED.

13. SUPPLEMENTARY NOTES

14. ABSTRACT

Recent innovations in additive manufacturing and design capabilities have opened the door for more opportunities to integrate multiple functions into a structural design. Specifically, 3D printing through advanced laser powder bed fusion of metal powder allows for the development and integration of advanced structures that were previously unachievable. The demonstration of these techniques on a small satellite results in a structural bus consisting of various external and internal features, increasing its functionality and capabilities beyond simply providing structural support. 3D printing a multi-functional CubeSat bus with these integrated features such as internal lattices and wiring tabs demonstrates a new way of thinking going forward: modularizing the structural design and incorporating various capabilities that can meet a unique or generic satellite mission. This research addresses the design and testing of an additively manufactured CubeSat structural bus. 3D printing capabilities were harnessed to incorporate lattices into the walls of the structure, increasing its natural frequency and decreasing mass. The 3D printed unloaded CubeSat structure was vibration tested to NASA GEVS qualification levels, and showed no damage and proved survivability under these loading conditions.

15. SUBJECT TERMS

Additive Manufacturing, CubeSat

16. SECURITY CLASSIFICATION OF:			17. LIMITATION OF ABSTRACT	18. NUMBER OF PAGES	19a. NAME OF RESPONSIBLE PERSON
a. REPORT	b. ABSTRACT	c. THIS PAGE			Major Ryan O'Hara, AFIT/ENY
U	U	U	UU	112	19b. TELEPHONE NUMBER *(include area code)* (937) 785-3636, x4542; Ryan.OHara@afit.edu